

AD\_\_\_\_\_

Award Number: W81XWH-12-2-0114

TITLE: Cyanide Antidotes for Mass Casualties: Comparison of Intramuscular Injector by Autoinjector, Intraosseous Injection, and Inhalational Delivery

PRINCIPAL INVESTIGATOR: Gerry R. Boss

CONTRACTING ORGANIZATION: University of California, San Diego

REPORT DATE: December 2015

TYPE OF REPORT: Final

PREPARED FOR: U.S. Army Medical Research and Materiel Command  
Fort Detrick, Maryland 21702-5012

DISTRIBUTION STATEMENT: Approved for Public Release;  
Distribution Unlimited

The views, opinions and/or findings contained in this report are those of the author(s) and should not be construed as an official Department of the Army position, policy or decision unless so designated by other documentation.

<b>REPORT DOCUMENTATION PAGE</b>				<i>Form Approved</i> <i>OMB No. 0704-0188</i>	
Public reporting burden for this collection of information is estimated to average 1 hour per response, including the time for reviewing instructions, searching existing data sources, gathering and maintaining the data needed, and completing and reviewing this collection of information. Send comments regarding this burden estimate or any other aspect of this collection of information, including suggestions for reducing this burden to Department of Defense, Washington Headquarters Services, Directorate for Information Operations and Reports (0704-0188), 1215 Jefferson Davis Highway, Suite 1204, Arlington, VA 22202-4302. Respondents should be aware that notwithstanding any other provision of law, no person shall be subject to any penalty for failing to comply with a collection of information if it does not display a currently valid OMB control number. <b>PLEASE DO NOT RETURN YOUR FORM TO THE ABOVE ADDRESS.</b>					
<b>1. REPORT DATE</b> December 2015		<b>2. REPORT TYPE</b> Final		<b>3. DATES COVERED</b> 26 Sep 2012 - 25 Sep 2015	
<b>4. TITLE AND SUBTITLE</b> Cyanide Antidotes for Mass Casualties: Comparison of Intramuscular Injector by Autoinjector, Intraosseous Injection, and Inhalational Delivery				<b>5a. CONTRACT NUMBER</b>	
				<b>5b. GRANT NUMBER</b> W81XWH-12-2-0114	
				<b>5c. PROGRAM ELEMENT NUMBER</b>	
<b>6. AUTHOR(S)</b> Gerry R. Boss  E-Mail: gboss@ucsd.edu				<b>5d. PROJECT NUMBER</b>	
				<b>5e. TASK NUMBER</b>	
				<b>5f. WORK UNIT NUMBER</b>	
<b>7. PERFORMING ORGANIZATION NAME(S) AND ADDRESS(ES)</b>  University of California, San Diego 9500 Gilman Drive La Jolla, CA 92093				<b>8. PERFORMING ORGANIZATION REPORT NUMBER</b>	
<b>9. SPONSORING / MONITORING AGENCY NAME(S) AND ADDRESS(ES)</b> U.S. Army Medical Research and Materiel Command Fort Detrick, Maryland 21702-5012				<b>10. SPONSOR/MONITOR'S ACRONYM(S)</b>	
				<b>11. SPONSOR/MONITOR'S REPORT NUMBER(S)</b>	
<b>12. DISTRIBUTION / AVAILABILITY STATEMENT</b> Approved for Public Release; Distribution Unlimited					
<b>13. SUPPLEMENTARY NOTES</b>					
<b>14. ABSTRACT</b> Current antidotes for cyanide poisoning must be administered by intravenous injection, which would not be practical for treating mass casualties as could occur in a major industrial accident or a terrorist attack. Thus, a need exists for alternative modes of administering cyanide antidotes, and we compared three different administration modes: intramuscular injection, intraosseous injection, and inhalational delivery. We found that all three modes can rescue animals from exposure to lethal cyanide doses. As part of these studies, we tested three new cyanide antidotes that are under development: cobinamide, dimethyltrisulfide, and sulfanegen.					
<b>15. SUBJECT TERMS</b> Cyanide Poisoning; Intramuscular Injection; Intraosseous Injection; Inhalational Delivery					
<b>16. SECURITY CLASSIFICATION OF:</b>			<b>17. LIMITATION OF ABSTRACT</b>	<b>18. NUMBER OF PAGES</b>	<b>19a. NAME OF RESPONSIBLE PERSON</b>
<b>a. REPORT</b> U	<b>b. ABSTRACT</b> U	<b>c. THIS PAGE</b> U			USAMRMC
			UU	10	<b>19b. TELEPHONE NUMBER</b> (include area code)

## Table of Contents

	<u>Page</u>
Cover Page .....	1
Report Documentation Page .....	2
Table of Contents .....	3
Introduction.....	4
Keywords .....	4
Accomplishments.....	4-7
Impact.....	7-8
Changes/Problems.....	8
Products.....	8
Participants and Other Collaborating Institutions.....	8-9
Special Reporting Requirements.....	9
Appendices.....	9

## **INTRODUCTION**

Cyanide is a rapidly acting poison, and, thus, antidotes must be administered quickly; clearly, the fastest way to deliver a drug to the systemic circulation is via intravenous injection. However, even under the best of circumstances, starting an intravenous line takes several minutes, and even more time will likely be required in cyanide-poisoned victims, since they may be hypotensive with collapsed peripheral veins. Thus, intravenous antidote administration would not be practical in the setting of mass casualties from cyanide exposure. Of other possible routes of drug administration, three stand out as potentially very useful to treat a large number of cyanide-poisoned people: intramuscular injection, intraosseous injection, and inhalational delivery. We sought to compare each of these three drug delivery modes to intravenous injection in three different species—mice, rabbits, and pigs. Each delivery mode has advantages and disadvantages. Intramuscular injection, particularly using an autoinjector is very quick, can be performed through clothing, can be done via self-administration, and has well developed technology. However, a limited volume can be injected, and muscle blood flow is relatively low under resting conditions and can be severely compromised during hypotension as occurs in cyanide poisoning. Intraosseous injection provides access to the systemic circulation as rapidly as intravenous injection, does not require finding a vein, and can be accomplished in a clothed hypotensive person. Disadvantages of intraosseous injection are that it is technically more difficult and time-consuming than intramuscular injection, cannot be conducted in a self-administration mode, and absorption can be potentially reduced by peripheral vasoconstriction. Inhalational delivery has advantages of self-administration, and very rapid absorption not compromised by peripheral vasoconstriction. Disadvantages of inhalational delivery are that the subject needs to be breathing, significant amounts of drug can be lost in the upper airways, and current inhalers deliver only small quantities of drug.

## **KEYWORDS**

Cyanide poisoning; intramuscular injection; intraosseous injection; inhalational drug delivery; cyanide antidotes.

## **ACCOMPLISHMENTS**

### **Major Goals of Project**

The major goals of this project were to develop a cyanide antidote that could be administered in the field quickly and easily. Three modes of antidote administration were tested: intramuscular injection, intraosseous injection, and inhalational delivery.

### **Major Accomplishments**

The major accomplishments are provided for each of the three modes of antidote delivery.

#### **Intramuscular Injection**

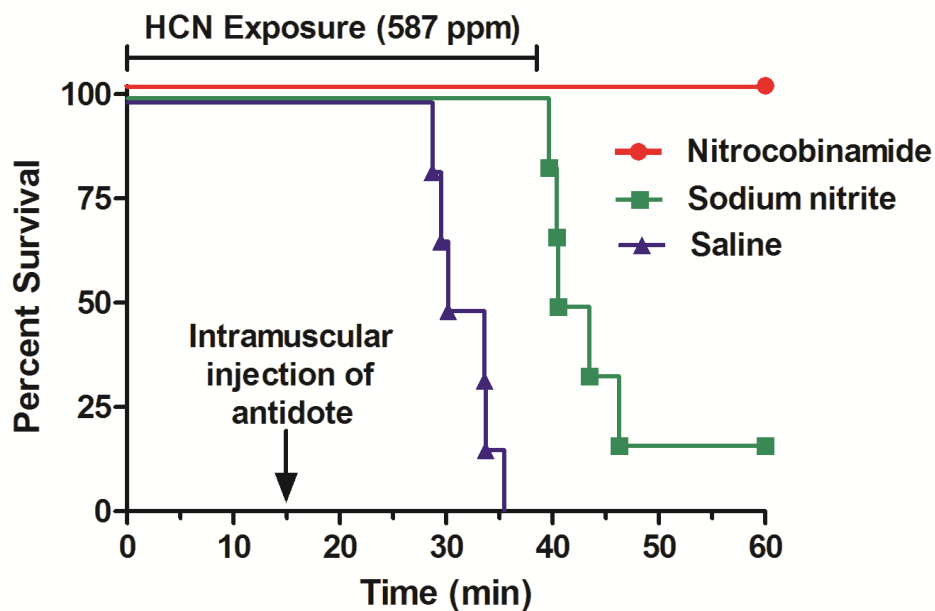
We tested cobinamide, dimethyltrisulfide, and sulfanegen administered by intramuscular injection in lethal mouse, rabbit, and pig models of cyanide poisoning. We found that all three drugs rescue the animals—even when the animals have been apneic for one minute—when the drugs are administered by intramuscular injection. Each drug requires a specific formulation for effective absorption after intramuscular injection. In Figure 1 (next page), we show the results for cobinamide (formulated with four moles of sodium nitrite) in an inhalational mouse model. As can be seen, nitrocobinamide fully rescued animals from a lethal exposure of cyanide gas. Sodium nitrite, at a dose corresponding to the amount of nitrite in the nitrocobinamide, had minimal effect.

Ideally, it would be best to use an autoinjector for intramuscular injection of the three cyanide antidotes, since it would be quicker and easier than using a conventional syringe and needle. We had entered into negotiations with Meridian Medical Technologies (MMT), a major provider of autoinjectors. However, MMT developed technical problems with one of its products, and has devoted all its efforts to resolving those problems. Hence, MMT is no longer a viable source of autoinjectors. We recently learned that Scandinavian Health Limited (SHL) Group markets several autoinjectors that would be appropriate for injecting a cyanide antidote. We are now discussing with them the possibility of using one of their autoinjectors in our drug development projects.



**Figure. 1. Intramuscular Injection of Nitrocobinamide in Mice.**

C57/Bl mice (6 animals/condition) were exposed to 587 ppm of cyanide gas for a total of 40 min in a sealed Plexiglas chamber. After 15 min of exposure, they were removed from the chamber, and injected intramuscularly with either 1.5  $\mu$ mol nitrocobinamide (red circles), 6.0  $\mu$ mol sodium nitrite (green squares), or saline (purple triangles). They were then placed back in the chamber for 25 min. The 6  $\mu$ mol of sodium nitrite corresponds to the amount of nitrite in the 1.5  $\mu$ mol of nitrocobinamide.



**Intraosseous Injection**

We have administered cobinamide via intraosseous injection to both rabbits (Drs. Brenner and Mahon) and pigs (Dr. Vikhyat Bebartha at University of Texas, San Antonio). We found that this administration mode rescued animals from lethal cyanide doses as effectively as when the antidote was given by intravenous injection. Results in pigs are shown in Figure 2 (next page). As part of these experiments, we compared cobinamide to hydroxocobalamin, and found that cobinamide was five times more potent than hydroxocobalamin, i.e., 12.5 mg/kg of cobinamide was equivalent to 65 mg/kg hydroxocobalamin.

## 60 Minute Survival by Cyanide Treatment Groups

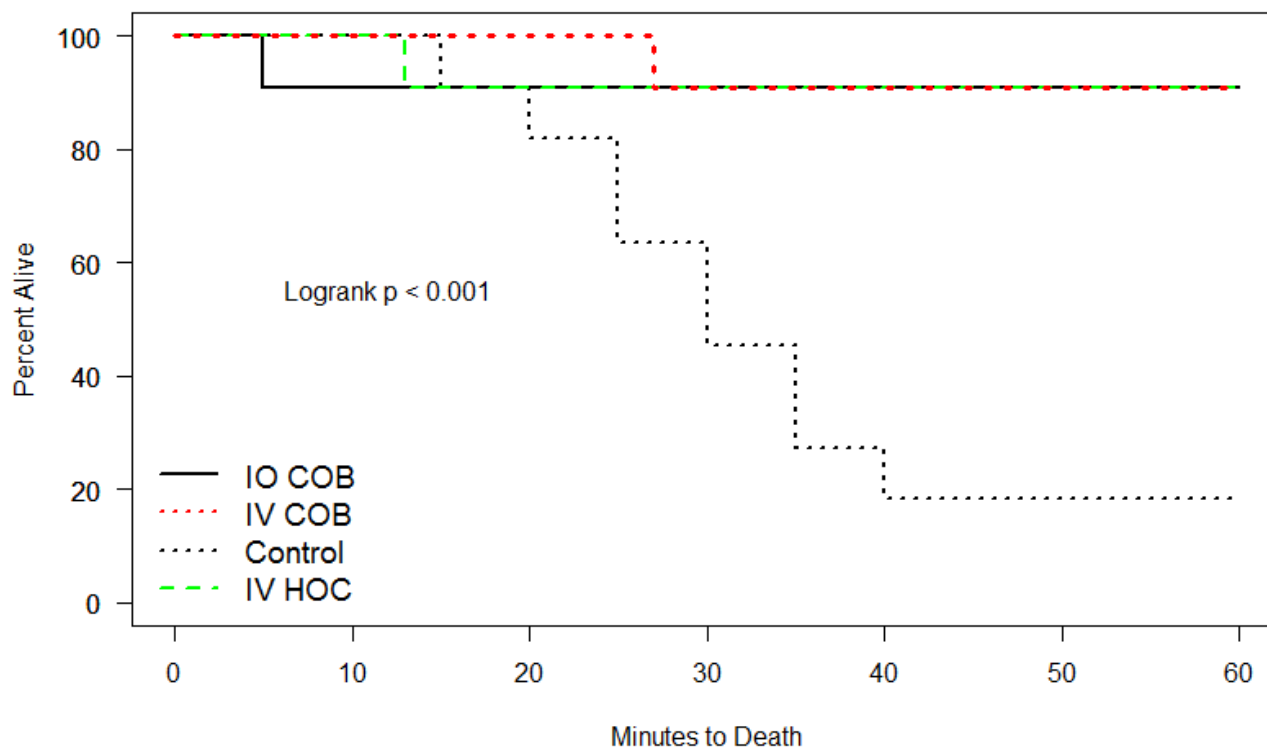


**Figure 2. Intraosseous Injection of Cobinamide Rescues Pigs from Cyanide Poisoning.** Cyanide was given by continuous intravenous injection to 50 kg Yorkshire pigs until one minute beyond the onset of apnea, i.e., apnea plus one minute. The animals then received saline by intraosseous injection (Control, dotted blue line), 12.5 mg/kg cobinamide by intraosseous (IO COB, solid black line) or intravenous injection (IV COB, red dotted line), or 65 mg/kg hydroxocobalamin by intravenous injection (IV HOC, green dashed line). The intraosseous injection was into the tibial plateau using a standard intraosseous injection device. Animals were randomly assigned to each group. A sample size of 11 animals per group was selected based on obtaining a power of 80%, an alpha of 0.05, and an effect size of  $\geq 0.25$  difference (one standard deviation) in mean time to spontaneous breathing. Time to spontaneous breathing and survival were compared using rank methods. Baseline weights (53, 51, 51, 52 kg), time to apnea (10:54, 10:07, 9:49, 10:16 min), and cyanide dose at apnea (1.8, 1.7, 1.7, 1.8 mg/kg) were similar for all four groups (control, IO COB, IV COB, and IV HOC, respectively). At the time of antidote injection, mean blood cyanide (1.7, 1.7, 1.8, 1.7 mcg/ml) and lactate concentrations (3.5, 3.5, 3.1, 3.3 mmol/L), and reduction in mean arterial pressure (MAP) from baseline (29%, 28%, 36%, 32% decrease) were similar for all four groups (again, control, IO COB, IV COB, and IV HOC, respectively). Two of 11 animals in the saline control group survived (18% survival) compared to 10 of 11 survivors in both the intravenous and intraosseous cobinamide groups (91% survival) ( $p < 0.001$  difference between saline- and cobinamide-injected animals). Survival in the intravenous hydroxocobalamin group was also 91%. Time to spontaneous breathing after antidote was similar (intravenous 1:48 min, and intraosseous 1:47 min). Blood cyanide concentrations became undetectable after cobinamide infusion in both groups. No statistically significant differences were detected between the intraosseous and intravenous cobinamide groups for cardiac output, MAP, or minute ventilation, or in lactate (1.3 vs 1.8 mmol/L) and pH (7.44 vs 7.41) at 60 min. We conclude that intraosseous cobinamide is as effective as intravenous cobinamide for treating cyanide-poisoned pigs.

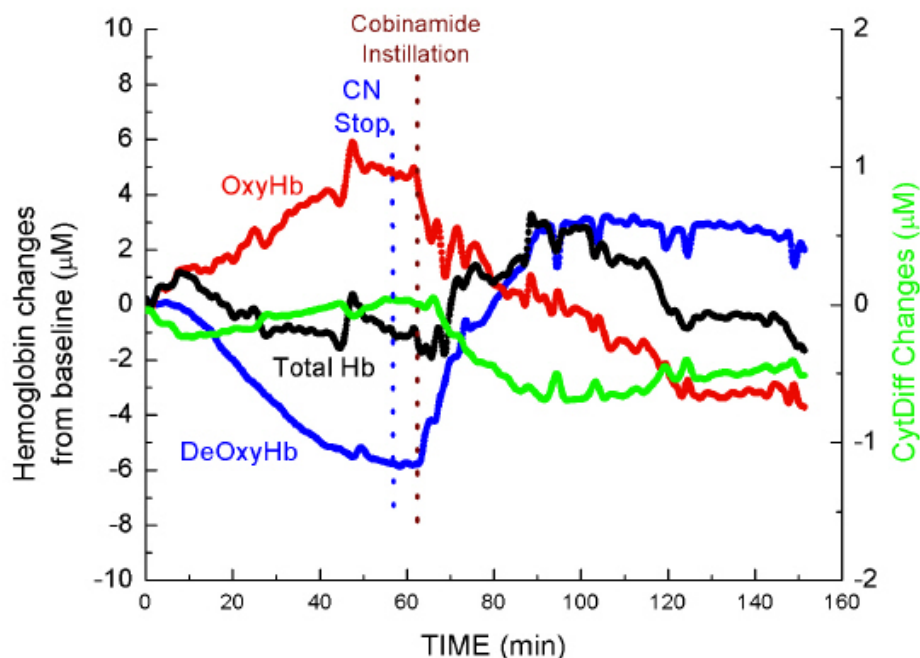
### Inhalational Delivery

Dr. Chen Tsai at the University of California, Irvine has further developed an ultrasonic nebulizer to deliver cyanide antidotes by inhalation (Figure 3, next page). It is a small, pocket-sized device (8.6 x 5.6 x 1.5 cm<sup>3</sup>) that contains a nozzle, electronic driver, cell-phone battery, piezoelectric micro pump, drug reservoir, and liquid feed system. It can deliver flow rates of up to 0.2 ml/min, allowing a cyanide antidote to be given in about five minutes. We have shown that giving cobinamide by this device can successfully rescue rabbits from lethal cyanide doses. In Figure 3, we present data using this nebulizer, showing that it delivers cobinamide quickly to cyanide-poisoned rabbits as evidenced by almost immediate reversal in oxy- and deoxyhemoglobin concentrations. During the second year of the two-year grant, an improved nozzle platform was designed and fabricated. The new platform is considerably smaller in size and capable of incorporating a pair of centimeter-sized nozzles. During the period of the no cost time extension, Dr. Tsai showed that the new nozzle platform

provides a higher delivery rate for a single antidote or can provide simultaneous delivery of separate antidotes such as cobinamide and sulfanegen. As part of Dr. Tsai's work, he generated two journal papers and four proceedings papers.

**Fig. 3. Inhalational Drug Delivery in Rabbits.**

New Zealand white rabbits received a continuous intravenous infusion of cyanide starting at time zero. This caused the oxyhemoglobin concentration to rise and the deoxyhemoglobin concentration to fall. At the indicated time, cobinamide was administered by inhalation through the animal's nasotracheal tube. Note the immediate reversal in the oxy- and deoxyhemoglobin concentrations; this is similar to what is observed after intravenous injection of drug.



**Training and Professional Development Opportunities**

Nothing to report.

**Dissemination of Results**

Results were disseminated via publications and conference presentations as listed under "Products."

**Plans During Next Reporting Period**

Nothing to report.

**IMPACT**

**Impact on Principal Discipline**

The current treatment for cyanide poisoning is to administer an antidote by intravenous injection over 5-10 min. This is not practical for use in the field, and we have shown that cyanide antidotes can be administered by three alternative routes, all of which could be used in the field. Thus, this work could have had a major impact on the treatment of cyanide poisoning.

**Impact on Other Disciplines**

Nothing to report.

**Impact on Technology Transfer**

We have developed a high-flow hand-held ultrasonic nebulizer capable of delivering hundreds of milligrams of drug per minute. This is to be compared with current hand-held nebulizers that can deliver only micrograms of drug per minute.

**Impact on Society**

A cyanide antidote that can be administered quickly in the field is needed urgently. We have shown that three novel cyanide antidotes that are in development can be administered by intramuscular injection, by

intraosseous injection, and by inhalational delivery. Thus, all three delivery modes are viable routes to administer these agents, and this work, could, therefore, have a major impact on the treatment of cyanide poisoning.

## **CHANGES/PROBLEMS**

Nothing to report.

## **PRODUCTS**

### **Journal Publications**

1. Lee, J., Kim, J. G., Mahon, S.B., Mukai, D., Yoon, D., Boss, G.R., Patterson, S.E., Rockwood, G., Isom, G., Brenner, M. Non-invasive optical cytochrome c oxidase redox state measurements using diffuse optical spectroscopy. *J Biomed Opt.* 2014 May;19(5):055001.
2. Tsai, C.S., Mao, R.W., Lin, S.K., Zhu, Y., Tsai, S.C. Faraday instability-based micro droplet ejection for inhalation drug delivery, *Technology*, 2, 75-81, 2014.
3. Bebarta, V., Boudreau, S., Dixon, P., Boss, G. R. Intravenous cobinamide versus hydroxocobalamin for acute treatment of severe cyanide poisoning in a swine (*Sus Scrofa*) model. *Ann. Emergency. Med.*, 64: 612-619, 2014
4. Chan, A, Jiang J., Fridman, A, Guo, L., Shelton, G, Liu, M-T, Green, C, Haushlater, K, Patel, H, Lee J, Yoon, D, Burney, T, Mukai, D, Mahon SB, Brenner M, Pilz RB, and Boss, GR. Development of a cyanide antidote for intramuscular injection. *J. Med. Chem.* 58:1750-1759, 2015.

### **Books**

Nothing to Report

### **Conference Papers and Presentations**

1. Tsai, C.S., Mao, R.W., Zhu, Y.M, Chien, E., Maduzia, J., Tsai, S.C., Brenner, M., Mahon, S., Mukai, D., Lee, J. Yoon, D., Burney, T., Boss, G., Patterson, S. Hand-held high-throughput ultrasonic monodisperse aerosol inhalers for detoxification of massive cyanide poisoning. *IEEE International Ultrasonics Symposium Proceedings, (IUS-2012)* 1632-1634, 2012.
2. Tsai, C.S., Lin, S.K., Mao, R.W., Tsai, S.C., Brenner, M., Mahorn, S., Muka, D., Boss, G. Pocket-Sized Ultrasonic Nebulizer for Inhalation Drug Delivery. *Proc. of the IEEE Int. Ultrasonics Symp. (IUS-2013)*, 1190-1192, 2013.
3. Mao, R.W., Lin, S.K., Tsai, S.C., Brenner, M., Mahorn, S., Boss, G., Smaldone, G., Tsai, C.S. MEMS-Based Silicon Ultrasonic Twin-Nozzle Nebulizer for Inhalation Drug Delivery. *Proc. of the IEEE Int. Ultrasonics Symp. (IUS-2014)*, 742-744, 2014.
4. Tsai, C.S., Mao, R.W., Lin, S.K., Tsai, S.C., Boss, G., Brenner, M., Smaldone, G., Mahon, S., Shahverdi, K., Zhu, Y. Ultrasound-driven megahertz Faraday waves for generation of monodisperse micro droplets and applications. *Proc. of the 2015 Int. Congress on Ultrasonics, Physics Procedia* 70:872-875, 2015.

## **PARTICIPANTS AND OTHER COLLABORATING ORGANIZATIONS**

### **Project Personnel**

The work was a multi-center collaboration among five different institutions. The investigators and their respective institutions are:

United States Army Medical Research Institute of Chemical Defense

Gary Rockwood, Ph.D.; Subproject PI.; Dr. Rockwood provided the dimethyltrisulfide used in the project.

#### University of California, Irvine

Matthew Brenner, M.D.; Subproject PI; Dr. Brenner directed the rabbit experiments.

Jangwoen Lee, Ph.D.; Dr. Lee conducted the rabbit experiments.

Sari Mahon-Brenner, Ph.D. Dr. Mahon-Brenner conducted the rabbit experiments.

Chen Tsai, Ph.D.; Dr. Tsai developed the ultrasonic nebulizer for inhalational drug delivery.

#### University of California, San Diego

Gerry R. Boss, M.D.; Overall project PI and PI at UCSD.

Adriano Chan, B.S.; Mr. Chan performed the mouse experiments and produced the cobinamide used in the project.

#### University of Minnesota'

Steven Patterson, Ph.D.; Subproject PI; Dr. Patterson provided the sulfanegen used in the project.

#### University of Texas, San Antonio

Vikhyat Bebart, M.D.; Subproject PI; Dr. Bebart directed the pig experiments.

Susan Boudreau, R.N.; Ms. Boudreau conducted the pig experiments.

Patricia Dixon, B.S.; Ms. Dixon conducted the pig experiments.

#### **Change in Key Personnel**

Nothing to report.

#### **Other Organizations**

Nothing to report.

#### **SPECIAL REPORTING REQUIREMENTS**

Nothing to report.

#### **APPENDICIES**

The four papers and four conference proceedings listed in "Products" are provided as appendicies.

# Journal of Biomedical Optics

[SPIDigitalLibrary.org/jbo](http://SPIDigitalLibrary.org/jbo)

## **Noninvasive optical cytochrome c oxidase redox state measurements using diffuse optical spectroscopy**

Jangwoen Lee  
Jae G. Kim  
Sari B. Mahon  
David Mukai  
David Yoon  
Gerry R. Boss  
Steven E. Patterson  
Gary Rockwood  
Gary Isom  
Matthew Brenner

# Noninvasive optical cytochrome c oxidase redox state measurements using diffuse optical spectroscopy

Jangwoen Lee,<sup>a,\*</sup> Jae G. Kim,<sup>a,b</sup> Sari B. Mahon,<sup>a</sup> David Mukai,<sup>a</sup> David Yoon,<sup>a</sup> Gerry R. Boss,<sup>c</sup> Steven E. Patterson,<sup>d</sup> Gary Rockwood,<sup>e</sup> Gary Isom,<sup>f</sup> and Matthew Brenner<sup>a,g,\*</sup>

<sup>a</sup>University of California Irvine, Beckman Laser Institute and Medical Clinic, 1002 Health Sciences Road East, Irvine, California 92612

<sup>b</sup>Gwangju Institute of Science and Technology, School of Information and Communications, Department of Medical System Engineering, 123 Cheomdan-gwagiro, Buk-gu, Gwangju 500-712, Republic of Korea

<sup>c</sup>University of California San Diego, Department of Medicine, 9500 Gilman Dr., La Jolla, California 92093

<sup>d</sup>University of Minnesota, Department of Pharmacology, 516 Delaware Street SE, Minneapolis, Minnesota 55455

<sup>e</sup>US Army Medical Research Institute of Chemical Defense, Aberdeen Proving Ground, Maryland 21010

<sup>f</sup>Purdue University, Department of Medicinal Chemistry and Molecular Pharmacology, 575 Stadium Mall Drive, West Lafayette, Indiana 47907

<sup>g</sup>University of California Irvine Medical Center, Department of Pulmonary and Critical Care, 333 West City Boulevard, Suite 400, Orange, California 92868

**Abstract.** A major need exists for methods to assess organ oxidative metabolic states *in vivo*. By contrasting the responses to cyanide (CN) poisoning versus hemorrhage in animal models, we demonstrate that diffuse optical spectroscopy (DOS) can detect cytochrome c oxidase (CcO) redox states. Intermittent decreases in inspired O<sub>2</sub> from 100% to 21% were applied before, during, and after CN poisoning, hemorrhage, and resuscitation in rabbits. Continuous DOS measurements of total hemoglobin, oxyhemoglobin, deoxyhemoglobin, and oxidized and reduced CcO from muscle were obtained. Rabbit hemorrhage was accomplished with stepwise removal of blood, followed by blood resuscitation. CN treated rabbits received 0.166 mg/min NaCN infusion. During hemorrhage, CcO redox state became reduced concurrently with decreases in oxyhemoglobin, resulting from reduced tissue oxygen delivery and hypoxia. In contrast, during CN infusion, CcO redox state decreased while oxyhemoglobin concentration increased due to CN binding and reduction of CcO with resultant inhibition of the electron transport chain. Spectral absorption similarities between hemoglobin and CcO make noninvasive spectroscopic distinction of CcO redox states difficult. By contrasting physiological perturbations of CN poisoning versus hemorrhage, we demonstrate that DOS measured CcO redox state changes are decoupled from hemoglobin concentration measurement changes. © The Authors. Published by SPIE under a Creative Commons Attribution 3.0 Unported License. Distribution or reproduction of this work in whole or in part requires full attribution of the original publication, including its DOI. [DOI: 10.1117/1.JBO.19.5.055001]

**Keywords:** diffuse optical spectroscopy; cytochrome c oxidase; physiological perturbation; cyanide poisoning; hemorrhage.

Paper 130482RR received Jul. 10, 2013; revised manuscript received Mar. 1, 2014; accepted for publication Mar. 7, 2014; published online May 1, 2014.

## 1 Introduction

Cyanide (CN) based derivatives have been used for centuries as poisons and chemical weapons.<sup>1,2</sup> CN continues to pose a major potential chemical threat to civilians and military personnel.<sup>2,3</sup> The mechanisms of CN toxicity are complex.<sup>4,5</sup> A main target of CN toxicity is CN impairment of the ability of tissues to utilize oxygen through inhibition of cytochrome c oxidase (CcO).<sup>3</sup> CcO is the terminal oxidase of the mitochondrial respiratory chain and transfers electrons from ferrocytochrome c to molecular oxygen.<sup>6</sup> CcO is involved in >95% of the oxygen consumption in the body and is essential for the efficient generation of cellular ATP.<sup>7</sup> CN has a high binding affinity for active sites on CcO. Progressive cytotoxic tissue hypoxia develops quickly after CN binding and immediate intervention is necessary to prevent toxicity and death.<sup>8</sup> Thus, the need for rapid identification of patients exposed to CN and ability to continuously monitor the response to treatment in field or hospital settings is critical. This need is compounded by the potentially large number of people with significant risks of severe injury from intentional or accidental mass casualty exposure events.

Moreover, the ability to measure CcO redox state *in vivo* is an important unmet need in clinical and research medicine. CcO redox status is a direct reflection of adequacy of tissue perfusion, oxygenation, and cellular metabolic status at the mitochondrial level. Investigators have sought accurate methods to noninvasively monitor the CcO redox status to determine whether the tissue and organs are in healthy, stressed, or diseased states.<sup>9–19</sup> In order to guide diagnostics, therapeutics, and resuscitation, noninvasive and continuous measurements of CcO redox state would be optimal.

Since CcO contains four redox active metal centers (two heme and copper groups respectively) and these metal centers give rise to absorption bands in ultraviolet, visible, and near-infrared (NIR) regions, photonics based technologies such as near-infrared spectroscopy (NIRS) have utilized the unique absorption spectra of the oxidized and reduced states of CcO in order to attempt to determine the physiological oxygenation status of tissue and organs *in vivo*.<sup>9,16,20</sup>

This change of absorption spectra associated with CcO redox state changes presents a potential noninvasive diagnostic opportunity for diffuse optical spectroscopy (DOS).<sup>21–23</sup> DOS combines multifrequency frequency domain photon migration (FDPM) with time-independent NIRS to quantitatively measure bulk tissue absorption and scattering spectra. DOS has been

\*Address for correspondence to: Jangwoen Lee, E-mail: [jangwl@uci.edu](mailto:jangwl@uci.edu); Matthew Brenner, E-mail [mbrenner@uci.edu](mailto:mbrenner@uci.edu)



applied to various clinical situations including breast cancer monitoring and clinical care monitoring. Especially in clinical care monitoring, it has been successfully employed in monitoring hemorrhage and fluid resuscitation,<sup>24,25</sup> the formation and treatment of methemoglobinemia,<sup>26</sup> and CN poisoning by quantifying the tissue concentrations of hemoglobin species and relevant chromophores.<sup>27,28</sup>

In addition, we have used DOS measurements of tissue hemoglobin concentrations during CN poisoning and treatment phases in order to determine the efficacy of various CN antidotes.<sup>29–31</sup> Although DOS and continuous wave NIRS measurements have proven valuable to determine the effectiveness of CN antidotes, we have relied primarily on the kinetics of oxy- and deoxyhemoglobin concentration changes such as decay time constants after the antidote injection. However, the changes in tissue hemoglobin concentrations at the onset of CN poisoning also includes other confounding factors such as cardiovascular changes and severe metabolic acidosis which, in turn, can affect tissue hemoglobin concentrations. Therefore, the assessment of CcO redox states would potentially show cellular metabolic status during CN poisoning and the effects of CN antidotes more directly.

CN has been used previously in NIRS measurement of CcO *in vivo* as a CcO and electron transport chain inhibitor.<sup>13,14,32</sup> CN poisoning presents a unique situation with regard to CcO and hemoglobin oxygenation. During CN poisoning, tissues are unable to extract oxygen from hemoglobin and optical measures of tissue hemoglobin saturation increase,<sup>27,29–31</sup> while principal electron transport chain cytochromes are reduced.<sup>14,33</sup> As the four metal centers in the CcO undergo changes in redox state during CN poisoning, they change absorption spectra. As CN binds to Cyt a3 of CcO, it prevents oxygen reduction of the electrons leaving CuA.<sup>34</sup> As a result, the CuA center, which accounts for the majority of the NIR absorption signal of CcO, becomes reduced.<sup>32,35,36</sup>

Unfortunately, noninvasive spectroscopic monitoring of CcO redox information *in vivo* has been limited by (i) a lack of clearly valid gold standard cytochrome oxidase measures for comparison and (ii) major concerns regarding optical interference from “cross talk” from dominant hemoglobin and myoglobin absorption signals in tissues.<sup>16,37</sup>

The objective of this study is to provide evidence for the validity of *in vivo* measurement of cytochrome oxidase redox state changes during CN poisoning with DOS in peripheral muscle. We report a series of experiments designed to noninvasively assess CcO redox states *in vivo* and demonstrate independence from hemoglobin (or myoglobin) “optical crosstalk” using DOS. These studies involve a combination of CN poisoning, hemorrhage, and alterations in inspired oxygen concentration in animal models undergoing continuous DOS monitoring.

Under most clinical conditions, CcO redox state changes parallel to those of hemoglobin oxygen delivery and supply to the tissues. Therefore, it has not been possible to convincingly demonstrate that optical signals that are presumed to be generated from CcO redox state changes are independent from changes in hemoglobin (or myoglobin in muscle) redox state measurements.<sup>14</sup> For example, during hemorrhage, reduction in tissue hemoglobin-based oxygen delivery, increase in tissue oxygen extraction coefficients, and decreased tissue hemoglobin (and/or myoglobin) oxygenation are associated with concurrent reduction in tissue cytochrome oxidation state.<sup>14</sup> This is particularly important, since hemoglobin absorption in the NIR region

has been reported to be approximately an order of magnitude higher than the cytochrome absorption signals.<sup>14,37</sup> A similar parallel change in redox states for hemoglobin and CcO occurs during reduction in inspired oxygen, and other hypoxemic or hypoperfusion states. Thus, it has not been possible in these scenarios to clearly separate photonics-based measured changes in CcO from hemoglobin redox state changes with certainty.

CN poisoning presents a unique situation with regard to CcO and hemoglobin oxygenation. During CN poisoning, tissues are unable to extract oxygen from hemoglobin and tissue hemoglobin saturations increase, while principal electron transport chain cytochromes are reduced. Thus, during CN poisoning, hemoglobin (and/or myoglobin) oxygenation states change in the opposite direction of CcO redox state.<sup>14</sup>

Therefore, by contrasting the differences of DOS based optical CcO redox state between hemorrhage-induced CcO and hemoglobin redox signals against CN-induced changes, together with the response to varying inhaled oxygen concentrations, it is possible to demonstrate uncoupling of these optical signals as demonstrated in this study.

## 2 Materials and Methods

The methods for CN induction and DOS monitoring in rabbits have been previously described<sup>27</sup> and are summarized here.

### 2.1 Rabbit Studies

The protocol was reviewed and approved by the University of California Irvine (UCI) Institutional Animal Care and Use Committee (IACUC). Fourteen pathogen-free New Zealand white rabbits (Western Oregon Rabbit Supply, Philomath, Oregon), weighing  $3.76 \pm 0.03$  kg (mean  $\pm$  standard error of mean) were used in this study. Animals were anesthetized with an intramuscular injection of Ketamine HCl 50 mg/kg (Ketaject, Phoenix Pharmaceutical Inc., St. Joseph, Michigan) and Xylazine 5 mg/kg (Anased, Lloyed Laboratories, Shenandoah, Iowa). After the injection, a catheter was placed in the animal's marginal ear vein to administer continuous intravenous anesthesia with Ketamine/Xylazine. Animals were mechanically ventilated (dual phase control respirator, model 32A4BEPM-5R, Harvard Apparatus, Chicago, Illinois) at a rate of 20 respirations per min, a tidal volume of 50 cc, and inspired O<sub>2</sub> concentration of 100%. A pulse oximeter (Biox 3700 Pulse Oximeter, Ohmeda, Boulder, Colorado) with a probe was placed on the tongue, to measure SpO<sub>2</sub> and heart rate.

Rabbits were anesthetized, intubated, ventilated, and monitored with continuous DOS measurements of oxyhemoglobin, deoxyhemoglobin, lipid, water content measurements as well as CcO redox states. Measurements were obtained from the DOS probe placed over the right thigh muscle region. Monitoring of blood pressure and blood gas sampling were accomplished through femoral arterial and venous lines. Respiratory challenges, with intermittent decreases (5 min) in inspired O<sub>2</sub> from 100% to 21%, were applied before, during hemorrhage and resuscitation (in hemorrhage study animals), as well as before, during, and after CN infusion (in CN study animals).

### 2.2 Control Animals

Control animals ( $n = 5$ ) received neither CN nor hemorrhage, but were monitored throughout the same time period as



treatment animals and underwent respiratory challenges at the corresponding time points.

### 2.3 Hemorrhage Rabbit Studies

Hemorrhage studies were conducted in rabbits ( $n = 4$ ) with stepwise (eight steps of 5 mL) removal of a total of 40 mL (~20% blood volume) over 60 min, followed by resuscitation with return of the whole blood by continuous infusion over 60 min (0.66 mL/min). Respiratory challenges, with decreases in inspired  $O_2$  from 100% to 21%, were applied for 5 min three times during hemorrhage and resuscitation phases.

### 2.4 CN Rabbit Studies

For CN rabbit studies ( $n = 5$ ), 10 mg of sodium CN in 60 cc normal saline was infused through the femoral vein at a rate of 1 cc/min (0.167 mg NaCN/min). Respiratory challenges were applied as described above; before, during, and after CN infusion. Changes in hemoglobin concentrations and CcO redox states were monitored continuously with DOS.

### 2.5 DOS Measurements in Rabbit Animal Models

DOS measurements were obtained through a fiber-optic probe with a diode light emitter and the detector at a fixed distance (10 mm) from the source fiber. The probe was placed on the shaved surface of the right inner thigh of the animal for muscle measurements.

The broadband DOS system we constructed combines multi-frequency FDPM with time-independent NIRS to measure bulk tissue absorption and scattering spectra.<sup>26,27,38–41</sup> It employs five laser diodes at discrete wavelengths (660, 685, 786, 822, and 852 nm), and a fiber-coupled avalanche photodiode (APD) detector (Hamamatsu high-speed APD module C5658, Bridgewater, New Jersey) for the frequency domain measurements. Absorption and reduced scattering coefficients are measured directly at each of the five laser diode wavelengths using frequency-dependent phase and amplitude data. Steady-state acquisition was a broadband reflectance measurement from 650 to 1000 nm that follows frequency domain measurements using a tungsten-halogen light source (Ocean Optics HL-2000, Dunedin, Florida) and a spectrometer (BWTEK BTC611E, Newark, Delaware). Intensity of the steady-state reflectance measurements is calibrated to the frequency domain values of absorption and scattering to establish the absolute reflectance intensity.<sup>27,38,39</sup> The acquisition time is ~10 s for the frequency

domain measurements and broadband steady-state measurement combined for each measurement.

The key challenges for *in vivo* optical monitoring of CcO redox changes come from the fact that there is a significant overlap in the NIR spectra of hemoglobin and the respiratory chain. Concurrent changes in hemoglobin saturation or volume with CcO redox shift would produce complex spectral changes dominated by hemoglobin due to its high content and high intrinsic absorption. We have made several changes from the previous DOS measurement for CcO redox states changes during CN poisoning.<sup>28</sup> The broadband reflectance measurement was carried out between 650 and 1000 nm focusing on the NIR absorptions centered at 830 nm, which are associated with the  $Cu_A$  center.<sup>16</sup> Absorption below 650 nm was excluded from data processing to avoid potential complications from the much stronger absorption changes due to cyt a and cyt  $a_3$  in this region, which could confuse the interpretation of the NIR spectra which are predominantly from  $Cu_A$ .<sup>9,32</sup>

At the baseline, broadband reduced scattering coefficients are calculated as a function of wavelength throughout the NIR region (650 to 1000 nm) by fitting a power-law to five discrete frequency domain reduced scattering coefficients and are used throughout the entire data analysis to extract absorption spectra. At each subsequent measurement, the difference absorption spectra are calculated with respect to baseline values. Finally, the changes in chromophore concentrations as well as changes in CcO redox states are calculated from the difference absorption spectra by a linear least squares fit of the wavelength-dependent extinction coefficient spectra of each chromophore in the current approach. We used published absorption spectra for hemoglobins,<sup>42</sup> water,<sup>43</sup> lipid,<sup>44</sup> and difference spectra of CcO (Ref. 45) (downloaded from <http://www.ucl.ac.uk/medphys/research/borl/intro/spectra>) for the subsequent fitting and analysis.

## 3 Results

Table 1 presents the baseline chromophore concentration values from DOS measurements in the three rabbit models. Tissue oxyhemoglobin (OxyHb) and deoxyhemoglobin (DeOxyHb) concentrations undergo changes during physiological challenges as shown in the following figures. The water fraction, the water concentration in tissue relative to the concentration of pure water (55.6 M) and the lipid fraction, the lipid mass density ( $g\ mL^{-1}$ ) in tissue relative to a lipid mass density of  $0.9\ g\ mL^{-1}$ , remain fairly constant. Water and lipid fraction varied less than 4% and 2%, respectively. Table 1 also lists the parameters associated with the power-law fit of five discrete

**Table 1** Baseline chromophore concentration values from DOS measurements in the three rabbit models. The water fraction is the water concentration in tissue relative to the concentration of pure water (55.6 M) and the lipid fraction is the lipid mass density ( $g\ mL^{-1}$ ) in tissue relative to a lipid mass density of  $0.9\ g\ mL^{-1}$ . DeOxyHb, OxyHb, and THb represent deoxyhemoglobin, oxyhemoglobin, and total hemoglobin (OxyHb + DeOxyHb), respectively. Parameters associated with the power-law fit of five discrete frequency domain reduced scattering coefficients at baseline, prefactor ( $A$ ), and scattering power (SP) where  $\mu'_s(\lambda) = A\lambda^{-SP}$ , from three rabbit models are also listed. Data are presented as mean  $\pm$  SEM (standard error of mean). Numbers of animals in control, CN (10 mg), and hemorrhage are 5, 5, and 4, respectively.

	Lipid (%)	Water (%)	DeOxyHb ( $\mu M$ )	OxyHb ( $\mu M$ )	THb ( $\mu M$ )	$A$	SP
Control	$14.3 \pm 0.97$	$85.4 \pm 2.74$	$13.6 \pm 1.01$	$18.7 \pm 2.79$	$32.2 \pm 2.02$	$7170 \pm 6660$	$-1.19 \pm 0.16$
CN (10 mg)	$18.1 \pm 3.42$	$79.5 \pm 2.78$	$11.3 \pm 1.44$	$17.3 \pm 1.66$	$28.6 \pm 2.73$	$2220 \pm 2210$	$-0.98 \pm 0.14$
Hemorrhage	$17.4 \pm 2.66$	$85.8 \pm 4.84$	$10.7 \pm 1.35$	$21.6 \pm 0.82$	$32.3 \pm 2.14$	$11,220 \pm 9134$	$-1.32 \pm 0.18$

**Table 2** Physiological values of control animals ( $n = 5$ ). Mean arterial pressure (mAP), heart rate (HR), and arterial and venous blood gas measurements ( $\text{PO}_2$ , partial pressure of  $\text{O}_2$ ; BE, base excess; pH) at baseline and 10, 55, and 85 min after the completion of saline infusion are listed. The subscripts a and v designate arterial and venous values, and bpm indicates beats per minute of the heart rate. Data are presented as mean  $\pm$  SEM. One-way repeated measures analysis of variance (ANOVA) test are performed for physiological parameters presented in this table and the significant mean differences among four time points are reported at the 0.05 significance level.

	Baseline		Post 10 min		Post 55 min		Post 85 min	
	Mean	SEM	Mean	SEM	Mean	SEM	Mean	SEM
$\text{P}_a\text{O}_2$ (mm Hg)	607.6	32.7	587.0	28.5	580.6	20.9	602.2	10.8
$\text{BE}_a$ (mM)	5.3	2.42*	2.5	1.56	1.8	1.76	0.5	2.25*
$\text{P}_v\text{O}_2$ (mm Hg)	49.7	3.40	51.4	3.51	51.7	4.95	50.4	4.16
pH <sub>v</sub>	7.47	0.03	7.42	0.04	7.37	0.05	7.37	0.05
$\text{BE}_v$ (mM)	6.2	1.78*†	3.4	1.68	1.7	1.76*	1.6	1.90†
mAP (mm Hg)	70.6	5.56*	64.5	5.63	65.5	7.09	56.8	5.95*
HR (bpm)	148.0	5.87	144.2	6.13	141.6	5.68	151.8	8.36

Note: Symbols (\* and †) are used to indicate the significant mean difference at the 0.05 level from pairwise comparisons

frequency domain reduced scattering coefficients at a baseline in order to obtain broadband reduced scattering coefficients for subsequent measurement and analysis. The power-law fit coefficients, prefactor ( $A$ ), and scattering power (SP) [ $\mu_s'(\lambda) = A\lambda^{-\text{SP}}$ ] from three rabbit experiments are reported in Table 1.

Tables 2 and 3 list the key physiological values from arterial and venous blood gas analysis of control and CN infused animal groups, respectively. One-way repeated measures analysis of variance test are performed for physiological parameters presented in Tables 2 and 3. At the 0.05 significance level, the significant mean differences between groups are reported. From blood gas analysis data of CN infused animal groups (Table 3), notable changes are observed after CN infusion in arterial and venous base excess values, and mean arterial pressure after CN infusion. The changes in these parameters are indicative of CN toxic effects.<sup>27</sup>

Optical properties from DOS of all 14 animals at baseline are presented in Fig. 1. Figure 1(a) shows the baseline broadband scattering coefficients of frequency domain measurement (mean  $\pm$  standard deviation) and power-law fit estimated broadband reduced scattering coefficient at baseline (mean, blue line). Absolute broadband absorption spectra (mean  $\pm$  standard deviation) at baseline are shown in Fig. 1(b). Black circles (in every 5 nm), blue line, and red dots represent measured absorption coefficients, DOS fitted absorption coefficients and residuals (measured—DOS fitted absorption coefficient), respectively. Figure 1(c) shows the estimated differential path-length factor (DPF) of all 14 animals at the baseline (mean  $\pm$  standard deviation) at five discrete wavelengths used for the frequency domain measurements of DOS. DPFs are estimated using the baseline absorption and reduced scattering coefficients and the equation described by Fantini et al.<sup>46</sup> The distance

**Table 3** Physiological values of CN infused animals ( $n = 5$ ). Mean arterial pressure (mAP), heart rate (HR), and venous blood gas measurements ( $\text{PO}_2$ , partial pressure of  $\text{O}_2$ ; BE, base excess; pH) at baseline and 10, 55, and 85 min after the completion of CN infusion are listed. The subscripts a and v designate arterial and venous values, and bpm indicates beats per minute of the heart rate. Data are presented as mean  $\pm$  SEM. One-way repeated measures ANOVA test are performed for physiological parameters presented in this table and the significant mean differences among four time points are reported at the 0.05 significance level.

	Baseline		Post CN 10 min		Post CN 55 min		Post CN 85 min	
	Mean	SEM	Mean	SEM	Mean	SEM	Mean	SEM
$\text{P}_a\text{O}_2$ (mm Hg)	527.9	31.7	581.0	28.1	541.7	32.2	583.4	19.0
$\text{BE}_a$ (mM)	4.8	0.66*†	−3.8	1.79*	−2.2	1.40†	−0.4	0.91
$\text{P}_v\text{O}_2$ (mm Hg)	51.6	2.78	53.4	2.42	56.0	3.23	58.5	4.16
pH <sub>v</sub>	7.41	0.02	7.39	0.04	7.35	0.03	7.36	0.04
$\text{BE}_v$ (mM)	5.9	0.58*†	−3.4	1.99*§	−0.3	1.57*†	0.7	0.97*§
mAP (mm Hg)	76.5	4.37*†	53.2	2.81	55.9	3.12*	60.1	3.82†
HR (bpm)	136.2	8.22*	159.4	12.06*	153.4	12.90	144.2	11.48

Note: Symbols (\*, †, ‡, and §) are used to indicate the significant mean difference at the 0.05 level from pairwise comparisons

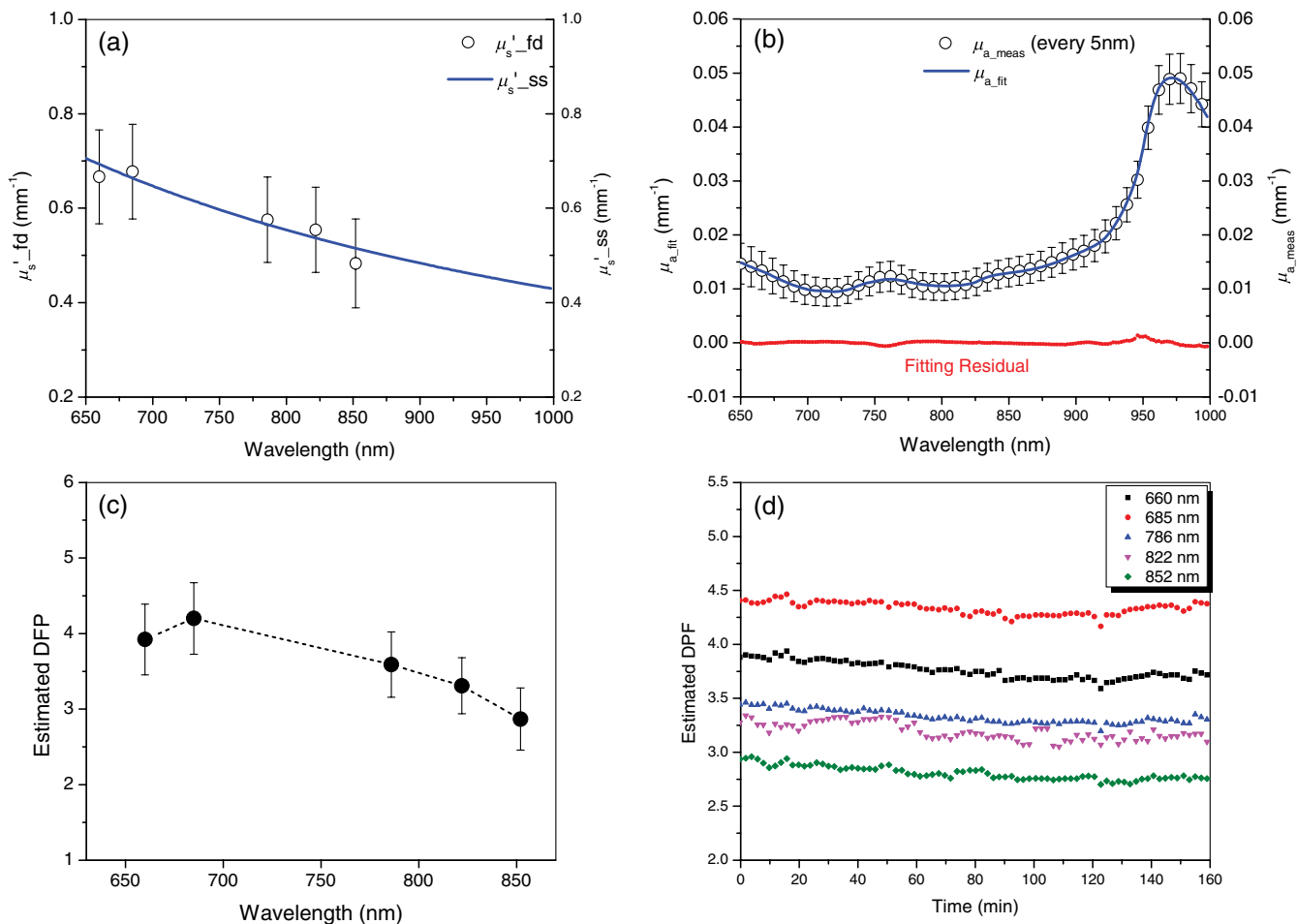


**Fig. 1** Optical properties from diffuse optical spectroscopy (DOS) of all 14 animals at the baseline. (a) Baseline broadband scattering coefficients of frequency domain measurement (mean  $\pm$  standard deviation) and power-law fit estimated broadband reduced scattering coefficient at baseline (mean, blue line), (b) absolute broadband absorption spectra (mean  $\pm$  standard deviation) at baseline are shown. Black circles (in every 5 nm), blue line, and red dots represent measured absorption coefficients, DOS fitted absorption coefficients and residuals (measured—DOS fitted absorption coefficient), respectively. (c) Estimated differential pathlength factor (DPF) of all 14 animals at the baseline (mean  $\pm$  standard deviation) of five discrete wavelengths used for frequency domain measurements of DOS. DPFs are estimated using the baseline absorption and reduced scattering coefficients and the equation described by Fantini et al. (Ref. 46). The distance between source and detector is 10 mm. (d) Time profile of the estimated DPF of five discrete wavelengths used in DOS measurement. Data are from a single animal in the 10 mg cyanide (CN) group. The distance between the source and detector is 10 mm and the equation described by Fantini et al. is used for the estimation.

between the source and detector is 10 mm. Figure 1(d) shows the time profile of the estimated DPF of five discrete wavelengths used in DOS measurement. Data are from a single animal in the 10 mg CN group.

Figure 2(a) shows the changes in tissue oxy- and deoxyhemoglobin concentrations during hemorrhage and resuscitation in rabbits. In the four hemorrhaged rabbits, tissue OxyHb decreased by  $7.47 \pm 0.87 \mu\text{M}$ , and DeOxyHb increased by  $3.73 \pm 0.99 \mu\text{M}$ . As a result, tissue hemoglobin oxygen saturation ( $S_{\text{T}O_2}$ ) decreased by  $15.1 \pm 4.59\%$ . Also shown in Fig. 2(a) is the time course changes in tissue water fraction of hemorrhage group animals. Although hemorrhage and resuscitation with whole blood has impacted the tissue oxy- and deoxyhemoglobin concentrations and tissue oxygen saturation, the water fraction has stayed steady at the baseline level, which is consistent with the results from our previous study.<sup>47</sup> Figure 2(b) shows the

concurrent changes in CcO redox state. The change in CcO redox state parallels the change in OxyHb during hemorrhage and resuscitation: the redox state of CcO becomes increasingly reduced during hemorrhage ( $-0.69 \pm 0.21 \mu\text{M}$  at the end of hemorrhage) and recovers toward baseline values during whole blood resuscitation ( $-0.24 \pm 0.14 \mu\text{M}$  at the end of resuscitation). Figure 2 also shows the effect of inspired oxygen concentration challenge during hemorrhage and resuscitation phases. Starting time points of each inspired oxygen challenges are indicated with red arrows. During a reduction in supplemental inspired oxygen respiratory challenge from 100% to 21%  $\text{O}_2$ , DOS monitoring reveals a decrease in OxyHb and increase in DeOxyHb concentrations. Concurrently, CcO redox state becomes reduced under these challenges.

Figures 3 and 4 demonstrate changes in tissue hemoglobin concentrations and CcO redox state during saline and CN

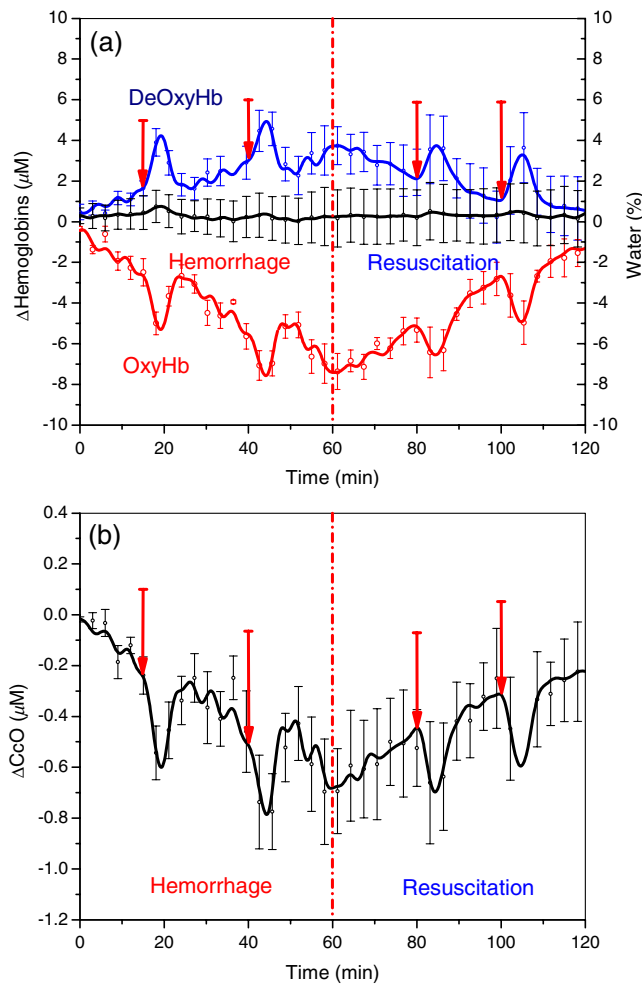


**Fig. 2** Changes in tissue oxy- and deoxyhemoglobin (OxyHb, DeOxyHb) concentrations and concurrent changes in CcO redox state during hemorrhage in the rabbit model ( $n = 4$ ). Error bars represent standard error of mean (SEM). Blood volume (40 cc) was removed over 60 min in eight steps via a left femoral artery catheter, and DOS measurements were taken with the probe placed on the right inner thigh muscle. Resuscitation was carried out by continuously infusing autologous blood back to the animal at the rate of 1 mL/min. Inspired oxygen concentration challenges, where oxygen concentration is decreased briefly from 100% to 21%, were carried out during the hemorrhage and whole blood resuscitation. OxyHb changes parallel changes in CcO redox state during hemorrhage.

infusion in respective animal models. Saline and NaCN solutions were infused at a rate of 1 cc/min.

During saline infusion shown in Fig. 3(a), DeOxyHb (blue line) and OxyHb (red line) demonstrate responsiveness to respiratory challenges. DeOxyHb increases during the relative “hypoxic” phase created by reduction of inspired oxygen concentration from 100% to 21%, and returns to baseline values once inspired oxygen concentration is returned back to 100% oxygen. OxyHb responds to respiratory challenges in the opposite direction. CcO redox state in Fig. 3(b) becomes reduced during the relative reduction in inspired oxygen phase and returns to baseline once inspired oxygen concentration is restored to 100%.

Figure 4 shows changes in OxyHb and DeOxyHb concentrations, and CcO redox state responses during CN infusion. In Fig. 4(a), the red curve shows the overall increase in

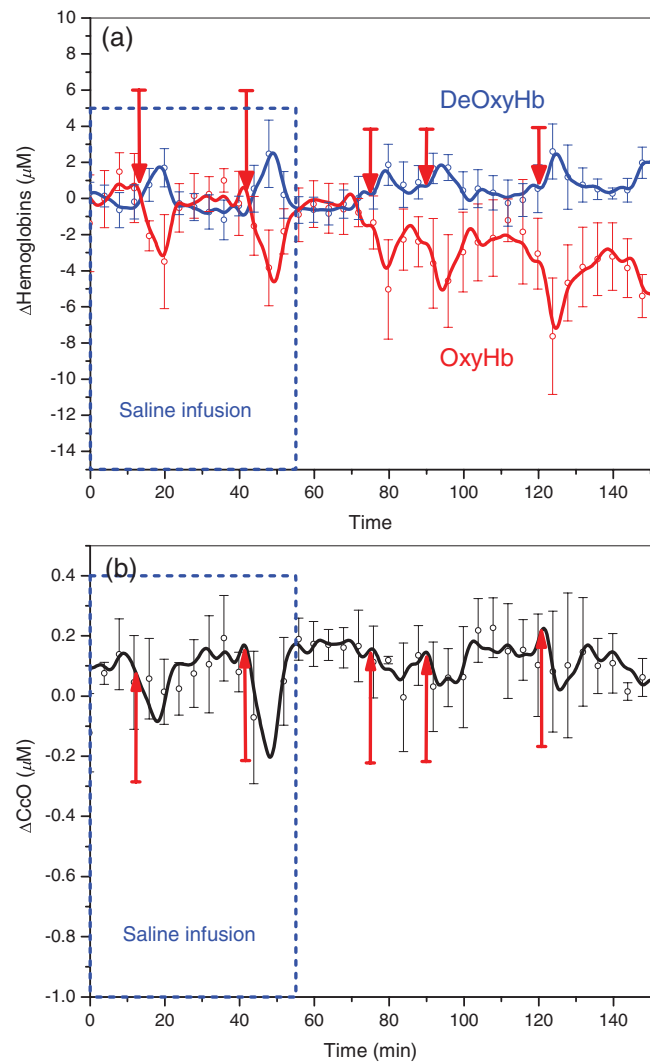


**Fig. 3** Changes in hemoglobin concentration and CcO redox state during saline infusion (60 cc) and inspired oxygen concentration challenges in the control animal group ( $n = 5$ ). During saline infusion, no significant change occurs in OxyHb, DeOxyHb, or CcO redox state until the inspired oxygen concentration is decreased briefly from 100% to 21% ( $F_iO_2$  challenges indicated by red arrows). During the  $F_iO_2$  challenges,  $\Delta$ CcO changes in parallel with changes in OxyHb concentration.

the OxyHb concentration during CN infusion from 0 to 60 min as animals become progressively CN toxic from 0.167 mg NaCN/min infusion. Conversely, DeOxyHb concentration decreases during CN poisoning due to the inability to extract oxygen from circulating blood in the tissues. Under a “relative” hypoxic respiratory challenge on 21%  $O_2$ , continuous DOS monitoring reveals a decrease in OxyHb and increase in DeOxyHb concentrations in CN exposed animals. Concurrently, CcO redox state becomes reduced under these challenges indicated by negative  $\Delta$ CcO values shown in Fig. 4(b). Combined continuous DOS readings show that OxyHb rises during CN infusion, but drops during respiratory challenges.

This composite effect demonstrates uncoupling of the hemoglobin oxygen signal changes from CcO redox state signals because the CcO redox state becomes reduced with both CN infusion and respiratory challenges, in contrast to the hemoglobin oxygenation state.

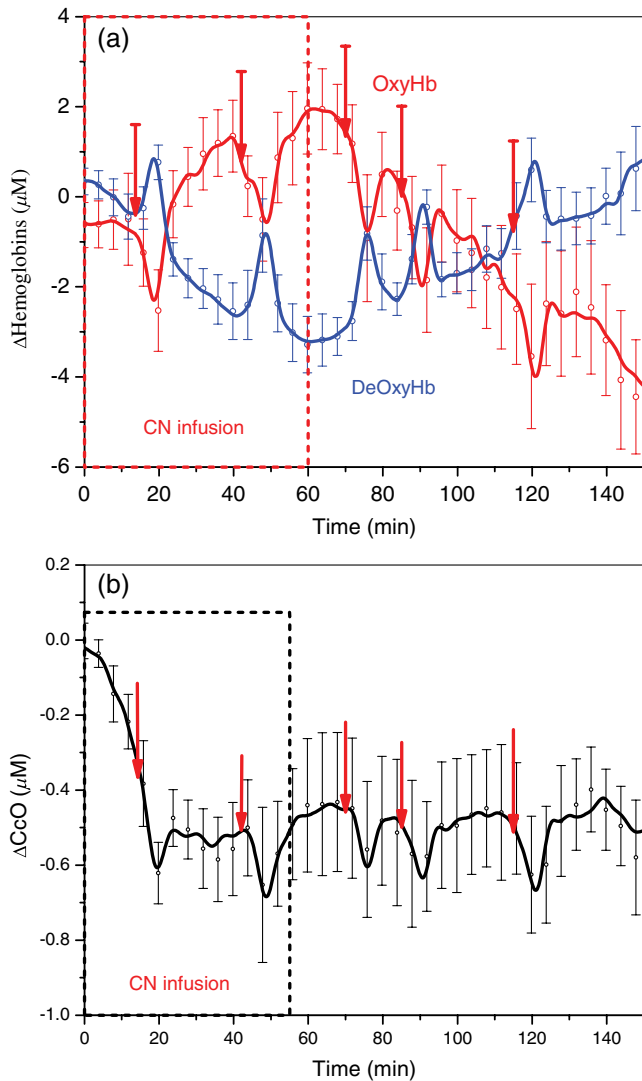


**Fig. 4** Changes in hemoglobin concentrations and CcO redox state during CN poisoning and inspired oxygen concentration challenges in 10 mg CN group ( $n = 5$ ). Ten milligrams of sodium CN is infused continuously at a rate of 1 cc/min. Animals receive progressively increasing amount of CN (0.167 mg NaCN/min) for 60 min. (a and b) Changes in OxyHb and DeOxyHb concentrations and  $\Delta$ CcO changes, respectively. Error bars represent standard error of mean (SEM). During CN infusion, OxyHb changes trend opposite direction of  $\Delta$ CcO change. However, during  $F_{I}O_2$  challenges the transient drops in OxyHb are accompanied by similar directional changes in  $\Delta$ CcO.

Finally, Fig. 5 shows the extracted difference absorption spectra of CcO redox state, DOS fit of difference CcO redox state, and resultant fitting residual after the animal was infused with 8.1 mg of sodium CN, which corresponds to 48.6 min after CN infusion started. From measured difference  $\mu_a$  spectrum, the absorption contribution from all other chromophores (oxy- and deoxyhemoglobin, water, and lipid) was subtracted to extract absorption signal contributed by changes in the redox state of CcO (black circles). These extracted CcO redox state absorption spectra are compared with DOS fit of CcO redox state changes (blue line). DOS fit of CcO redox state change is the product of the extinction coefficient at each wavelength and the tissue concentration of each animal ( $-0.62 \pm 0.30 \mu$ M, mean  $\pm$  SD). The extracted difference absorption spectra of CcO redox state

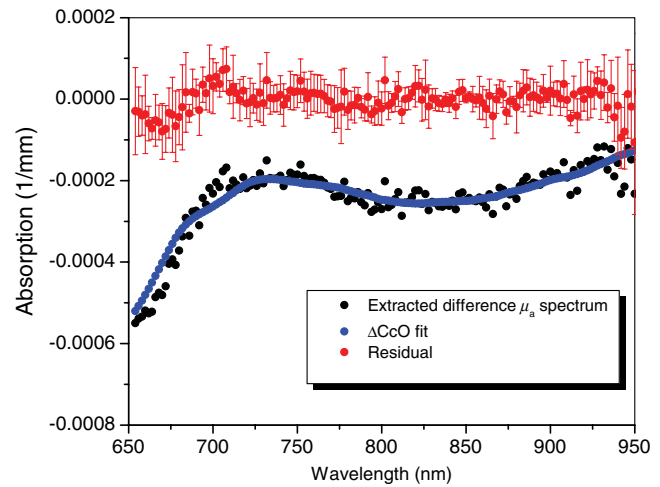


**Fig. 5** The extracted difference absorption spectra of CcO redox state (black circles), DOS fit of difference CcO redox state (blue line), and resulting fitting residual (red solid circles) after the animal was infused with 8.1 mg of sodium CN (48.6 min after CN infusion started). Change in  $\Delta$ CcO is  $-0.62 \pm 0.30 \mu$ M from DOS fitting. Mean values of fitting residual (red solid circle) and standard deviation (error bar) are also shown in this figure.

match spectral features and shape of difference CcO  $\mu_a$  spectrum used for concentration fitting. Red solid circles represent the residual between extracted CcO redox state absorption spectrum and DOS fit from all five animals (mean  $\pm$  SD). It is interesting that the residual test of DOS fitting in Fig. 4 shows the spectral features associated with binuclear center (cyt<sub>a3</sub>/Cu<sub>B</sub>) at 655 nm as well as the weaker and broad NIR Cu<sub>A</sub> band at 830 nm. Figure 5 demonstrates that DOS can measure the changes in CcO redox states in the presence of background chromophore concentration changes in NIR wavelength region between 650 and 1000 nm effectively.

## 4 Discussion

This study was designed to advance the development of *in vivo* noninvasive optical assessment of CcO redox state. The findings demonstrate that changes in CcO redox state signal can be detected and differentiated from background hemoglobin signal changes under a variety of experimental stress conditions.

As expected, during hemorrhage, the tissue concentration of OxyHb decreases and DeOxyHb increases. During hemorrhage, there is vasoconstriction, reduction in cardiac output and reduction in intravascular total hemoglobin concentration. Since DOS measures the bulk average values of OxyHb, DeOxyHb, and total hemoglobin within the interrogation volume of the tissue, this results in a decrease in the measured total tissue hemoglobin concentration.<sup>24</sup> With the reduction in tissue hemoglobin oxygen delivery to the tissues, increased tissue extraction of oxygen from hemoglobin occurs. All of these factors contribute to a reduction of total oxyhemoglobin content within the tissues measured by DOS; although arterial oxygen saturation is not affected, DOS measures a combination of arterial, capillary, and venous OxyHb, and total quantity of DeOxyHb.<sup>24,25,41,47,48</sup> The tissue DeOxyHb concentration increases due to increased extraction of oxygen from the reduced amount of OxyHb. However, the rise in total tissue DeOxyHb is countered to some degree by vasoconstriction, decreased intravascular hemoglobin, and resultant reduction in total hemoglobin within the tissues. Tissue hemoglobin



saturation ( $S_{T-O_2}$ ) is calculated as the ratio of OxyHb/total hemoglobin thus falls during hemorrhage.<sup>24,25,41,47,48</sup>

CcO redox state changes parallel to those of OxyHb and  $S_{T-O_2}$  during hemorrhage. As tissue oxygen supply decreases, with hypotension, decreased cardiac output, and anemia, ongoing tissue metabolic oxygen demands continue. This results in a supply:demand imbalance and a decrease of CcO in the oxidized state and an increase of CcO in the reduced state, with an overall reduction in CcO redox state during hemorrhage.

During CN poisoning, OxyHb increases and DeOxyHb decreases due to the inability of tissues to extract oxygen from the blood as a result of inhibition of cytochrome-based electron transport. This results in increased tissue capillary and venous hemoglobin oxygen content as reflected by an increase in OxyHb and decrease in DeOxyHb concentrations with increased tissue hemoglobin oxygen saturation.<sup>28–31</sup>

However, CN poisoning presents a relatively unique situation in which, despite the increase in tissue OxyHb and  $S_{T-O_2}$ , the CcO oxidation state decreases. This is a direct result of CN binding and subsequent reduction of the active metal centers in CcO.<sup>14,32,34–36</sup> Thus, during CN poisoning, the direction of change of cytochrome oxidation is opposite to that of hemoglobin oxygenation (unlike that seen during hemorrhage).

During decreases in inspired oxygen concentration, tissue hemoglobin oxygenation decreases. Although arterial hemoglobin is fully oxygen saturated on room air (21%  $O_2$ ), the partial pressure and oxygen content of dissolved blood oxygen are higher when animals are on 100% inspired oxygen than when on room air. This leads to increases in capillary and venous oxygen content when maintained on 100% inspired oxygen. Thus, as inspired oxygen concentration is decreased from 100% to 21% for brief periods of time, the tissue OxyHb temporarily falls. Although the tissue OxyHb concentration rises during CN poisoning, the CcO redox state moves in the opposite direction, i.e., becomes more reduced. Brief reductions in inspired oxygen from 100% to 21% decrease the tissue OxyHb concentration, and reduce the CcO redox state due to reduction in the quantity and partial pressure of oxygen in the delivered blood. Thus, hemoglobin oxygen saturation and CcO redox states move in the same direction during brief reductions in inspired oxygen, but in opposite directions during continuous CN infusion.

Together, these findings clearly demonstrate uncoupling of OxyHb and DeOxyHb signals from CcO redox signals in peripheral muscle. These findings are further supported by blood gas measurements demonstrating development of acute metabolic acidosis during CN poisoning. Previous *in vitro* studies have shown that anaerobic metabolism commences when approximately 60% of CcO activity has been inhibited by CN.<sup>5</sup> CcO reduction as measured by DOS is an optical measure of redox state, while *in vitro* studies measure CcO enzymatic activity; comparison of the two measures may not be expected to correlate directly.

There are number of limitations of the current study. First, the oxyhemoglobin, deoxyhemoglobin, total hemoglobin, oxidized, and reduced CcO values we report have no gold standard for validation. Thus, while they are consistent with physiologic invasive measurements, the precision and accuracy of the DOS numbers have not been validated. Second, we have clearly demonstrated “uncoupling” of the optical hemoglobin signals from the CcO signals in peripheral muscle. However, whether

some underlying degree of partial “cross talk” may affect the CcO redox state remains uncertain. Also third, DOS interrogates a region 2 to 4 mm below the sensor using the source detector separation distances used in these studies. Thus, the ability to extrapolate to deeper events is limited. Additional limitations of this study include the potential contribution of wavelength based spatial variation in tissue signal interrogation in the NIR wavelength range. This could result in deeper tissue region contributions from the higher wavelength regions. The contribution of other cytochrome components cannot be excluded as well. We have attempted to minimize these factors by focusing the analytic spectra above the 650 nm range in this study.

In summary, using unique animal model systems and intervention combinations, these studies demonstrate independence of *in vivo* DOS CcO redox state measurements from underlying hemoglobin signals in peripheral muscle, where potential interference from myoglobin could occur, unlike in the brain region. Important future directions would include confirmation and correlation of DOS measures of CcO redox state by assessment of anaerobic metabolism based on gas exchange measurements during CN poisoning, and deeper level invasive DOS-based probes for internal organ level assessment. Ultimately, clinical studies will be needed to determine if CcO redox signal measurements can optimize management of tissue CcO redox states in critical disease processes.

### Acknowledgments

The authors acknowledge support by the CounterACT Program, Office of the Director, National Institutes of Health (OD) and the National Institute of Environmental Health Sciences (NIEHS), 1U54NS063718, 1U54NS079201, U01-NS058030, U54-NS079201, AMRMC W81XWH-12-2-0114, Air Force FA9550-04-1-0101, FA9550-08-1-0384, and FA9550-10-1-0438; the NIH/NBIB Laser Microbeam and Medical Program P41-EB015890.

### References

1. A. H. Hall and B. H. Rumack, “Clinical toxicology of cyanide,” *Ann. Emerg. Med.* **15**(9), 1067–1074 (1986).
2. S. I. Baskin and T. G. Brewer, “Medical aspects of chemical and biological warfare. Cyanide poisoning,” Chapter 10 in *Textbook of Military Medicine. Part I, Warfare, Weaponry, and the Casualty*, F. R. Sidell et al., Eds., pp. 272–286, Office of the Surgeon General at TMM Publications, Washington, D.C. (1997).
3. T. F. Cummings, “The treatment of cyanide poisoning,” *Occup. Med. (Lond.)* **54**(2), 82–85 (2004).
4. G. E. Isom and J. L. Borowitz, “Modification of cyanide toxicodynamics: mechanistic based antidote development,” *Toxicol. Lett.* **82–83**, 795–799 (1995).
5. H. B. Leavesley et al., “Interaction of cyanide and nitric oxide with cytochrome c oxidase: implications for acute cyanide toxicity,” *Toxicol. Sci.* **101**(1), 101–111 (2008).
6. K. Alexander and S. I. Baskin, “The inhibition of cytochrome oxidase by diaminomaleonitrile,” *Biochim. Biophys. Acta* **912**(1), 41–47 (1987).
7. G. T. Babcock and M. Wikstrom, “Oxygen activation and the conservation of energy in cell respiration,” *Nature* **356**(6367), 301–309 (1992).
8. J. O. Egekeze and F. W. Oehme, “Cyanides and their toxicity: a literature review,” *Tijdschr. Diergeneesk.* **105**(8, Suppl. 2), 104–114 (1980).
9. F. F. Jobsis et al., “Reflectance spectrophotometry of cytochrome aa3 *in vivo*,” *J. Appl. Physiol.* **43**(5), 858–872 (1977).
10. N. B. Hampson and C. A. Piantadosi, “Near infrared monitoring of human skeletal muscle oxygenation during forearm ischemia,” *J. Appl. Physiol.* **64**(6), 2449–2457 (1988).

11. A. D. Edwards et al., "Quantification of concentration changes in neonatal human cerebral oxidized cytochrome oxidase," *J. Appl. Physiol.* **71**(5), 1907–1913 (1991).
12. Y. Hoshi et al., "Redox behavior of cytochrome oxidase in the rat brain measured by near-infrared spectroscopy," *J. Appl. Physiol.* **83**(6), 1842–1848 (1997).
13. T. Noriyuki et al., "Near-infrared spectroscopic method for assessing the tissue oxygenation state of living lung," *Am. J. Respir. Crit. Care Med.* **156**(5), 1656–1661 (1997).
14. C. E. Cooper et al., "Use of mitochondrial inhibitors to demonstrate that cytochrome oxidase near-infrared spectroscopy can measure mitochondrial dysfunction noninvasively in the brain," *J. Cereb. Blood Flow Metab.* **19**(1), 27–38 (1999).
15. C. E. Cooper, D. T. Delpy, and E. M. Nemoto, "The relationship of oxygen delivery to absolute haemoglobin oxygenation and mitochondrial cytochrome oxidase redox state in the adult brain: a near-infrared spectroscopy study," *Biochem. J.* **332**(Pt 3), 627–632 (1998).
16. C. E. Cooper and R. Springett, "Measurement of cytochrome oxidase and mitochondrial energetics by near-infrared spectroscopy," *Philos. Trans. R. Soc., B* **352**(1354), 669–676 (1997).
17. V. Quaresima et al., "Oxidation and reduction of cytochrome oxidase in the neonatal brain observed by in vivo near-infrared spectroscopy," *Biochim. Biophys. Acta* **1366**(3), 291–300 (1998).
18. A. Bainbridge et al., "Brain mitochondrial oxidative metabolism during and after cerebral hypoxia-ischemia studied by simultaneous phosphorus magnetic-resonance and broadband near-infrared spectroscopy," *Neuroimage* (in press) (2013).
19. Y. Sakata et al., "Measurement of the oxidation state of mitochondrial cytochrome c from the neocortex of the mammalian brain," *Biomed. Opt. Express* **3**(8), 1933–1946 (2012).
20. B. Chance and W. Bank, "Genetic disease of mitochondrial function evaluated by NMR and NIR spectroscopy of skeletal tissue," *Biochim. Biophys. Acta* **1271**(1), 7–14 (1995).
21. F. Bevilacqua et al., "Broadband absorption spectroscopy in turbid media by combined frequency-domain and steady-state methods," *Appl. Opt.* **39**(34), 6498–6507 (2000).
22. D. J. Jakubowski, *Development of Broadband Quantitative Tissue Optical Spectroscopy for the Non-Invasive Characterization of Breast Disease*, Beckman Laser Institute, University of California Irvine, Irvine (2002).
23. B. J. Tromberg et al., "Non-invasive in vivo characterization of breast tumors using photon migration spectroscopy," *Neoplasia* **2**(1–2), 26–40 (2000).
24. J. Lee et al., "Hemoglobin measurement patterns during noninvasive diffuse optical spectroscopy monitoring of hypovolemic shock and fluid replacement," *J. Biomed. Opt.* **12**(2), 024001 (2007).
25. J. Lee et al., "Broadband diffuse optical spectroscopy assessment of hemorrhage- and hemoglobin-based blood substitute resuscitation," *J. Biomed. Opt.* **14**(4), 044027 (2009).
26. J. Lee et al., "Noninvasive in vivo monitoring of methemoglobin formation and reduction with broadband diffuse optical spectroscopy," *J. Appl. Physiol.* **100**(2), 615–622 (2006).
27. J. Lee et al., "Non-invasive in vivo diffuse optical spectroscopy monitoring of cyanide poisoning in a rabbit model," *Physiol. Meas.* **28**(9), 1057–1066 (2007).
28. J. Lee et al., "Noninvasive in vivo monitoring of cyanide toxicity and treatment using diffuse optical spectroscopy in a rabbit model," *Mil. Med.* **174**(6), 615–621 (2009).
29. M. Brenner et al., "Sulfanegen sodium treatment in a rabbit model of sub-lethal cyanide toxicity," *Toxicol. Appl. Pharmacol.* **248**(3), 269–276 (2010).
30. M. Brenner et al., "Intramuscular cobinamide sulfite in a rabbit model of sublethal cyanide toxicity," *Ann. Emerg. Med.* **55**(4), 352–363 (2010).
31. M. Brenner et al., "Comparison of cobinamide to hydroxocobalamin in reversing cyanide physiologic effects in rabbits using diffuse optical spectroscopy monitoring," *J. Biomed. Opt.* **15**(1), 017001 (2010).
32. C. A. Piantadosi, A. L. Sylvia, and F. F. Jobsis, "Cyanide-induced cytochrome a, a3 oxidation-reduction responses in rat brain in vivo," *J. Clin. Invest.* **72**(4), 1224–1233 (1983).
33. A. Villringer and B. Chance, "Non-invasive optical spectroscopy and imaging of human brain function," *Trends Neurosci.* **20**(10), 435–442 (1997).
34. H. Beinert et al., "Studies on the origin of the near-infrared (800–900 nm) absorption of cytochrome c oxidase," *Biochim. Biophys. Acta* **591**(2), 458–470 (1980).
35. C. A. Piantadosi and A. L. Sylvia, "Cerebral cytochrome a,a3 inhibition by cyanide in bloodless rats," *Toxicology* **33**(1), 67–79 (1984).
36. M. Tamura, "Protective effects of a PGI2 analogue OP-2507 on hemorrhagic shock in rats—with an evaluation of the metabolic recovery using near-infrared optical monitoring," *Jpn. Circ. J.* **56**(4), 366–375 (1992).
37. C. E. Cooper et al., "Measurement of cytochrome oxidase redox state by near infrared spectroscopy," *Adv. Exp. Med. Biol.* **413**, 63–73 (1997).
38. F. Bevilacqua et al., "Broadband absorption spectroscopy in turbid media by combined frequency-domain and steady-state methods," *Appl. Opt.* **39**(34), 6498–6507 (2000).
39. T. H. Pham et al., "Broad bandwidth frequency domain instrument for quantitative tissue optical spectroscopy," *Rev. Sci. Instrum.* **71**(6), 2500–2513 (2000).
40. S. Merritt et al., "Comparison of water and lipid content measurements using diffuse optical spectroscopy and MRI in emulsion phantoms," *Technol. Cancer Res. Treat.* **2**(6), 563–569 (2003).
41. J. Lee et al., "Broadband diffuse optical spectroscopy measurement of hemoglobin concentration during hypovolemia in rabbits," *Physiol. Meas.* **27**(8), 757–767 (2006).
42. W. G. Zijlstra, A. Buursma, and O. W. Assendelft, *Visible and Near-infrared Absorption Spectra of Human and Animal Hemoglobin*, VSP BV, AH Zeist, Netherlands (2000).
43. L. H. Kou, D. Labrie, and P. Chylek, "Refractive indices of water and ice in the 0.65 to 2.5 mm spectral range," *Appl. Opt.* **32**(19), 3531–3540 (1993).
44. C. Eker, *Optical Characterization of Tissue for Medical Diagnostics*, Lund University, Lund, Sweden (1999).
45. S. Wray et al., "Characterization of the near infrared absorption spectra of cytochrome aa3 and haemoglobin for the non-invasive monitoring of cerebral oxygenation," *Biochim. Biophys. Acta* **933**(1), 184–192 (1988).
46. S. Fantini et al., "Non-invasive optical monitoring of the newborn piglet brain using continuous-wave and frequency-domain spectroscopy," *Phys. Med. Biol.* **44**(6), 1543–1563 (1999).
47. J. Lee et al., "Tissue hemoglobin monitoring of progressive central hypovolemia in humans using broadband diffuse optical spectroscopy," *J. Biomed. Opt.* **13**(6), 064027 (2008).
48. T. H. Pham et al., "Noninvasive monitoring of hemodynamic stress using quantitative near-infrared frequency-domain photon migration spectroscopy," *J. Biomed. Opt.* **7**(1), 34–44 (2002).

Biographies of the authors are not available.

# Faraday instability-based micro droplet ejection for inhalation drug delivery

C.S. Tsai<sup>1,3</sup>, R.W. Mao<sup>1</sup>, S.K. Lin<sup>1</sup>, Y. Zhu<sup>1</sup> & S.C. Tsai<sup>2</sup>

**We report here the technology and the underlying science of a new device for inhalation (pulmonary) drug delivery which is capable of fulfilling needs unmet by current commercial devices. The core of the new device is a centimeter-size clog-free silicon-based ultrasonic nozzle with multiple Fourier horns in resonance at megahertz (MHz) frequency. The dramatic resonance effect among the multiple horns and high growth rate of the MHz Faraday waves excited on a medicinal liquid layer together facilitate ejection of monodisperse droplets of desirable size range (2–5  $\mu\text{m}$ ) at low electrical drive power (<1.0 W). The small nozzle requiring low drive power has enabled realization of a pocket-size ( $8.6 \times 5.6 \times 1.5 \text{ cm}^3$ ) ultrasonic nebulizer. A variety of common pulmonary drugs have been nebulized using the pocket-size unit with desirable aerosol sizes and output rate. These results clearly provide proof-of-principle for the new device and confirm its potential for commercialization.**

## INNOVATION

Drugs designed to treat pulmonary diseases or for systemic absorption through the massive surface area of the lung require optimum particle sizes (1 to 6  $\mu\text{m}$ ). Current advanced commercial devices such as Omron, Pari eFlow, and Philips I-neb produce droplets or aerosols by a vibrating mesh. All these devices suffer from broad particle size (poly-disperse) distributions and lack of size control capability, and also are plagued by clogging of mesh orifices used.

Here we report a new delivery device that has demonstrated capability for control of particle size within the optimum size range at low drive power and freedom from clogging. The new device employs a novel silicon-based ultrasonic nozzle with multiple Fourier horns in resonance designed to operate based on the newly discovered phenomena of Faraday waves at the frequency range of 1 to 2.5 MHz. The superior performance and batch fabrication economy of the centimeter-size nozzles have paved the way for commercialization of the new device.

## INTRODUCTION

Inhalation is an increasingly important route for non-invasive drug delivery for both systemic and local applications<sup>1–5</sup>. Control of particle (aerosols or droplets in air) size and output plays a critical role in the efficient and effective delivery of often expensive medications to the lung. Drugs designed to treat pulmonary diseases or for systemic absorption through the alveolar capillary bed require optimum particle sizes (1 to 6  $\mu\text{m}$ ) for effective delivery. Based on deposition of aerosol particles in human respiratory tract following a slow inhalation (250 mL/s air rate) and a 5-second hold<sup>4,5</sup>, particles 1 to 4  $\mu\text{m}$  (in aerodynamic diameter) deposit primarily in the alveolar region while particles 3 to 6  $\mu\text{m}$  deposit in the airways. Particles larger than 6  $\mu\text{m}$  deposit primarily in the mouth

and throat. It is to be noted that respirable particles in the 1–4  $\mu\text{m}$  range are optimal for alveolar deposition, but contain less drug than particles in the 2–5  $\mu\text{m}$  range by 4 to 8 times per particle. With proper control of particle size, drugs ranging from small molecules such as pentamidine to large molecules such as insulin could be effectively delivered as aerosols via inhalation for systemic absorption or local treatment in airways and lung parenchyma<sup>6–10</sup>.

Current commercial devices such as Misty-Neb, AeroEclipse, Omron, Pari eFlow, and Philips I-neb produce droplets or aerosols by compressed air, a vibrating piezoelectric plate together with a metallic mesh, or a vibrating mesh. As the examples (plots a and b) show in Fig. 1A, all these devices suffer from broad particle size (poly-disperse) distributions (with high geometrical standard deviation (GSD) >1.5), making it difficult to deliver sufficient drug of desirable sizes to targeted sites precisely and rapidly. Furthermore, the eFlow and I-neb which utilize vibrating mesh technology<sup>11</sup> and are considered the most advanced commercial devices suffer from clogging of the mesh orifices used<sup>12</sup>. Thus, delivery devices with control capability in particle size and less susceptibility to clogging are clearly needed for rapid administration at sufficient quantities of often expensive drugs such as agents to treat pulmonary hypertension and toxic inhalation agent antidotes<sup>13,14</sup>. Here we report a new delivery device that utilizes a silicon-based megahertz (MHz) multiple-Fourier horn ultrasonic nozzle (MFHUN) and temporal instability of Faraday waves<sup>15,16</sup> to fulfill the unmet needs. As plots c, d, and e of Fig. 1A show, by varying the drive frequency of the MFHUN from 1.0 to 2.5 MHz the new device was capable of controlling the particle sizes within the optimum size range (1 to 6  $\mu\text{m}$ ) with a much narrower size distribution.

The much narrower droplet size distribution achieved by the new device (MFHUN), compared to advanced commercial devices, is also

<sup>1</sup>Department of Electrical Engineering and Computer Science, <sup>2</sup>Department of Chemical Engineering and Materials Science, University of California, Irvine, CA 92697, USA. <sup>3</sup>Institute of Optoelectronics and Photonics, National Taiwan University, Taipei, Taiwan. Correspondence should be addressed to C.S.T. (csttsai@uci.edu).



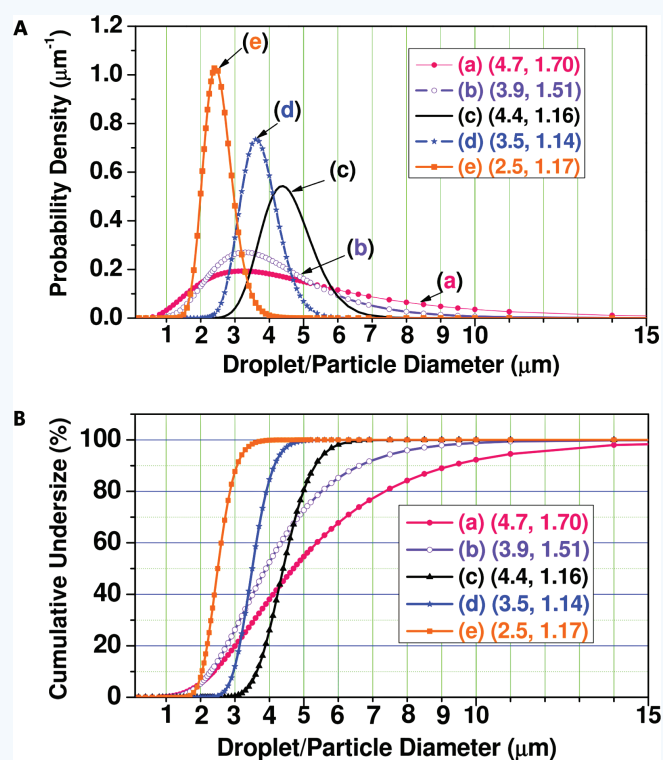


**Figure 1** Comparison of (A) particle diameters and size distributions (MMAD/MMD  $\mu\text{m}$ , GSD), and (B) Cumulative undersize percentage between the commercial devices and the new device: (a) Philips I-neb<sup>9</sup>, (b) Pari eFlow<sup>8</sup>, (c) 1.0 MHz, (d) 1.5 MHz, and (e) 2.5 MHz. Note that MMAD for (a)–(b) and MMD for (c)–(e) stand for mass median aerodynamic diameter and mass median diameter, respectively; MMD and geometrical standard deviation (GSD) for the new device were obtained using Malvern/Spraytec particle sizer (Model #STP 5311); and GSD of 1.0 represents a single particle size and the closer the GSD to 1.0 the higher the monodispersity.

illustrated by its steeper cumulative undersize percentage curves as shown in Fig. 1B. Notably, plots c to e show that 100% or nearly 100% of droplets are smaller than 6  $\mu\text{m}$  in diameter for the new device while plots a and b show only 66% and 85%, respectively, for the advanced commercial nebulizers. The much narrower droplet size distribution will have significant economic impact on lung deposition of drugs, especially of expensive drugs. For example, as shown in Fig. 1A the MMD of plot c obtained using the new device at 1 MHz drive frequency is similar to the MMAD of plot a obtained using one of the most advanced commercial nebulizers — the I-neb Adaptive Aerosol Delivery (AAD) System that delivers aerosol only during inspiration (i.e. breath actuation). However, as shown in plot c of Fig. 1B the narrower size distribution with a smaller GSD obtained by the former (1.16 versus 1.70) leads to a much greater respirable (inhaled) fraction (nearly 100% versus 66% with particle diameter < 6  $\mu\text{m}$ ) than by the latter. Therefore, the inhaled dose delivered to the lung using the new device together with breath actuation should be much higher than the  $60 \pm 5\%$  achievable using the I-neb AAD System<sup>9</sup>. Note that as presented in the final section of “Methods and Results”, the capability of breath actuation with the pocket-size MFHUN unit has been demonstrated (Fig. 6C).

Faraday waves, also known as standing capillary waves, were first observed as wavy surface of a water layer resting on a solid surface subjected to perpendicular mechanical vibration, as depicted in Fig. 2A, at a very low drive (or forcing) frequency (5 Hz) by Faraday in 1831<sup>17</sup>. They

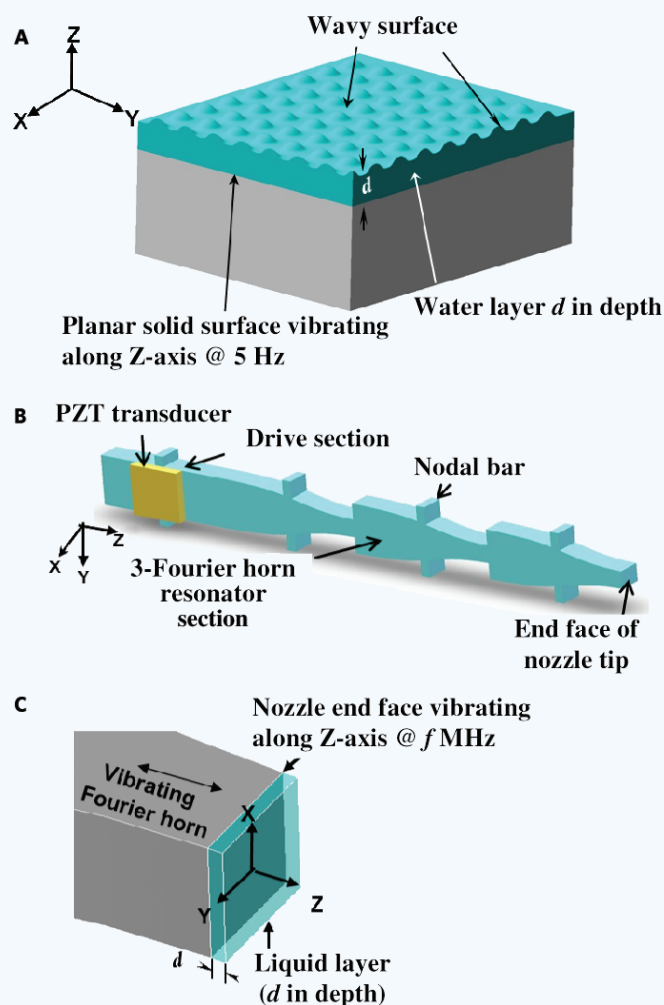


**Figure 2** (A) Classical planar geometry for Faraday waves formation at low drive frequency (5 Hz). (B) 3-D architecture of the MHz multiple-Fourier horn ultrasonic nozzle. (C) Geometry of nozzle end face and planar liquid layer d in depth.

were subsequently analyzed by Rayleigh in 1883<sup>18</sup> and many others<sup>19</sup>. Faraday instability, the underlying physical mechanism for Faraday wave formation and amplification, was studied<sup>20–24</sup> extensively based on the above classical planar geometry during the 1990s, and continued<sup>25–29</sup> in the 2000s, but mostly at very low drive frequency ranging from tens to thousands hertz (Hz). At such low drive frequencies, various standing-wave patterns were observed<sup>25,30</sup> when the mechanical vibration amplitude on the solid surface reached the onset threshold for Faraday wave formation. However, no droplet ejection (atomization) was described in the theoretical treatments of these earlier low-drive frequency studies. In the few reports on atomization at low drive frequencies, droplet ejection was found to take place only when the mechanical vibration amplitude on the solid surface was *much higher* than the onset threshold for Faraday wave formation. In stark contrast, our recent discovery as reported here using a novel device, silicon-based MHz MFHUN (see Fig. 2B), shows that at the much higher drive frequencies of MHz the onset threshold for Faraday wave formation is *much lower* and the mechanical vibration amplitude required for subsequent droplet ejection is *only slightly higher* than the onset threshold for Faraday wave formation<sup>15</sup>. These findings have also been verified by the rigorous theoretical treatment<sup>31,32</sup> summarized in the first section of “Methods and Results”.

## METHODS AND RESULTS

### Linear theory on MHz Faraday wave instability for monodisperse micro droplet ejection

#### Classical model of planar liquid layer geometry

**Figure 2C** depicts the classical model geometry for theoretical study of Faraday instability reported here — a planar liquid layer of depth ( $d$ ) resting on a planar solid surface mimicked by the end face of the silicon-based multiple-Fourier horn ultrasonic nozzle (MFHUN) that vibrates longitudinally along the nozzle axis (Z-axis) at the resonance frequency ( $f$ ). The longitudinal vibration of the nozzle end face exerts a periodic pressure on the planar liquid layer. Faraday waves are formed on the free surface of the liquid layer when the peak vibration displacement of the nozzle end face ( $h$ ) reaches the critical value or onset threshold ( $h_{cr}$ ). The following theoretical treatment for the Faraday wave with amplitude  $\xi(x, t)$  that represents the time-dependence displacement of the free liquid surface is based on mass-conservation and linearized Navier-Stokes equations for incompressible Newtonian liquids, such as water, with density  $\rho$ , surface tension  $\sigma$ , and kinematic viscosity  $\nu$ <sup>33</sup>.

Due to symmetry in the XY-plane, it is convenient to separate the coordinates into the perpendicular Z-direction and the XY-plane with  $x$  designating ( $x, y$ ). First, we utilize Navier-Stokes equations and incompressibility condition, and apply the boundary conditions on the nozzle end face and the free liquid surface of the planar liquid layer geometry of **Fig. 2C**. The Navier-Stokes equations together with the Laplace's equation are solved by means of the Fourier transform in the horizontal coordinates ( $x$ ) to result in the following equation for the temporal evolution of the amplitude  $\xi_k$  of the  $k^{\text{th}}$  mode Faraday waves for low-viscosity liquid such as water:

$$\partial_t^2 \xi_k(t) + 4\nu k^2 \partial_t \xi_k(t) + (\omega_k^2 + kg_e(t))\xi_k(t) = 0 \quad (1)$$

where the wave number ( $k$ ) equals  $2\pi/\lambda$  and  $\omega_k^2 \equiv \sigma k^3/\rho$ , and  $g_e(t)$  is the external acceleration, equal to  $h(2\pi f)^2 \cos(2\pi f t)$ . Finally, Eq. (1) is solved using the established technique for the  $k^{\text{th}}$  mode Faraday waves amplitude  $\xi_k(x, t)$  in the most unstable region (the first tongue-like region) of the stability chart<sup>15,34</sup> and the result is given by Eq. (2).

#### Temporal instability of MHz Faraday waves and onset threshold for droplet ejection

The amplitude of the fastest growing  $k^{\text{th}}$  mode Faraday wave  $\xi_k(t)$  in the most unstable region is obtained as follows:

$$\begin{aligned} \xi_k(t) &= \xi_0 e^{(\pi k f h - \beta)t} \sin(\pi f t - \pi/4), \\ \text{i.e. } \xi_k(t) &= \xi_0 e^{\pi k f (h - h_{cr})t} \sin(\pi f t - \pi/4), \end{aligned} \quad (2)$$

where  $\xi_0$  designates the initial wave amplitude and  $h_{cr} \equiv \beta/(\pi k f)$ , in which  $\beta \equiv 2\nu k^2$ . Equation (2) clearly shows that the single-mode Faraday waves excited carry a frequency equal to one-half of the drive frequency ( $f$ ), namely,  $\omega_k = \pi f$ , and the corresponding wavelength ( $\lambda$ ) and onset threshold ( $h_{cr}$ ) are given as follows:

$$\lambda = 2\pi/k = 2\pi(\rho \omega_k^2/\sigma)^{-1/3} = 2\pi(\rho \pi^2 f^2/\sigma)^{-1/3} = (8\pi\sigma/\rho)^{1/3} f^{-2/3}. \quad (3)$$

$$h_{cr} \equiv \beta/(\pi k f) = 2\nu k/(\pi f) = 2\nu \rho^{1/3} (\pi\sigma)^{-1/3} f^{-1/3}. \quad (4)$$

Note that the onset threshold ( $h_{cr}$ ) is at the minimum at the critical wave number ( $k_{cr}$ ), i.e., the  $k^{\text{th}}$  mode Faraday wave in the aforementioned stability chart and also referred to in Eq. (1).

#### Dynamics of droplet ejection

Equation (4) shows the specific dependence of the onset threshold on the drive frequency ( $f$ ) and the liquid properties ( $\rho$ ,  $\sigma$ , and  $\nu$ ). It should be emphasized that  $h_{cr}$  decreases with the drive frequency in accordance

with  $f^{-1/3}$ , and the wave amplitude  $\xi_k(t)$  grows exponentially in time when  $h > h_{cr}$ . It is to be emphasized also that  $h_{cr}$  not only falls within the most unstable region but also decreases from 0.33 to 0.29 and to 0.24  $\mu\text{m}$ , respectively, for water as an example, as  $f$  increases from 1.0 to 1.5 and to 2.5 MHz. The corresponding Faraday wavelengths are 12.2, 9.2, and 6.6  $\mu\text{m}$ , and the respective wave numbers  $k_{cr}$ 's are 5204, 6820, and 9498  $\text{cm}^{-1}$ . While  $h_{cr}$  decreases with the drive frequency in accordance with  $f^{-1/3}$ , the exponent  $\pi k f (h - h_{cr})t$  in the exponential factor of  $\xi_k(t)$  increases with the drive frequency in accordance with  $f^{4/3}$ . Thus, the temporal growth of the single-mode Faraday wave amplitude at MHz drive frequency is very rapid once the nozzle end face excitation displacement  $h$  exceeds the onset threshold  $h_{cr}$ . Take the Faraday waves at the 1.5 MHz drive frequency with the corresponding wavelength of 9.2  $\mu\text{m}$  in water as an example, when  $h$  exceeds the predicted  $h_{cr}$  of 0.29  $\mu\text{m}$  by as little as 0.01  $\mu\text{m}$  the growth rate factor  $e^{\pi k f (h - h_{cr})t}$  of the Faraday wave amplitude in Eq. (2) in a time increment of 0.5 ms is  $\sim 10^7$  times that with  $(h - h_{cr})$  as large as 100  $\mu\text{m}$  at 200 Hz<sup>25</sup> drive frequency at the same time increment (0.5 ms). The amplitude growth rate factor at 1.5 MHz with  $(h - h_{cr})$  of 0.01  $\mu\text{m}$  in a time increment of 0.5 ms is still greater (by 8%) than that at 200 Hz with  $(h - h_{cr})$  of 100  $\mu\text{m}$  in a much longer time increment of 143 ms. When the wave amplitude grows and becomes too great to maintain wave stability, the Faraday waves break up, and thus droplets are ejected from the free surface of the liquid layer<sup>31,32</sup>.

In summary, the scientific discovery on dynamics of droplet ejection at MHz drive frequency as described above together with the greatly magnified displacement on the end face of the MHz MFHUN enables generation of micrometer-size monodisperse droplets at low electrical drive power. This discovery also serves to explain the observations on atomization experiments at low drive frequencies described in "Introduction".

#### Size of ejected droplets

Now the ejected spherical droplets, with radius  $a$  and at the lowest oscillation mode frequency<sup>33,35</sup>, are dispersed in air and free from external acceleration ( $g_e$ ). Thus, by setting the frequency of the droplet's lowest oscillation mode equal to the nozzle drive frequency, the following theoretical droplet diameter ( $D_p \equiv 2a$ ) in terms of Faraday wavelength ( $\lambda$ ) is obtained:

$$D_p = 2(2/\pi^2)^{1/3} (\sigma/\rho)^{1/3} f^{-2/3} = 0.40\lambda. \quad (5)$$

Namely, the predicted droplet diameter equals four tenths of the Faraday wavelength involved. Note that this is the first theoretical formula for the droplet diameter in capillary wave-based ultrasonic droplet ejection. Clearly, for a given liquid to be nebulized, the desired size of the droplets can be controlled by the drive frequency ( $f$ ) of the MFHUN in accordance with  $f^{-2/3}$ ; the smaller the droplet size the higher the nozzle drive frequency.

### Design, simulation, fabrication, characterization of MFHUNs, and droplet ejection studies

#### Design and simulation of MFHUNs

The innovation of the new ultrasonic delivery device lies in the multiple Fourier horns in cascade that vibrate in a single longitudinal mode along the nozzle axis at the same and single resonance frequency. As shown in **Fig. 2B**, the nozzle consists of a drive section and a resonator section. A lead zirconate titanate (PZT) piezoelectric transducer is bonded on the drive section to excite mechanical vibrations along the nozzle axis (Z-axis). The resonator section is made of multiple (3 in the example) Fourier horns in cascade<sup>36</sup>. The nozzle is designed to vibrate at the resonance frequency of the multiple Fourier horns. The resultant vibration amplitude (displacement) on the nozzle end face (tip of the distal horn) is greatly magnified with a gain of  $M^n$  for a  $n$ -Fourier horn nozzle with a magnification of  $M$  for each Fourier horn<sup>15</sup>. In order to produce

monodisperse droplets of desirable size range (2–5  $\mu\text{m}$ ) at high output rate and low electrical drive power (sub Watt), the optimum magnifications of 1.8 and 1.3 for the first three and the last horn of the 4-Fourier horn nozzles, respectively, were used in the design of optimized MFHUN.

Each Fourier horn is of half acoustic wavelength design<sup>36,37</sup>. The longitudinal axis of the nozzle (Z-axis) is in the direction of the primary flat, namely,  $\langle 110 \rangle$  of the silicon wafer with the highest longitudinal acoustic velocity. A three-dimensional (3-D) finite element method (FEM) simulation is carried out using the commercial ANSYS (ANSYS Inc., Canonsburg, PA) Program first for vibration mode shape analysis and then for electrical impedance analysis<sup>36</sup>. The mode shape analysis determines the nozzle resonance frequency of pure longitudinal vibration mode; the electrical impedance analysis determines the longitudinal vibration displacement on the nozzle end face and the impedance at the nozzle resonance frequency. The resultant longitudinal vibration displacement on the nozzle end face is then used to determine the threshold voltage required to produce the onset threshold ( $h_{cr}$ ) given by Eq. (4) in the first section of “Methods and Results”. The threshold voltage thus obtained together with the resistive part of the impedance is then used to calculate the electrical drive power required for droplet ejection. Both the simulation results with the acoustical and electrical losses taken into account and the experimental results show that the optimum number of Fourier horns ( $n$ ) in terms of electrical drive power requirement is 3 or 4. Due to the design of the nozzle, the onset threshold ( $h_{cr}$ ) cannot be reached at any frequency outside the bandwidth ( $<10$  kHz) of the designed resonance frequency; this design feature is critical to producing monodisperse droplets of the desired diameter at very low drive power.

The greatly enhanced peak vibration displacement ( $h$ ) on the nozzle end face of the MFHUN facilitates the onset threshold required for initiation of temporal instability of the Faraday waves on the surface of the liquid layer and subsequent ejection of droplets at low electrical drive.

#### Fabrication and characterization of MFHUNs

The silicon-based MFHUNs of various designs in terms of the drive (resonance) frequency and the number of Fourier horns in cascade were fabricated using micro-electromechanical system (MEMS) technology.<sup>38</sup> The drive and resonator sections of the MFHUN were formed in a single-fabrication step using an inductive coupled plasma (ICP) process<sup>39</sup>. Note that a large number of nozzles with identical or different design specifications can be fabricated in one batch in a common silicon wafer. **Figure 3A** shows the layout of a large number of nozzles. After bonding of the PZT plate and the connecting wires, the resulting centimeter-size nozzles with optimum designs are shown in **Fig. 3B**.

The only essential characterization of the fabricated nozzle prior to droplet ejection experiments is to measure the impedance curve using Agilent impedance analyzer model 4294 A<sup>15</sup> from which the drive frequency and the electrical drive power are determined.

#### Droplet ejection studies

All the droplet ejection (atomization) experiments presented below were conducted using either the established bench-scale setup<sup>16</sup> or the pocket-size nebulizer. Major components of the setup are: (i) a PZT transducer drive system to provide a MHz electrical drive to the ultrasonic nozzle, (ii) a Syringe Pump (kd Scientific Model #101) to provide a controlled flow rate of liquid, (iii) a CCD camera to take pictures or movies of the droplets produced, and (iv) a Malvern/Spraytec System (Model #STP 5311) for analysis of the size distribution of the droplets.

**Figures 4A** and **4B** show photos of a stream of droplets produced from a water layer resting on the nozzle end face of the MHz nozzles using a high-resolution high-speed camera system with back-lighting and a normal speed camera system with front lighting, respectively. The droplet rates for the outputs of 40 and 350  $\mu\text{L}/\text{min}$  (set by external feeding of water) are  $1.4 \times 10^7$  and  $4.0 \times 10^8$  droplets/sec, respectively. These high droplet output rates are in contrast to the continuous ink-jet printing

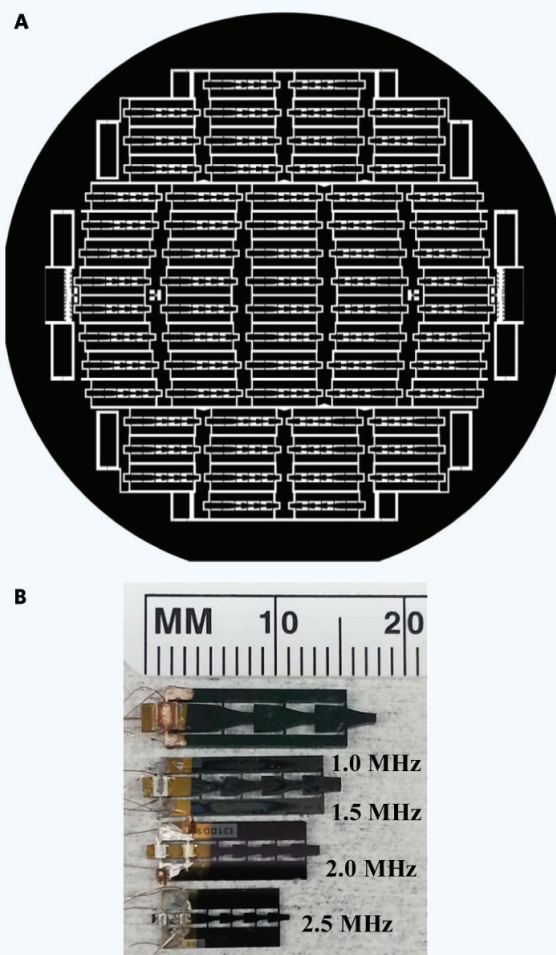


**Figure 3** (A) Layout of nozzles with various designs in a common silicon wafer. (B) 1.0, 1.5, 2.0, and 2.5 MHz nozzles fabricated and studied.

( $<10^6$  droplets/sec (10  $\mu\text{m}$  in diameter)<sup>40</sup>) resulting from the Rayleigh-Plateau instability. The short depth of focus provided by the high-resolution high-speed camera system enabled visualization of individual droplets ejected from the liquid layer and the thin-lighted curve caused by the Faraday waves excited on its surface as shown in **Fig. 4A**. The wavy liquid surface caused by the Faraday waves acts like optical gratings to scatter the incident light. Note that light scattered by Faraday waves excited on the liquid surface also resulted in intense brightness over the entire spherical surface of a water ball<sup>32</sup> (see **Fig. 2a** of Ref. 32) ejecting micro droplets.

The Malvern/Spraytec System is used to analyze the size distribution of droplets of **Fig. 4B**. The system is a non-invasive particle sizing instrument based on laser light diffraction. Since the laser beam had a cross sectional area (1 cm in diameter) much larger than the stream (spray) of droplets ( $\sim 0.07 \times 0.1$  cm<sup>2</sup>) produced by the nozzles, the data reported in this study were obtained from the entire cross-section of the droplet stream. The data include mass median diameter (MMD) and geometrical standard deviation (GSD). GSD and geometric mean of a data set with a log-normal distribution are, respectively, equivalent to the standard deviation and arithmetic mean of a data set with normal distribution. GSD is simply calculated by the geometric mean of quotients (ratios)  $D_{84}/D_{50}$  and  $D_{50}/D_{16}$ , where  $D_{84}$ ,  $D_{50}$ , and  $D_{16}$  are, respectively, the droplet diameters at 84.1%, 50.0%, and 15.9% of the cumulative undersize percent of the droplet size distribution as shown in **Fig. 1B**. Note that the GSD was determined by least square fit ( $R^2 = 0.9987$ ) of



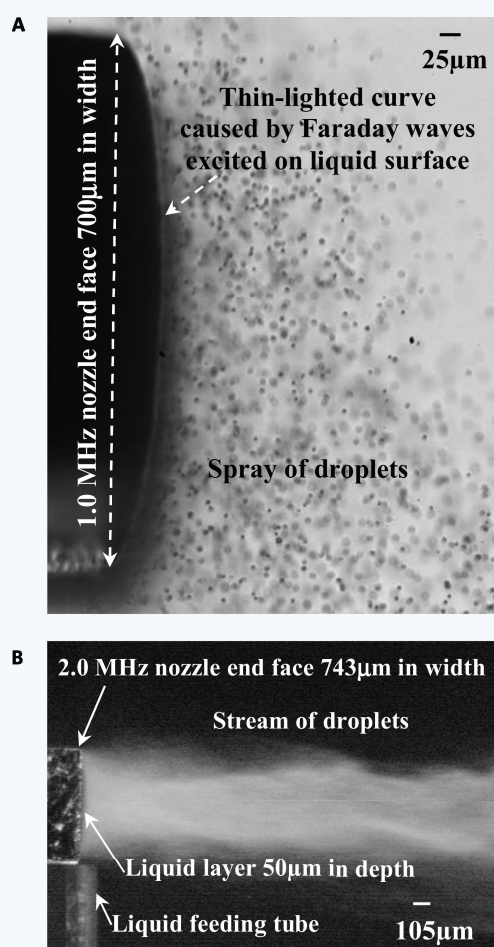


**Figure 4** Stream of droplets ejected from the liquid layer resting on the end face of the nozzle tip: (A) High-speed photograph ( $10^4$  frame/sec, Vision Research Model Phantom<sup>®</sup> v7.2) with short depth of focus for droplets stream at output rate of 40  $\mu\text{L}/\text{min}$  with 1.0 MHz nozzle. (B) CCD image (20 frame/sec) of droplets stream at output rate of 350  $\mu\text{L}/\text{min}$  and electrical drive power of 0.27 W with optimized 2.0 MHz nozzle. Note that the scale bars in (A) and (B) are 25  $\mu\text{m}$  and 105  $\mu\text{m}$ , respectively.

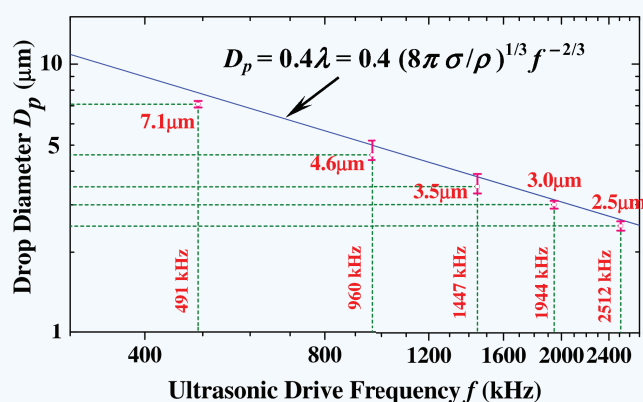


**Figure 5** Comparison between the measured droplet diameters and the theoretical predictions.

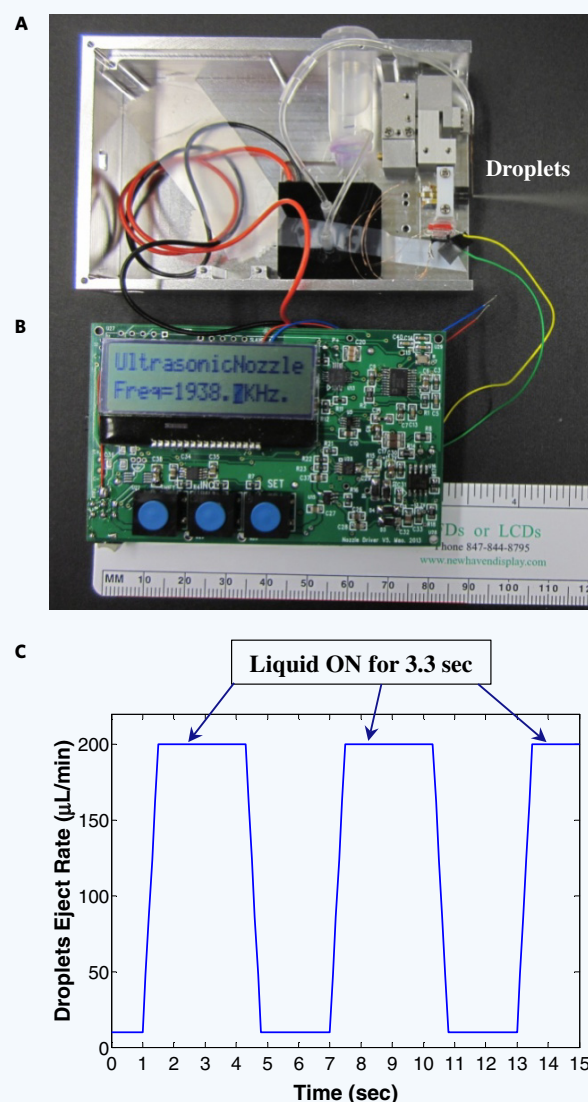


**Figure 6** Pocket-size silicon-based ultrasonic nebulizer (8.8 cm  $\times$  5.9 cm  $\times$  1.9 cm): (A) Layout of ultrasonic nozzle and other mechanical components. (B) Layout of battery-powered electronic driver. (C) Externally actuated ON/OFF nebulization using a Harvard ventilator at 55% inspiratory, 750 mL tidal volume, and 10 breaths/min.

the cumulative undersize percentage curve obtained using the Malvern/Spraytec System. **Figure 5** shows clearly the excellent agreement between the measured droplet diameter and the theoretical prediction of Eq. (5) given in the first section of "Methods and Results".

#### Pocket-size ultrasonic nebulizer and nebulization of common drugs

As presented in the last subsection, the droplet ejection (atomization) experiments using the bench-scale unit with a single nozzle have demonstrated the capability of the silicon-based MHz MFHUNs for production of monodisperse droplets of desirable size (2 to 5  $\mu\text{m}$ ) and moderate output (up to 0.2 mL/min) at low electrical drive power (sub Watt). At the typical output rate of 0.15 mL/min with 3.5  $\mu\text{m}$ -diameter droplets, which equals  $1.1 \times 10^8$  droplets/sec, the required electrical drive power of 0.27 W corresponds to 2.4 nano joule per droplet generated. The centimeter-size nozzles with the low electrical power requirement

**Table 1** Summary of drugs nebulized.

Medicine	Medicine concentration	Ultrasonic drive freq. (MHz)	Nebulizer unit	Droplet diameter ( $\mu\text{m}$ )	Output rate ( $\mu\text{L}/\text{min}$ )	Disease
Albuterol	25 mg/ml	1.0	Bench-scale	4.5	150	Asthma
Humulin, U100	100 units/ml	1.0	Bench-scale	4.5	100	Diabetes
Cobinamide <sup>a</sup>	100 mM	1.5	Pocket-size	3.9	130	Cyanide poisoning
Interferon- $\gamma^b$	100 $\mu\text{g}/0.5$ ml	2.0	Pocket-size	2.9	100	Pulmonary fibrosis
Budesonide suspension	0.5 mg/2.0 ml	2.0	Pocket-size	3.1	350	Asthma

<sup>a,b</sup>Provided by Prof. G. Boss at UC San Diego and Prof. G.C. Saldone, State Univ. of New York, Stony Brook, respectively.

enabled most recent realization of the first pocket-size ultrasonic nebulizer ( $8.6 \times 5.6 \times 1.5$  cm<sup>3</sup>). The nebulizer contains a single ultrasonic nozzle with optimum design as shown in **Fig. 3B**, IC electronic driver, battery, micro pump, drug reservoir, and liquid feed tube. The layout of the nozzle with other mechanical components and that of the battery-powered electronic driver are shown in **Figs. 6A** and **6B**, respectively. A range of drug substances for asthma, diabetes, pulmonary fibrosis, cyanide poisoning, etc. such as albuterol (salbutamol), Humulin U-100,<sup>41</sup> cobinamide, interferon- $\gamma$ <sup>10</sup> and budesonide suspension<sup>42</sup> have been nebulized using the pocket-size nebulizer with desirable aerosol size and output rate as summarized in **Table 1**. Some drugs such as albuterol and cobinamide, and aqueous glycerol were successfully nebulized using the bench scale and/or the pocket-size units at varying concentrations with the corresponding range of viscosity up to as high as 4.5 cP and flow rate up to 350  $\mu\text{L}/\text{min}$ . Furthermore, the pocket-size nebulizer has demonstrated its capability for nebulization of commercial budesonide suspension medicine that none of the current commercial ultrasonic nebulizers is capable of. It is to be noted that the demonstrated moderate output rate of 100–350  $\mu\text{L}/\text{min}$  by the pocket-size unit would provide a higher effective dosage over the current commercial nebulizers in light of the higher aerosol monodispersity produced by the former. Clearly, a higher output rate can be accomplished readily by using an array of identical ultrasonic nozzles.

Breath actuation is an important operational requirement of a nebulizer in order to save the often expensive medicine. As shown in **Fig. 6C**, nebulization of medicine is turned ON/OFF by turning ON/OFF the feeding of the medicine using a piezoelectric micro pump to the nozzle end face in synchronization with the inspiratory cycle of a ventilator (Harvard piston pump). Specifically, a probe senses the UP/DOWN movement of the piston pump and sends a corresponding electrical signal to turn ON/OFF the liquid feed. A pressure sensor, with or without an ON/OFF disk/membrane valve, can be used for breathing without a ventilator. Thus, the pocket-size ultrasonic nebulizer is also capable of fulfilling this operational requirement.

## DISCUSSION

Recently, we mimicked the Faraday's classical planar geometry of **Fig. 2A** using the end face of silicon-based MHz multiple-Fourier horn ultrasonic nozzle (MFHUN) and carried out theoretical and experimental studies at much higher drive frequencies (0.5 to 2.5 MHz)<sup>15,16,31,32</sup>. The resonance effect among the multiple Fourier horns designed for the single vibration mode at the single resonance frequency greatly magnifies the vibration displacement of the nozzle end face (by a factor of  $2^n$ , where  $n$  designates the number of Fourier horns each with a magnification of 2) and, hence, readily facilitates formation and subsequent high-rate growth of Faraday waves on the free surface of the liquid layer. The single-mode Faraday wave excitation and amplification leads to generation of monodisperse droplets of desirable size range ( $\sim 2$  to  $5$   $\mu\text{m}$ ) at very low electrical drive power ( $<1$  W)<sup>16</sup>. Such Faraday instability-based droplet ejection device is in stark contrast to all other existing ultrasonic devices employing a vibrating piezoelectric plate that simultaneously involve various droplet ejection mechanisms such as cavitation, impinging, and jetting in addition to capillary wave mechanism<sup>25,43,44</sup>. These ejection mechanisms require

much higher electrical drive power (by 1 to 2 orders of magnitude) and produce broad droplet size distribution. The low electrical drive power requirement for the new ultrasonic device reported here not only facilitates miniaturization, but also minimizes temperature rises that might damage the medications to be aerosolized.

The precise control of particle size and much narrower particle size distribution achieved by the new device will improve targeting of treatment within the respiratory tract and improve delivery efficiency, resulting in better efficacy, fewer side effects, shorter treatment times, and lower medication costs compared with existing nebulizers. Additionally, high output rate of medicinal aerosol is desirable because it will shorten treatment times. The new device with a single nozzle alone has demonstrated an output rate up to 350  $\mu\text{L}/\text{min}$ . Clearly, the output rate can be readily increased by using an array of identical nozzles. Furthermore, nozzle arrays with individual nozzles designed at different resonance frequency will provide the unique capability for production and mixing of aerosols of different sizes and/or medicines. Such nozzle arrays will provide a unique platform for basic research. The MEMS-based fabrication technology involved will enable construction of nozzle arrays of various designs.

The micron-size monodisperse droplets produced by the miniaturized low-power ultrasonic nozzles reported here may find a wide range of attractive applications other than inhalation drug delivery. Some examples of such applications include synthesis of nano particles via spray pyrolysis, sample injection in chemical analysis (e.g. mass spectroscopy), high-quality thin-film coating,<sup>45</sup> 3-D photoresist coating of micro- and nano-structures in fabrication of nano-electronic and -photonic devices, fuel injection in combustion, delivery of lipid-based micro-encapsulated biological entities or gene,<sup>46,47</sup> pharmaceutical preparation such as double emulsion,<sup>48,49</sup> rapid heat removal in laser surgery, and rapid administration of cosmetics.

The work reported here is the result of an interesting cross-fertilization between science and technology. Our original quest for an atomizer capable of producing micron-size monodisperse droplets led to the invention of the silicon-based MHz multiple Fourier horns in cascade. Subsequently, the study of the underlying mechanisms for droplet ejection led all the way back to Faraday's 1831 classical experiments involving a water layer at the very low drive frequency of 5 Hz and to many subsequent theoretical and experimental studies, but still at low drive frequencies up to ten's kHz. Our theoretical study on Faraday waves at the much higher drive frequency of MHz uncovered the frequency-sensitive dynamics of droplet ejection. The multiple-Fourier horn ultrasonic nozzle provides experimental verification of the theoretical predictions and facilitates the production of monodisperse droplets of desirable micron-size range at low drive power. Despite more than 180 years of continued interest and studies on Faraday waves it was only through our invention and realization of MHz ultrasonic nozzles with multiple Fourier horns in resonance that the technical potential of Faraday waves at MHz frequency range was discovered and led to a technology with immediate and important medical applications.

## ACKNOWLEDGEMENTS

This work was supported by grants from the US National Institute of Health (NIH) NIBIB Grant #5R21EB006366, Counter ACT Program U54-NS063718 and AMRMC W81XWH-12-2-0114, Academia Sinica

and National Science Council, Taiwan, and Shih-Lin Electric USA. C.S. Tsai and S.C. Tsai would like to acknowledge collaborations with Matthew Brenner of UC Irvine, Gerry R. Boss of UC San Diego, and Steven Patterson of Univ. of Minnesota; encouragement and helpful discussions with Gerald C. Smaldone, State Univ. of New York, Stony Brook, NY, Howard A. Stone of Princeton University, Kwang-Jin Kim at Univ. of Southern California, Theodore Y.T. Wu of California Institute of Technology, Robert Langar of MIT, and Enrique Cerda at Univ. de Santiago de Chile. The authors also acknowledge Professor Peter Taborek and graduate student Serah Gutman of the Department of Physics and Astronomy at UC Irvine for loaning of their high-speed high-resolution camera and assistance in obtaining Fig. 4A, and the Institute of Physics, Academia Sinica, Taiwan for fabrication of some of the nozzle platforms.

## AUTHOR CONTRIBUTIONS

C.S. Tsai initiated, acquired funding and supervised the study, and wrote the paper. S.C. Tsai and C.S. Tsai co-invented the device and developed the theory. S.C. Tsai also analyzed the experimental data and compared them with the theoretical predictions. R.W. Mao made major contributions to fabrication and construction of the device, and obtained the experimental data using the pocket-size nebulizer with the assistances of S.K. Lin and Y. Zhu. S.K. Lin also obtained the experimental data using the bench-scale setup.

## COMPETING INTERESTS STATEMENT

The authors declare that they have no competing interests.

## REFERENCES

- Langer, R. Perspectives: Drug delivery — Drugs on target. *Science* **293**, 58–59 (2001).
- Heyder, J. Deposition of inhaled particles in the human respiratory tract and consequences for regional targeting in respiratory drug delivery. *Proc. Am. Thorac. Soc.* **1**, 315–320 (2004).
- Usmani, O.S., Biddiscombe, M.F. & Barnes, P.J. Regional lung deposition and bronchodilator response as a function of beta2-agonist particle size. *Am. J. Respir. Crit. Care Med.* **172**, 1497–1504 (2005).
- Scheuch, G., Kohlhaeufel, M.J., Brand, P. & Siekmeier, R. Clinical perspectives on pulmonary systemic and macromolecular delivery. *Adv. Drug Deliv. Rev.* **58**, 996–1008 (2006).
- Patton, J.S. & Byron, P.R. Inhaling medicines: Delivering drugs to the body through the lungs. *Nat. Rev. Drug Discovery* **6**, 67–74 (2007).
- Sangwan, S., Condos, R. & Smaldone, G.C. Lung deposition and respirable mass during wet nebulization. *J. Aerosol. Med.* **16**, 379–386 (2003).
- Watts, A.B., McConville, J.T. & Williams, R.O. 3<sup>rd</sup>. Current therapies and technological advances in aqueous aerosol drug delivery. *Drug Dev. Ind. Pharm.* **34**, 913–922 (2008).
- Coates, A.L., Green, M., Leung, K., Chan, J., Ribeiro, N., Louca, E., Ratjen, F., Charon, M., Tservistas, M. & Keller, M. Rapid pulmonary delivery of inhaled tobramycin for *Pseudomonas* infection in cystic fibrosis: A pilot project. *Pediatr. Pulmonol.* **43**, 753–759 (2008).
- Geller, D.E. & Kesser, K.C. The I-neb adaptive aerosol delivery system enhances delivery of alpha 1-antitrypsin with controlled inhalation. *J. Aerosol Med. Pulm. D* **23**, S55–S59 (2010).
- Diaz, K.T., Skaria, S., Harris, K., Solomita, M., Lau, S., Bauer, K., Smaldone, G.C. & Condos, R. Delivery and safety of inhaled interferon-gamma in idiopathic pulmonary fibrosis. *J. Aerosol Med. Pulm. Drug Deliv.* **25**, 79–87 (2012).
- Lass, J.S., Sant, A. & Knoch, M. New advances in aerosolised drug delivery: Vibrating membrane nebuliser technology. *Expert Opin. Drug Deliv.* **3**, 693–702 (2006).
- Rottier, B.L., van Erp, C.J.P., Sluyter, T.S., Heijerman, H.G.M., Frijlink, H.W. & de Boer, A.H. Changes in performance of the Pari eFlow (R) Rapid and Pari LC Plus (TM) during 6 months use by CF patients. *J. Aerosol Med. Pulm. D* **22**, 263–269 (2009).
- Kreuter, K.A., Lee, J., Mahon, S.B., Kim, J.G., Mukai, D., Mohammad, O., Blackledge, W., Boss, G.R., Tromberg, B.J. & Brenner, M. Rapid reversal of cyanide toxicity using a novel agent, cobinamide, assessed noninvasively using diffuse optical spectroscopy. *Chest* **134**, 124001 (2008).
- Tsai, C.S., Mao, R.W., Zhu, Y., Chien, E., Tsai, S.C., Brenner, M., Mahon, S., Mukai, D., Lee, J., Yoon, D., Berney, T., Boss, G.R. & Patterson, S. Hand-held high-throughput ultrasonic monodisperse aerosol inhalers for detoxification of massive cyanide poisoning. 2012 *IEEE Int. Ultrason. Symp. Proc.*, pp. 1632–1634 (2012).
- Tsai, S.C., Cheng, C.H., Wang, N., Song, Y.L., Lee, C.T. & Tsai, C.S. Silicon-based Megahertz ultrasonic nozzles for production of monodisperse micrometer-sized droplets. *IEEE Trans. Ultrason. Ferroelect. Freq. Control* **56**, 1968–1979 (2009).
- Tsai, C.S., Mao, R.W., Lin, S.K., Wang, N. & Tsai, S.C. Miniaturized multiple Fourier-horn ultrasonic droplet generators for biomedical applications. *Lab Chip* **10**, 2733–2740 (2010).
- Faraday, M. On a peculiar class of acoustical figures and on certain forms assumed by groups of particles upon vibrating elastic surfaces. *Philos. Trans. Roy. Soc. Lond.* **A52**, 299–340 (1831).
- Rayleigh, B. On the crispation of fluid resting upon a vibrating support. *Philos. Mag.* **16**, 50–58 (1883).
- Benjamin, T.B. & Ursell, F. The stability of the plane free surface of a liquid in vertical periodic motion. *Proc. Roy. Soc. Lond. A* **225**, 505–515 (1954).
- Miles, J. & Henderson, D. Parametrically forced surface-waves. *Annu. Rev. Fluid Mech.* **22**, 143–165 (1990).
- Guthart, G.S. & Wu, T.Y.T. Observation of a standing kink cross wave parametrically excited. *Proc. Roy. Soc. Lond. A* **434**, 435–440 (1991).
- Kumar, K. Linear theory of Faraday instability in viscous liquids. *Proc. Roy. Soc. Lond. A* **452**, 1113–1126 (1996).
- Cerda, E.A. & Tirapegui, E.L. Faraday's instability for viscous liquids. *Phys. Rev. Lett.* **78**, 859–862 (1997).
- Sindayibura, D. & Bolle, L. Ultrasonic atomization of liquids: Stability analysis of the viscous liquid film free surface. *Atomization Sprays* **8**, 217–233 (1998).
- Yule, A.J. & Al-Suleimani, Y. On droplet formation from capillary waves on a vibrating surface. *Proc. Roy. Soc. Lond. A* **456**, 1069–1085 (2000).
- Ubal, S., Giavedoni, M.D. & Saita, F.A. A numerical analysis of the influence of the liquid depth on two dimensional Faraday waves. *Phys. Fluids* **15**, 3099–3113 (2003).
- James, A.J., Vukasinovic, B., Smith, M.K. & Glezer, A. Vibration-induced drop atomization and bursting. *J. Fluid Mech.* **476**, 1–28 (2003).
- Wright, P.H. & Saylor, J.R. Patterning of particulate films using Faraday waves. *Rev. Sci. Instrum.* **74**, 4063–4070 (2003).
- Shats, M., Xia, H. & Punzmann, H. Parametrically excited water surface ripples as ensembles of oscillons. *Phys. Rev. Lett.* **108**, 034502–034501 to 034505 (2012).
- Edwards, W.S. & Fauve, S. Parametrically excited quasi-crystalline surface-waves. *Phys. Rev. E* **47**, R788–R791 (1993).
- Tsai, S.C. & Tsai, C.S. Linear theory of temporal instability of Megahertz Faraday waves for monodisperse microdroplet ejection. *IEEE Trans. Ultrason. Ferroelect. Freq. Control* **60**, 1746–1754 (2013).
- Tsai, S.C., Lin, S.K., Mao, R.W. & Tsai, C.S. Ejection of uniform micrometer-sized droplets from Faraday waves on a millimeter-sized water drop. *Phys. Rev. Lett.* **108**, 154501–154501 to 154505 (2012).
- Landau, L.D. & Lifshitz, E.M. *Fluid Mechanics*. Elsevier Publishing, London/New York (1987).
- Cerda, E.A. & Tirapegui, E.L. Faraday's instability in viscous fluid. *J. Fluid Mech.* **368**, 195–228 (1998).
- Rayleigh, B. On the capillary phenomenon of jets. *Proc. Roy. Soc. Lond.* **29**, 71–97 (1879).
- Tsai, S.C., Song, Y.L., Tseng, T.K., Chou, Y.F., Chen, W.J. & Tsai, C.S. High-frequency silicon-based ultrasonic nozzles using multiple Fourier horns. *IEEE Trans. Ultrason. Ferroelect. Freq. Control* **51**, 277–285 (2004).
- Tsai, S.C., Song, Y.L., Tsai, C.S., Chou, Y.F. & Cheng, C.H. Ultrasonic atomization using MHz silicon-based multiple-Fourier horn nozzles. *Appl. Phys. Lett.* **88**, 014102–014101 (2006).
- Lal, A. & White, R.M. Micromachined silicon ultrasonic atomizer. *IEEE Int. Ultrason. Symp. Proc.*, pp. 339–342 (1996).
- McAuley, S.A., Ashraf, H., Atabo, L., Chambers, A., Hall, S., Hopkins, J. & Nicholls, G. Silicon micromachining using a high-density plasma source. *J. Phys. D* **34**, 2769–2774 (2001).
- Hertz, C.H. & Samuelsson, B.A. Ink jet printing of high quality color images. *J. Imag. Tech.* **15**, 141–148 (1989).
- Tsai, S.C., Mao, R.W., Mukai, D., Lin, S.K., Wilson, A.F., Wang, N., Brenner, M., George, S.C., Yang, J.Y., Wang, P. & Tsai, C.S. Pulmonary drug delivery using miniaturized silicon-based MHz ultrasonic nozzles. Presented at the *Int. Conf. Accelerating Biopharm. Dev.*, Colorado, 9–12 March (2009).
- Nikander, K., Turpeinen, M. & Wollmer, P. The conventional ultrasonic nebulizer proved inefficient in nebulizing a suspension. *J. Aerosol Med.* **12**, 47–53 (1999).
- Maehara, N., Ueha, S. & Mori, E. Influence of the vibrating system of a multipin-hole plate ultrasonic nebulizer on its performance. *Rev. Sci. Instrum.* **57**, 2870–2876 (1986).
- Tsai, S.C., Luu, P., Childs, P., Teshome, A. & Tsai, C.S. The role of capillary waves in two-fluid atomization. *Phys. Fluids* **9**, 2909–2918 (1997).
- Bird, J.C., Mandre, S. & Stone, H.A. Coalescence of spreading droplets on a wettable substrate. *Phys. Rev. Lett.* **97**, 064501–064501 to 064504 (2006).
- Dang, J.M. & Leong, K.W. Natural polymers for gene delivery and tissue engineering. *Adv. Drug Delivery Rev.* **58**, 487–499 (2006).
- Zarnitsyn, V.G., Meacham, J.M., Varady, M.J., Hao, C.H., Degertekin, F.L. & Fedorov, A.G. Electrosonic ejector microarray for drug and gene delivery. *Biomed. Microdevices* **10**, 299–308 (2008).
- Garstecki, P., Fuerstman, M.J., Stone, H.A. & Whitesides, G.M. Formation of droplets and bubbles in a microfluidic T-junction — Scaling and mechanism of break-up. *Lab Chip* **6**, 437–446 (2006).
- Tan, Y.C., Hettiarachchi, K., Siu, M., Pan, Y.R. & Lee, A.P. Controlled microfluidic encapsulation of cells, proteins, and microbeads in lipid vesicles. *J. Am. Chem. Soc.* **128**, 5656–5658 (2006).



# Intravenous Cobinamide Versus Hydroxocobalamin for Acute Treatment of Severe Cyanide Poisoning in a Swine (*Sus scrofa*) Model

Lt Col Vikhyat S. Bebarta, MC, USAF\*; David A. Tanen, MD; Susan Boudreau, RN, BSN; Maria Castaneda, MS; Lee A. Zarzabal, MS; Toni Vargas, PA-C; Gerry R. Boss, MD

\*Corresponding Author. E-mail: [vikbebarta@yahoo.com](mailto:vikbebarta@yahoo.com).

**Study objective:** Hydroxocobalamin is a Food and Drug Administration–approved antidote for cyanide poisoning. Cobinamide is a potential antidote that contains 2 cyanide-binding sites. To our knowledge, no study has directly compared hydroxocobalamin with cobinamide in a severe, cyanide-toxic large-animal model. Our objective is to compare the time to return of spontaneous breathing in swine with acute cyanide-induced apnea treated with intravenous hydroxocobalamin, intravenous cobinamide, or saline solution (control).

**Methods:** Thirty-three swine (45 to 55 kg) were intubated, anesthetized, and instrumented (continuous mean arterial pressure and cardiac output monitoring). Anesthesia was adjusted to allow spontaneous breathing with  $\text{FiO}_2$  of 21% during the experiment. Cyanide was continuously infused intravenously until apnea occurred and lasted for 1 minute (time zero). Animals were then randomly assigned to receive intravenous hydroxocobalamin (65 mg/kg), cobinamide (12.5 mg/kg), or saline solution and monitored for 60 minutes. A sample size of 11 animals per group was selected according to obtaining a power of 80%, an  $\alpha$  of .05, and an SD of 0.17 in mean time to detect a 20% difference in time to spontaneous breathing. We assessed differences in time to death among groups, using Kaplan-Meier estimation methods, and compared serum lactate, blood pH, cardiac output, mean arterial pressure, respiratory rate, and minute ventilation time curves with repeated-measures ANOVA.

**Results:** Baseline weights and vital signs were similar among groups. The time to apnea and cyanide dose required to achieve apnea were similar. At time zero, mean cyanide blood and lactate concentrations and reduction in mean arterial pressure from baseline were similar. In the saline solution group, 2 of 11 animals survived compared with 10 of 11 in the hydroxocobalamin and cobinamide groups ( $P < .001$  between the 2 treated groups and the saline solution group). Time to return of spontaneous breathing after antidote was similar between hydroxocobalamin and cobinamide (1 minute 48 seconds versus 1 minute 49 seconds, respectively). Blood cyanide concentrations became undetectable at the end of the study in both antidote-treated groups, and no statistically significant differences were detected between the 2 groups for mean arterial pressure, cardiac output, respiratory rate, lactate, or pH.

**Conclusion:** Both hydroxocobalamin and cobinamide rescued severely cyanide-poisoned swine from apnea in the absence of assisted ventilation. The dose of cobinamide was one fifth that of hydroxocobalamin. [Ann Emerg Med. 2014;64:612-619.]

Please see page 613 for the Editor's Capsule Summary of this article.

A **feedback** survey is available with each research article published on the Web at [www.annemergmed.com](http://www.annemergmed.com).

A **podcast** for this article is available at [www.annemergmed.com](http://www.annemergmed.com).

0196-0644/\$-see front matter

Copyright © 2014 by the American College of Emergency Physicians.

<http://dx.doi.org/10.1016/j.annemergmed.2014.02.009>

## INTRODUCTION

### Background

Hydroxocobalamin is a Food and Drug Administration–approved antidote for treating acute cyanide poisoning.<sup>1-3</sup> However, because of its poor water solubility, it must be administered in a relatively large volume intravenously. In the out-of-hospital setting of cyanide gas release, such as an industrial accident, terrorist attack, or commercial or residential fire,

intravenous access can be difficult and particularly problematic for providers wearing hazardous material protective gear; thus, nonintravenous antidotes are urgently needed.<sup>4-7</sup> To address this concern, federal agencies, including the National Institutes of Health and the US Army Medical Research Institute of Chemical Defense, are actively seeking nonintravenous, potent new antidotes.<sup>4,5</sup> Cobinamide is a water-soluble analog of hydroxocobalamin that has a much higher affinity for cyanide than

### Editor's Capsule Summary

#### *What is already known on this topic*

An intramuscularly administered antidote for cyanide toxicity would be desirable, particularly in the out-of-hospital environment. Cobinamide is a candidate agent, but its intravenous efficacy has not yet been evaluated.

#### *What question this study addressed*

This nonblinded 33-pig study compared the efficacy of intravenous cobinamide, hydroxocobalamin, and placebo in a nonlethal model of cyanide poisoning.

#### *What this study adds to our knowledge*

The primary endpoint, time to return of spontaneous respirations after intravenous administration, was similar for both antidotes.

#### *How this is relevant to clinical practice*

If findings are confirmed with intramuscular administration, cobinamide may be an effective out-of-hospital antidote, especially during mass toxicologic events.

hydroxocobalamin and binds 2 moles of cyanide per mole compared with 1 mole of cyanide for each mole of hydroxocobalamin. Cobinamide has been shown to be 3 to 10 times more potent than hydroxocobalamin<sup>6</sup> in both mice and rabbit models of acute cyanide intoxication,<sup>7,8</sup> but to our knowledge it has not been studied in a critically ill large-animal model of cyanide poisoning.

### Goals of This Investigation

Our goal was to compare the time to return of spontaneous breathing among 3 groups of swine after 1 minute of acute cyanide-induced apnea. This model has been previously validated as a model of acute cyanide toxicity and was developed to have a potential low survival rate in untreated animals.<sup>3,9,10</sup> If intravenous cobinamide is as efficacious as hydroxocobalamin in treating cyanide poisoning in a large animal, future studies could test the efficacy of cobinamide administered by the intramuscular route.

## MATERIALS AND METHODS

### Study Design and Setting

This investigation was a nonblinded randomized study approved by the Wilford Hall Clinical Research Division Institutional Animal Care and Use Committee. All animal experiments complied with the regulations and guidelines of the Animal Welfare Act, the National Institutes of Health Guide for

the Care and Use of Laboratory Animals, and the American Association for Accreditation of Laboratory Animal Care. Animals were housed and the study was conducted in the Animal Care Facility.

Before the beginning of the experiment, animals were randomly assigned, using a commonly used online medical research randomization plan generator (<http://www.randomization.com>) to one of the 3 following intravenous interventions: (1) hydroxocobalamin, the positive control and standard antidote; (2) cobinamide, the experimental antidote; or (3) saline solution, the negative control.

Yorkshire swine (*Sus scrofa*) (n=33, weighing 45 to 55 kg, female) were premedicated with intramuscular ketamine 10 mg/kg. General anesthesia was induced with isoflurane by nose cone. After intubation, the animals were mechanically ventilated with a volume-limited, time-cycled ventilator (Fabius GS anesthesia machine; Dräger-Siemens, New York, NY) and maintained with inhaled isoflurane (1% to 3%) and oxygen (FiO<sub>2</sub> of 0.4 to 0.45). The tidal volume was initially 8 to 10 mL/kg and respiratory rate was 12 breaths/min. The minute ventilation was adjusted to maintain an end tidal CO<sub>2</sub> of 38 to 42 mm Hg as measured by inline capnography. Lead II of the surface ECG was monitored continuously. Animal body temperature was maintained at 37.5°C (99.5°F) to 39.0°C (102.2°F). Baseline biochemical variables (arterial blood gas, hemoglobin, and electrolytes) were measured.

### Interventions

Invasive hemodynamic variables were measured with an 8-French Swan-Ganz CCOMbo pulmonary artery catheter (model 746HF8) and the Edwards Vigilance II monitor (Edwards Lifesciences, Irvine, CA). Measurements included continuous cardiac output, systemic vascular resistance, mixed venous oxygen saturation, central venous pressure, pulmonary artery pressure, and core temperature. Catheter ports were flushed with saline solution, and the catheter was placed by cutdown in the right external jugular. Aortic pressure was measured continuously through the femoral artery. An 8.5-French introducer (Arrow, Reading, PA) was placed in the carotid artery for laboratory sampling and another was placed in the femoral vein for medication administration. The animals received a warmed saline solution intravenous bolus (15 mL/kg) during procedure setup. Heparin (100 U/kg) was administered intravenously after catheters were inserted. The Fabius GS anesthesia data collection software embedded in the ventilator's computer was used for data acquisition at 1-minute intervals.

Baseline biochemical measurements included oxygen saturation, PaCO<sub>2</sub>, PaO<sub>2</sub>, and pH (ABL 800 Flex blood gas analyzer; Radiometer America, Westlake, OH), hemoglobin (OSM3 Hemoximeter; Radiometer, Westlake, OH), and electrolytes (Piccolo Chemistry Analyzer; Abaxis, Union City, CA). Ventilation and oxygenation variables were also collected and included tidal volume, respiratory rate, minute volume, and pulse oximetry.

After a 10-minute acclimation period, isoflurane was reduced to 1% to 1.5%, the FIO<sub>2</sub> was adjusted to room air (0.21), and



the mechanical ventilator was turned off. Thus, the animals breathed spontaneously for the remainder of the experiment. Once the animals had sustained spontaneous respirations for 5 minutes, a 0.4% potassium cyanide solution (potassium cyanide; Sigma Aldrich, St. Louis, MO; normal saline solution) was infused continuously until apnea occurred and was confirmed by capnography for 20 seconds. At this point (apnea), the cyanide infusion was stopped. After capnographic confirmation of 1 additional minute of apnea (time zero), animals were administered the antidote or saline solution intravenously as a bolus injection. The cobinamide was infused in less than 1 minute and the hydroxocobalamin was infused during 2 to 3 minutes to administer the larger volume. Animals received equal volumes of 90 mL during the infusion with 10 mL of saline solution given before and 10 mL infused after each drug administration. Cobinamide was infused in 4 to 8 mL, with an additional 80 to 85 mL of saline solution, hydroxocobalamin was infused in 90 mL, and 90 mL of saline solution was infused for control animals. The dose and infusion duration for cobinamide and hydroxocobalamin were based on previous published animal models and preliminary experiments in our laboratory.<sup>3,8-10</sup>

The animals were monitored for 60 minutes after treatment. Death was defined as a mean arterial pressure less than 20 mm Hg for 5 minutes. Animals that died were observed for an additional 20 minutes or until the end of the experiment to evaluate for a possible delayed therapeutic effect. At death or the conclusion of the study, animals were euthanized with intravenous sodium pentobarbital 100 mg/kg.

Whole blood cyanide levels, which includes cyanide bound to cobinamide and hydroxocobalamin, were measured spectrophotometrically at a referral laboratory (Michigan State University, Diagnostic Center for Population and Animal Health, Lansing, MI).<sup>11</sup> This method generates hydrogen cyanide gas, converts it to a cyanogen chloride, and measures a barbituric acid complex.<sup>10,11</sup>

## Methods of Measurement and Outcome Measures

The primary outcome was time to return of spontaneous breathing after 1 minute of cyanide-induced apnea. This outcome was defined before the study and based on our previous research.<sup>3,7,12</sup> We also assessed survival and compared cardiac output, pulse rate, mixed venous oxygenation, pH, lactate, base excess, serum bicarbonate, cyanide concentrations, and inflammatory markers. Vital signs and hemodynamic measurements were recorded at 1-minute intervals and analyzed at 5-minute intervals. Blood sampling was obtained at baseline, 5 minutes after start of the cyanide infusion, at the onset of apnea, after 1 minute of apnea, and at 10, 20, 30, 40, 50, and 60 minutes after treatment.

## Primary Data Analysis

The average time (in minutes and seconds) to return of spontaneous breathing after the antidote/saline solution was

administered was compared among the 3 groups with the Kruskal-Wallis test. This nonparametric statistical analysis was used because the data were not normally distributed (Shapiro-Wilk test). Additional analysis was performed among the 3 groups to assess the differences in time to death, using Kaplan-Meier estimation methods of the survival distribution and log-rank testing to compare survival among the groups.

Secondary outcome variables (cardiac output, pulse rate, systemic vascular resistance, respiratory rate, mean arterial blood pressure, mixed venous oxygenation, and inflammatory markers) were modeled with repeated-measures ANOVA, with adjustment for treatment, time, and the interaction of treatment by time with an autoregressive covariance structure assumed. Because only 2 of the control animals survived after 30 minutes, the control group was not included in secondary outcome variable analysis so that those data would not unduly influence the results of the comparison between the 2 antidote intervention groups. Post hoc analysis was performed on all variables that showed a significant treatment-by-time interaction, for which treatment contrasts were measured at each posttreatment point with a Bonferroni adjustment for multiple testing applied. Values for arterial blood pH, lactate, cyanide, bicarbonate, base excess, and potassium concentrations were compared among groups with repeated-measures ANOVA for times zero to 60 minutes.

All statistical testing was 2 sided, with a significant level of  $\alpha=.05$ , and was completed with SAS (version 9.3; SAS Institute, Inc., Cary, NC). All graphic presentations were made with R version 2.15.1. Sample size calculations were based on our previous animal experiments of acute cyanide toxicity. A sample size of 11 animals per group was determined to be sufficient according to obtaining a power of 80%, an  $\alpha=.05$ , and an SD of 0.17 (based on previous experiments) in mean time to detect a 20% difference in time to spontaneous breathing. Sample size calculation was performed with PASS 12 (version 12; NCSS, LLC, Kaysville, UT; <http://www.ncss.com>).

## RESULTS

### Characteristics of Study Subjects

At baseline and at apnea, the groups had similar vital signs and biochemical variables (Tables 1 and 2). At time zero, predefined as apnea of 1 minute's duration, there were no significant differences among groups (Table 3). Reduction in mean arterial blood pressure from baseline was also similar among groups (29%, 38%, and 36% decrease;  $P=.35$ ).

### Main Results

The time to return of spontaneous breathing between the 2 antidote-treated groups was similar: hydroxocobalamin group (1 minute 48 seconds [SD 29 seconds]), and cobinamide group (1 minute 49 seconds [SD 31 seconds]). This was significantly different from the control group (5 of 11 animals had return of spontaneous breathing and 6 of 11 remained apneic; 4 minutes 5 seconds [SD 40 seconds];  $P=.005$ ). One animal in the hydroxocobalamin group, 1 animal in the

**Table 1.** Baseline characteristics of animals in each group before receiving cyanide infusion.\*

Characteristics at Baseline	Hydroxocobalamin (65 mg/kg IV) (N=10)	Cobinamide (12.5 mg/kg IV) (N=10)	Control (Saline Solution) (N=11)
Weight, kg	49.9 (3.9)	52.7 (3.09)	51 (2.86)
Pulse rate, beats/min	76.7 (10.69)	84.9 (14.72)	85.55 (23.56)
Systolic blood pressure, mm Hg	122.9 (12.42)	120.7 (16.46)	119.36 (16.75)
MAP, mm Hg	99.2 (12.35)	97.9 (13.86)	96.09 (17)
Cardiac output, L/min	4.97 (0.98)	6.03 (1.13)	5.13 (1.28)
Systemic vascular resistance, dynes-s/cm <sup>5</sup>	1,564.2 (464.9)	1,244.9 (221.32)	1,418.9 (303.27)
pH, mEq/L	7.46 (0.02)	7.47 (0.03)	7.47 (0.02)
Bicarbonate, mEq/L	27.81 (1.26)	27.56 (2)	28.43 (2.24)
Lactate, mmol/L	1.06 (0.38)	1.1 (0.46)	0.89 (0.31)

IV, Intravenous, MAP, mean arterial pressure.

\*Data are presented as mean (SD).

cobinamide group, and 9 animals in the control group died before completion of the experiment, ie, between receiving the antidote or saline solution at 1 minute after onset of apnea and 60 minutes later (Figure 1). Consequently, the 3 groups showed a difference in the Kaplan-Meier survival estimation (90% survival in hydroxocobalamin and cobinamide animals, 10% in control) and time to death compared with controls ( $P<.001$ ). Outcome variables for the control group are reported until more than half of the animals died, which occurred at 30 minutes after time zero. Of the antidote-treated animals that survived, respiratory rate, mean arterial pressure, pulse rate, cardiac output, and central mixed venous oxygenation all trended toward baseline after treatment (Figure 2A through E and Figure E2 available at [www.annemergmed.com](http://www.annemergmed.com)). There were no significant differences in respiratory rate, cardiac output, or mixed venous oxygenation between treatment groups from time zero to 60 minutes. Mean arterial pressure was significantly different between the 2 antidote-treated groups ( $P<.05$ ) such that pigs in the hydroxocobalamin-treated group demonstrated an increased

**Table 2.** Characteristics for each group at apnea of the cyanide-poisoned animals.\*

Characteristics at Apnea	Hydroxocobalamin (65 mg/kg IV) (N=10)	Cobinamide (12.5 mg/kg IV) (N=10)	Control (Saline Solution) (N=11)
Cyanide dose, mg/kg	1.91 (0.7)	1.85 (0.53)	1.67 (0.53)
Time to apnea, min:s	11:12 (04:04)	10:54 (03:07)	09:49 (03:05)

\*Data are presented as mean (SD).

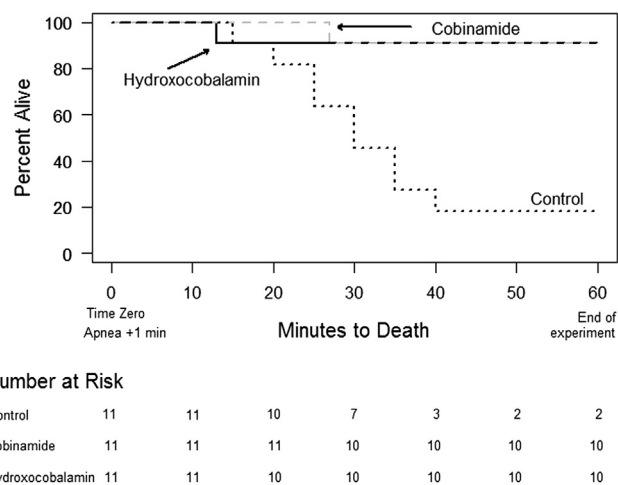
**Table 3.** Characteristics for each group at time zero (1 minute of apnea) of the cyanide-poisoned animals.\*

Characteristics at 1 Minute of Apnea	Hydroxocobalamin (65 mg/kg IV) (N=10)	Cobinamide (12.5 mg/kg IV) (N=10)	Control (Saline Solution) (N=11)
MAP at apnea, mm Hg	70 (17)	61 (20)	58 (27)
Lactate, mmol/L	3.4 (1.3)	3.7 (0.9)	3.2 (1.1)
Cyanide level, µg/mL	1.83 (0.51)	1.68 (0.36)	1.76 (0.59)
pH	7.38 (0.05)	7.36 (0.05)	7.38 (0.07)

\*Data are presented as mean (SD).

mean arterial pressure at 5 minutes through 50 minutes postapnea. Moreover, pulse rate was significantly faster at times 5 to 15 minutes in the hydroxocobalamin-treated animals compared with cobinamide-treated animals. However, post hoc analysis at the individual times revealed no statistical difference by the end of the experiment (88 [SD 15.2] 15.2 mm Hg hydroxocobalamin and 71 [SD 10] 10 mm Hg cobinamide). The systolic blood pressure was also different between groups ( $P<.05$ ) but similar at the end of the experiment (112 mm Hg SD [14.1] 14.2 mm Hg IV hydroxocobalamin, 91 [SD 15.1] mm Hg IV cobinamide).

No important difference was detected between treated groups in regard to lactate, bicarbonate, pH, or cyanide concentration levels from time zero through the end of the study (Figure 3A through D and Figure E3 available at [www.annemergmed.com](http://www.annemergmed.com)). Lactate (1.2 versus 1.5 mmol/L), pH (7.44 versus 7.44), and bicarbonate (28 versus 28 mEq/L) at 60 minutes were similar in the treated groups. Immediately after treatment, cyanide was not detected in the blood of 10 of 10 hydroxocobalamin-treated animals and 7 of 10 cobinamide-treated animals. Cyanide was not detectable in any treated animal at the end of the study. The

**Figure 1.** Survival analysis using a Kaplan-Meier curve plot estimate comparing all the groups of cyanide-poisoned animals.

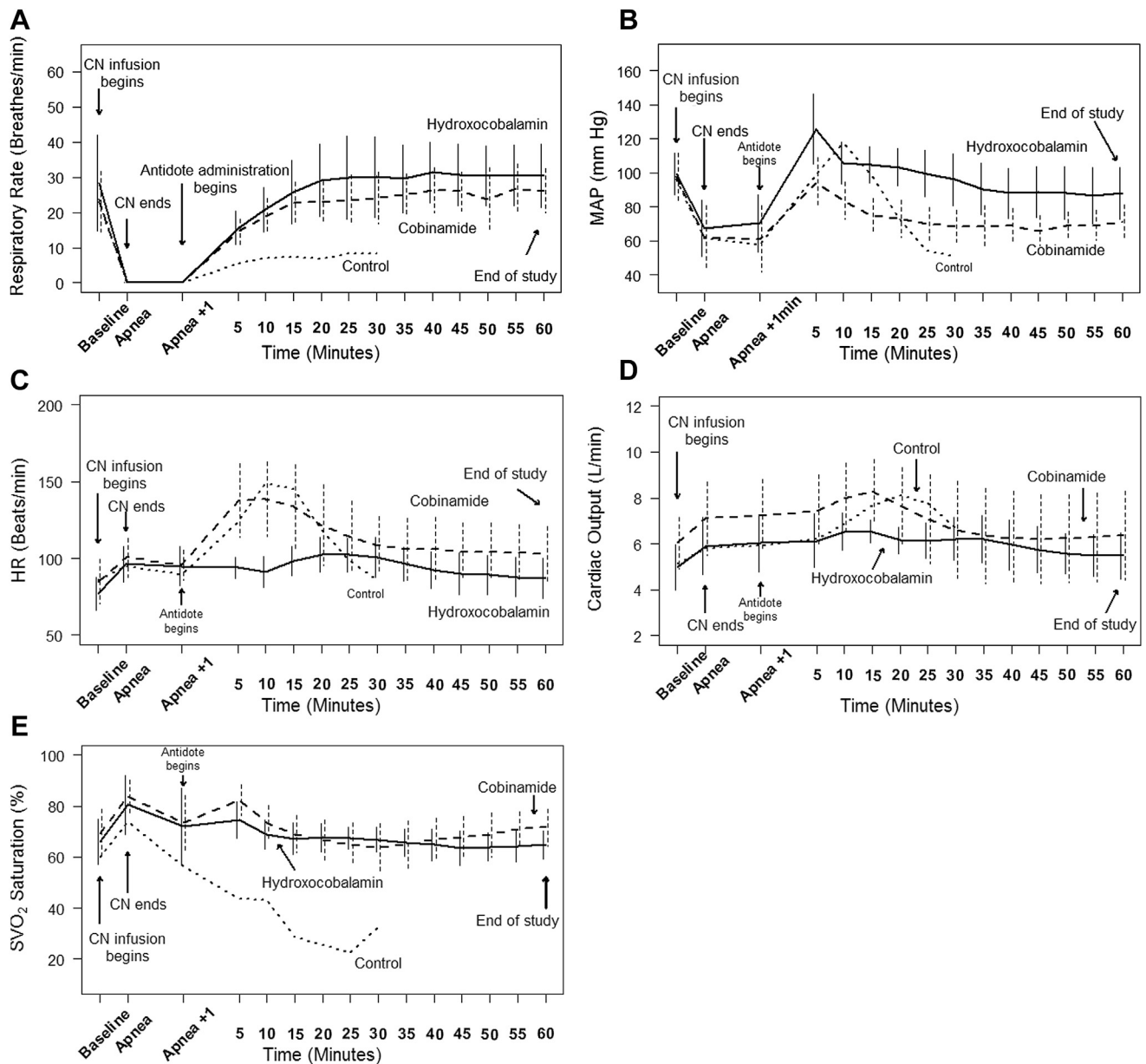


**Figure 2.** Hemodynamic variables and vital signs (respiratory rate, mean arterial pressure, pulse rate, cardiac output, and mixed venous oxygenation [SVO<sub>2</sub>] saturation) in cyanide-poisoned animals over time for the 3 groups. Values for the control arms were plotted until greater than 50% of the animals died (30 minutes). MAP, Mean arterial pressure; HR, pulse rate; CN, cyanide.

likely reason that blood cyanide was detected longer in the cobinamide-treated animals than the hydroxocobalamin-treated animals is that cobinamide binds more tightly to plasma proteins than hydroxocobalamin; thus, cobinamide was likely at a higher blood concentration than hydroxocobalamin, yielding higher cyanide concentrations.

## LIMITATIONS

This study has several limitations, the principal one being that an animal model does not precisely reproduce human toxicity. However, it clearly is not possible to administer cyanide to

humans, and animal models must be used. We have previously noted that pigs are an excellent choice for modeling cyanide exposure, given the similarities of their cardiovascular systems to that of humans.<sup>3,13,14</sup>

Another shortcoming is that we used intravenous cyanide as a substitute for inhalational exposure. Both routes have rapid onset, but the intravenous route provides a controlled method to induce toxicity compared with relatively uncontrolled cyanide absorption in an inhalational model. In addition, an inhalational route of cyanide exposure for a large animal puts the research staff at a greater risk than the intravenous route because of the potential for undetected leaks in the ventilation system.<sup>10,12,15</sup>

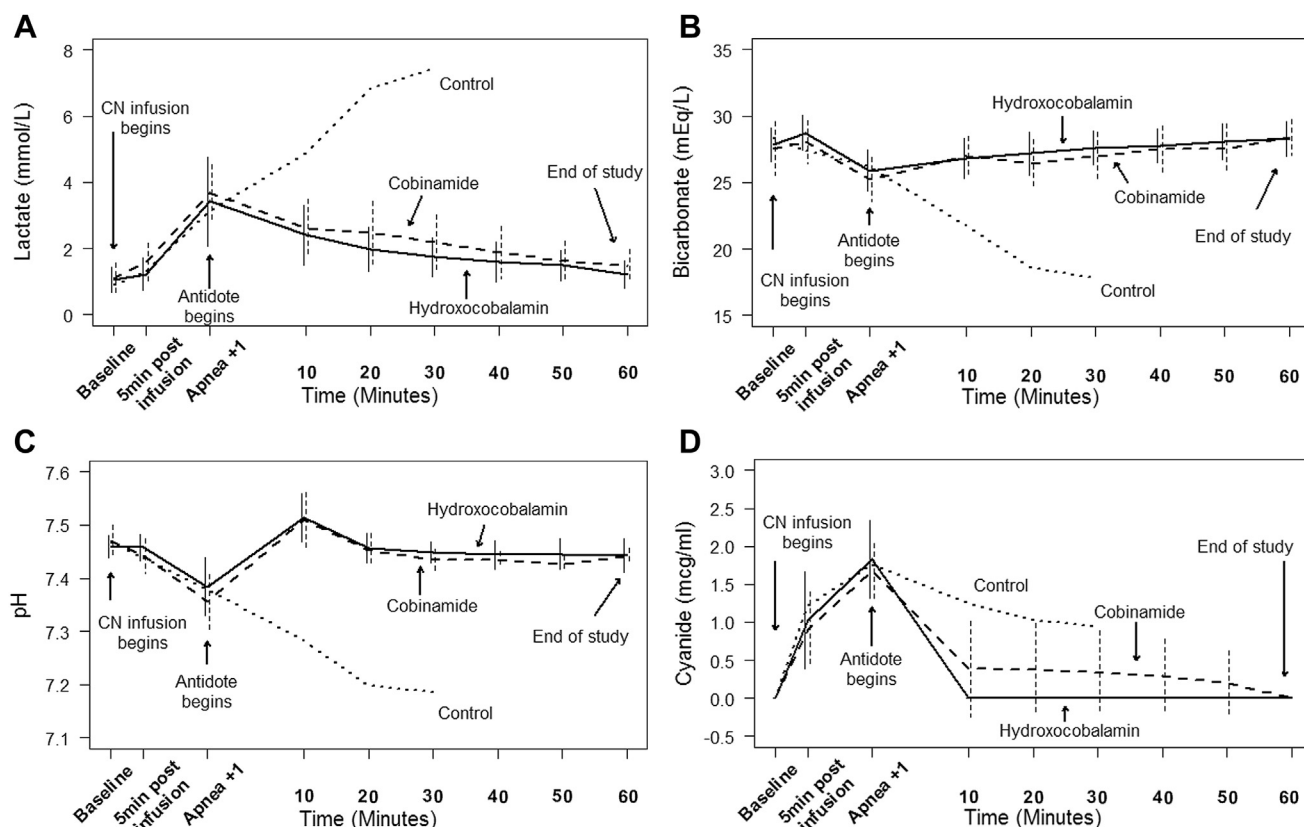


**Figure 3.** Serum markers (lactate, bicarbonate, pH, and cyanide concentrations) of cyanide-poisoned animals over time for the 3 groups. Values for the control arms were plotted until greater than 50% of the animals died (30 minutes).

A third potential concern is that we used potassium cyanide, rather than sodium cyanide. However, the potassium dose received was small, about 0.67 mEq during 10 minutes.

A fourth limitation is that we observed the animals for only 60 minutes after treatment. A longer observation period may have shown a difference between the 2 antidote-treated groups.

Finally, our study was not blinded; however, we reported objective criteria (death, breathing-based capnography, blood pressure, and cyanide levels) to limit the subjectivity of interpretation of the results.

## DISCUSSION

We expected cobinamide to provide a significantly faster and more complete rescue for cyanide-exposed animals compared with either hydroxocobalamin or saline solution. Previous investigations in our laboratory comparing the 2 antidotes in mice and rabbits suggested that cobinamide is 3 to 10 times more potent than hydroxocobalamin as a cyanide antidote, depending on the cyanide exposure model.<sup>7,8</sup> To our knowledge, this is the first investigation comparing the antidotes in a pig model of cyanide poisoning. We found no difference between cobinamide, an agent being developed as a cyanide antidote, and hydroxocobalamin, an established cyanide antidote, in terms of

the primary outcome measure of time to return of spontaneous breathing after cyanide-induced apnea. Furthermore, we found both groups similar in terms of mortality, lacticemia, acidosis, and clearance of cyanide. Although we found differences in mean arterial pressure and pulse rate between the 2 antidote-treated groups, we find it difficult to speculate about these minor cardiovascular differences because this is a small controlled animal study. Moreover, these differences had abated by the conclusion of the study.

Although no difference was noted between cobinamide and hydroxocobalamin in terms of the main outcome variable, the dose of cobinamide we used to rescue the animals was one fifth that of hydroxocobalamin, on a milligram-per-kilogram basis. This apparent increased potency may relate to the fact that each cobinamide molecule can bind, and therefore neutralize, 2 cyanide molecules compared with hydroxocobalamin, which can bind only 1 cyanide molecule.<sup>6,8,16</sup> This difference in binding capacity explains only a 2-fold increase in potency, suggesting other differences between cobinamide and hydroxocobalamin as cyanide antidotes. Two other explanations seem likely. First, cobinamide has a much higher affinity for cyanide than hydroxocobalamin ( $K_{a\text{overall}} 10^{22} \text{ M}^{-2}$  for cobinamide and  $K_a 10^{12} \text{ M}^{-1}$  for hydroxocobalamin).<sup>17</sup> This could allow cobinamide to more effectively remove cyanide from cytochrome c oxidase than hydroxocobalamin; we have



previously shown that cobinamide is more potent than hydroxocobalamin in reversing cyanide inhibition of cellular respiration.<sup>6</sup> Cytochrome c oxidase is one of the primary molecular targets of cyanide and is part of complex IV of the mitochondrial electron transport system. Second, we have preliminary evidence that cobinamide is transported into cells more rapidly and completely than hydroxocobalamin. Together, these 3 differences between cobinamide and hydroxocobalamin of increased cyanide binding capacity, increased cyanide binding affinity, and increased cellular transport could explain the apparent increased potency of cobinamide as a cyanide antidote.

There are 2 major differences between our study and previous work on animal models of cyanide poisoning. First, we used 50-kg Yorkshire pigs instead of rodents, rabbits, or dogs, which have been more commonly used in studies of cyanide toxicity.<sup>7,12,15,18</sup> Second, ours was a strictly nonventilated model.

We chose pigs because they are close in size to humans, thereby minimizing scaling issues, and because their cardiovascular system is similar to that of humans.<sup>3,13,14</sup> Drug doses are generally converted from one species to another with body surface area, but this may not be appropriate for all drugs, and less scaling will usually lead to a more accurate estimate of the proper human dose. The heart and brain are generally considered the 2 primary targets of cyanide, and thus, using an animal model that has a cardiovascular system close to that of humans allows one to apply the results to humans more confidently. In addition, we have reported swine models of cyanide-induced cardiac arrest and of shock.<sup>3,9,10</sup>

In the out-of-hospital setting of a major cyanide exposure such as a massive fire or a terrorist attack, it is extremely unlikely that sufficient time or resources will be available to intubate and ventilate the large number of cyanide-exposed victims.<sup>8</sup> Thus, we chose not to ventilate our animals as a means to more accurately simulate such a scenario. This considerably narrows the window of time available to rescue an animal from cyanide exposure, and we elected to treat the pigs after 1 minute of apnea. Although this could be considered a relatively short period of apnea, it is not realistic to think that humans can be rescued fully after several minutes of apnea. We believe that the advantages of simulating a mass casualty scenario of no artificial ventilation outweigh the disadvantage of treatment after 1 minute of apnea.

Now that we have shown that intravenous cobinamide is comparable to intravenous hydroxocobalamin in a swine model of acute cyanide toxicity, the next step is to evaluate cobinamide delivered by nonintravenous routes. To that end, we currently have multiple ongoing swine studies evaluating the efficacy of intraosseous and intramuscular administration of cobinamide in a similar model.

In conclusion, no difference was noted between intravenous cobinamide, at one fifth the dose, and intravenous hydroxocobalamin for return of spontaneous breathing after acute cyanide poisoning in a nonventilated swine model.

*Supervising editor:* Matthew D. Sztajnkrzyer, MD, PhD

*Author affiliations:* From Medical Toxicology (Bebarta) and the Department of Emergency Medicine (Boudreau, Castaneda, Zarzabal, Vargas), San Antonio Military Medical Center, San Antonio, TX; the David Geffen School of Medicine at UCLA, Harbor-UCLA Medical Center, Torrance, CA (Tanen); and the University of California, San Diego, San Diego, CA (Boss).

*Author contributions:* VSB, DAT, and GRB conceived and designed the trial and drafted the article. VSB obtained research funding and supervised the conduct of the study and data collection. VSB, SB, MC, and TV performed the study. LAZ provided statistical advice on study design, analyzed the data, and prepared the graphs. All authors contributed substantially to article revision. VSB takes responsibility for the paper as a whole.

*Funding and support:* By *Annals* policy, all authors are required to disclose any and all commercial, financial, and other relationships in any way related to the subject of this article as per ICMJE conflict of interest guidelines (see [www.icmje.org](http://www.icmje.org)). The authors have stated that no such relationships exist and provided the following details: The study was funded by the US Air Force Office of the Surgeon General (SG5, FWH20100170A) and the CounterACT Program, Office of the Director, National Institutes of Health (OD) and the National Institutes of Neurological Disorders and Stroke (NINDS), grant U01NS058030. No other funding was used.

*Publication dates:* Received for publication July 2, 2013. Revision received December 12, 2013. Accepted for publication February 7, 2014. Available online April 18, 2014. Corrections to Figure 3D available online October 21, 2014.

Presented at the Society for Academic Emergency Medicine meeting, May 2013, Atlanta, GA.

The views expressed in this article are those of the authors and do not reflect the official policy or position of the Department of the US Air Force, Department of Defense, or the US government.

## REFERENCES

1. Thompson JP, Marrs TC. Hydroxocobalamin in cyanide poisoning. *Clin Toxicol (Phila)*. 2012;50:875-885.
2. Borron SW, Baud FJ, Barriot P, et al. Prospective study of hydroxocobalamin for acute cyanide poisoning in smoke inhalation. *Ann Emerg Med*. 2007;49:794-801.e1-e2.
3. Bebarta VS, Pitotti RL, Dixon P, et al. Hydroxocobalamin versus sodium thiosulfate for the treatment of acute cyanide toxicity in a swine (*Sus scrofa*) model. *Ann Emerg Med*. 2012;59:532-539.
4. Jett DA, Yeung DT. The CounterACT Research Network: basic mechanisms and practical applications. *Proc Am Thorac Soc*. 2010;7:254-256.
5. Countermeasures Against Chemical Threats (CounterACT) Exploratory/Developmental Projects in Translational Research (R21). National Institutes of Health; Bethesda, MD. 2013. Available at: <http://grants.nih.gov/grants/guide/pa-files/PAR-13-005.html>. Accessed March 23, 2014.
6. Brenner M, Mahon SB, Lee J, et al. Comparison of cobinamide to hydroxocobalamin in reversing cyanide physiologic effects in rabbits using diffuse optical spectroscopy monitoring. *J Biomed Opt*. 2010;15:017001.

7. Chan A, Balasubramanian M, Blackledge W, et al. Cobinamide is superior to other treatments in a mouse model of cyanide poisoning. *Clin Toxicol (Phila)*. 2010;48:709-717.
8. Brenner M, Kim JG, Mahon SB, et al. Intramuscular cobinamide sulfate in a rabbit model of sublethal cyanide toxicity. *Ann Emerg Med*. 2010;55:352-363.
9. Bebarta VS, Pitotti RL, Dixon PS, et al. Hydroxocobalamin and epinephrine both improve survival in a swine model of cyanide-induced cardiac arrest. *Ann Emerg Med*. 2012;60:415-422.
10. Bebarta VS, Tanen DA, Laiet J, et al. Hydroxocobalamin and sodium thiosulfate versus sodium nitrite and sodium thiosulfate in the treatment of acute cyanide toxicity in a swine (*Sus scrofa*) model. *Ann Emerg Med*. 2010;55:345-351.
11. Hughes C, Lehner F, Dirikolu L, et al. A simple and highly sensitive spectrophotometric method for the determination of cyanide in equine blood. *Toxicol Mechanisms Methods*. 2003;13:129-138.
12. Borron SW, Stonerook M, Reid F. Efficacy of hydroxocobalamin for the treatment of acute cyanide poisoning in adult beagle dogs. *Clin Toxicol (Phila)*. 2006;44(suppl 1):5-15.
13. Idris AH, Becker LB, Ornato JP, et al. Utstein-style guidelines for uniform reporting of laboratory CPR research. A statement for healthcare professionals from a task force of the American Heart Association, the American College of Emergency Physicians, the American College of Cardiology, the European Resuscitation Council, the Heart and Stroke Foundation of Canada, the Institute of Critical Care Medicine, the Safar Center for Resuscitation Research, and the Society for Academic Emergency Medicine Writing Group. *Circulation*. 1996;94:2324-2336.
14. Hannon JP, Bossone CA, Wade CE. Normal physiological values for conscious pigs used in biomedical research. *Lab Anim Sci*. 1990;40:293-298.
15. Vick J, Marino MT, von Bredow JD, et al. A reproducible nonlethal animal model for studying cyanide poisoning. *Mil Med*. 2000;165:967-972.
16. Broderick KE, Potluri P, Zhuang S, et al. Cyanide detoxification by the cobalamin precursor cobinamide. *Exp Biol Med (Maywood)*. 2006;231:641-649.
17. Broderick KE, Balasubramanian M, Chan A, et al. The cobalamin precursor cobinamide detoxifies nitroprusside-generated cyanide. *Exp Biol Med (Maywood)*. 2007;232:789-798.
18. Brenner M, Kim JG, Mahon SB, et al. Intramuscular cobinamide sulfate in a rabbit model of sublethal cyanide toxicity. *Ann Emerg Med*. 2010;55:352-363.

## Most-Read Articles You May Have Missed

This is one of the top 5 most cited *Annals* articles in the last five years (97 cites). Be sure to read the full article in the March 2009 issue on [www.annemergmed.com](http://www.annemergmed.com).

### CARDIOLOGY/ORIGINAL RESEARCH

#### Coronary Computed Tomographic Angiography for Rapid Discharge of Low-Risk Patients With Potential Acute Coronary Syndromes

Judd E. Hollander, MD  
Anna Marie Chang, MD  
Frances S. Shofer, PhD  
Christine M. McCusker, RN,  
BSN  
William G. Baxt, MD  
Harold I. Litt, MD, PhD

From the Departments of Emergency Medicine (Hollander, Chang, Shofer, McCusker, Baxt) and Radiology (Litt), Hospital of the University of Pennsylvania, Philadelphia, PA.

**Study objective:** Coronary computed tomographic (CT) angiography has excellent performance characteristics relative to coronary angiography and exercise or pharmacologic stress testing. We hypothesize that coronary CT angiography can identify a cohort of emergency department (ED) patients with a potential acute coronary syndrome who can be safely discharged with a less than 3% risk of 30-day cardiovascular death or nonfatal myocardial infarction.

**Methods:** We conducted a prospective cohort study at an urban university hospital ED that enrolled consecutive patients with potential acute coronary syndromes and a low TIMI risk score who presented to the ED with symptoms suggestive of a potential acute coronary syndrome and received a coronary CT angiography. Our intervention was either immediate coronary CT angiography in the ED or after a 9- to 12-hour observation period that included cardiac marker determinations, depending on time of day. The main clinical outcome was 30-day cardiovascular death or nonfatal myocardial infarction.

**Results:** Five hundred sixty-eight patients with potential acute coronary syndrome were evaluated; 285 of these received coronary CT angiography immediately in the ED and 283 received coronary CT angiography after a brief observation period. Four hundred seventy-six (84%) were discharged home after coronary CT angiography. During the 30-day follow-up period, no patients died of a cardiovascular event (0%); 95% confidence interval (CI) 0% to 0.8% or sustained a nonfatal myocardial infarction (0%); 95% CI 0 to 0.8%.

**Conclusion:** ED patients with symptoms concerning for a potential acute coronary syndrome with a low TIMI risk score and a nonischemic initial ECG result can be safely discharged home after a negative coronary CT angiography test result. [*Ann Emerg Med*. 2009;53:295-304.]

0190-0044/\$-see front matter  
Copyright © 2008 by the American College of Emergency Physicians.  
doi:10.1016/j.annemergmed.2008.09.025

#### SEE EDITORIAL, P. 305.

#### INTRODUCTION

##### Background

Approximately 6 million patients present to the emergency department (ED) annually with a complaint of chest pain or other symptoms suggestive of myocardial ischemia.<sup>1</sup> 55% to 85% of whom do not have a cardiac cause for their symptoms.<sup>2-10</sup> Eight to 10 billion dollars are spent annually on hospital stays to rule out an acute coronary syndrome.<sup>4,5,10</sup> Although the identification of high-risk patients has improved during the past 20 years,<sup>4-6</sup> the rapid cost-effective evaluation and accurate

identification of low-risk patients remain problematic.<sup>7,7-9,17</sup> Clinical and computerized algorithms can successfully risk-stratify patients; however, they cannot identify a group of patients at such low risk that they can be safely and immediately released from the ED with a less than 1% risk of 30-day adverse events.<sup>8,9,17</sup>

##### Importance

Coronary computed tomographic (CT) angiography has excellent correlation with cardiac catheterization, and studies have shown that it has a sensitivity of 93% to 100% and specificity of 75% to 98% for identification of coronary artery

Volume 53, No. 3 : March 2009

Annals of Emergency Medicine 295

## Nitrocobinamide, a New Cyanide Antidote That Can Be Administered by Intramuscular Injection

Adriano Chan,<sup>†</sup> Jingjing Jiang,<sup>†</sup> Alla Fridman,<sup>†</sup> Ling T. Guo,<sup>‡</sup> G. Diane Shelton,<sup>‡</sup> Ming-Tao Liu,<sup>‡</sup> Carol Green,<sup>‡</sup> Kristofer J. Haushalter,<sup>§</sup> Hemal H. Patel,<sup>||,¶</sup> Jangwoon Lee,<sup>∞</sup> David Yoon,<sup>∞</sup> Tanya Burney,<sup>∞</sup> David Mukai,<sup>∞</sup> Sari B. Mahon,<sup>∞</sup> Matthew Brenner,<sup>∞</sup> Renate B. Pilz,<sup>†</sup> and Gerry R. Boss<sup>\*,†</sup>

Departments of <sup>†</sup>Medicine, <sup>‡</sup>Pathology, <sup>§</sup>Chemistry and Biochemistry, and <sup>||</sup>Anesthesiology, University of California—San Diego, La Jolla, California 92093-0652, United States

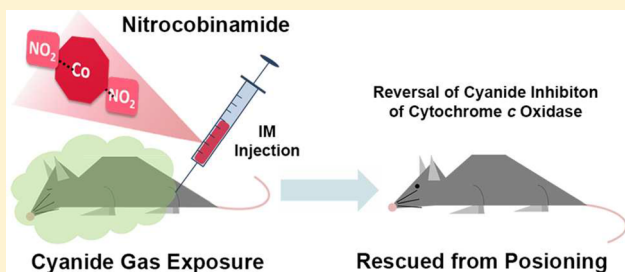
<sup>‡</sup>SRI International, Menlo Park, California 94025-3493, United States

<sup>¶</sup>VA San Diego Healthcare System, San Diego, California 92161, United States

<sup>∞</sup>Beckman Laser Institute and Medical Clinic, University of California—Irvine, Irvine, California 92697, United States

**S** Supporting Information

**ABSTRACT:** Currently available cyanide antidotes must be given by intravenous injection over 5–10 min, making them ill-suited for treating many people in the field, as could occur in a major fire, an industrial accident, or a terrorist attack. These scenarios call for a drug that can be given quickly, e.g., by intramuscular injection. We have shown that aquohydroxocobinamide is a potent cyanide antidote in animal models of cyanide poisoning, but it is unstable in solution and poorly absorbed after intramuscular injection. Here we show that adding sodium nitrite to cobinamide yields a stable derivative (referred to as nitrocobinamide) that rescues cyanide-poisoned mice and rabbits when given by intramuscular injection. We also show that the efficacy of nitrocobinamide is markedly enhanced by coadministering sodium thiosulfate (reducing the total injected volume), and we calculate that ~1.4 mL each of nitrocobinamide and sodium thiosulfate should rescue a human from a lethal cyanide exposure.



## INTRODUCTION

Cyanide is a very potent and rapidly acting poison. Over one billion pounds are used each year in the United States in a variety of industries, including electroplating, paint manufacturing, and gold extraction from ore.<sup>1</sup> Moreover, it is relatively easy to make from simple reagents, making it available for nefarious use. Thus, a large number of people could be exposed to cyanide in either a major industrial accident or a terrorist attack. In addition, cyanide may be as important as carbon monoxide as a cause of inhalational deaths in residential and industrial fires.<sup>2,3</sup>

Two treatments for cyanide poisoning are currently available in the United States: hydroxocobalamin (Cyanokit) and the combination of sodium nitrite and sodium thiosulfate (Nithiodote). Both treatments must be given intravenously. Even in the best of settings, starting an intravenous line can take several minutes, and in a clothed hypotensive subject, obtaining venous access can be particularly challenging. Moreover, both hydroxocobalamin and sodium nitrite/sodium thiosulfate are recommended to be given over 5–15 min. Thus, neither antidote is suitable for use in the field, particularly for a mass casualty scenario, and an antidote that can be given quickly and easily is urgently needed. The best approach would

appear to be intramuscular injection using a prefilled syringe. This requires that the antidote (i) is sufficiently potent so that it can be administered in a small volume, (ii) is rapidly absorbed after intramuscular injection, and (iii) is sufficiently stable to be stored as a solution for long periods.

We have been developing the hydroxocobalamin analog cobinamide (see Experimental Section for nomenclature) as a cyanide antidote and have shown it is 3–10 times more potent than hydroxocobalamin in mouse, rabbit, and pig models of cyanide poisoning.<sup>4–7</sup> Aquohydroxocobinamide (Supporting Information, Figure 1A) is poorly absorbed after intramuscular injection; however, we showed that placing a ligand on the cobalt atom markedly improved its absorption.<sup>4,6</sup> The first ligand we tested was sulfite, but we subsequently found that sulfitecobinamide was not stable over time. We now show that nitrocobinamide (Supporting Information, Figure 1B) is very stable and well absorbed after intramuscular injection. The amount of nitrite in a nitrocobinamide preparation is subtherapeutic, and the nitrite is present only to improve absorption after intramuscular injection.

**Received:** October 9, 2014



The combination of sodium thiosulfate and sodium nitrite was developed for cyanide poisoning because the two drugs act by different mechanisms and yield a synergistic effect.<sup>8,9</sup> Thiosulfate also synergizes with hydroxocobalamin, as well as with various experimental treatments of cyanide poisoning.<sup>10–13</sup> The mechanism whereby thiosulfate potentiates other drugs is unknown, but we hypothesized thiosulfate might potentiate cobinamide, allowing a reduction of the cobinamide dose and thus injection volume. We now show that combining a small amount of thiosulfate with nitrocobinamide yields a potent cyanide antidote and that the two drugs can be given in small volumes by intramuscular injection. The major antidotal potency of the drug combination is derived from combining thiosulfate with the cobinamide in nitrocobinamide, not with the nitrite.

## RESULTS

**Nitrite Binding to Aquohydroxocobinamide.** Nitrite has a reasonably high affinity for cobalamin,<sup>14</sup> and we hypothesized that nitrite might bind tightly enough to cobinamide to allow the nitrocobinamide derivative to be absorbed after intramuscular injection (as described in the Experimental Section, we use the generic term “nitrocobinamide” to refer to cobinamide in the presence of nitrite, without specifying the number of bound nitrite groups). Ligand binding to cobinamide and cobalamin changes the molecules’ ultraviolet–visible spectrum, and we found that adding one or two nitrite equivalents to a concentrated aquohydroxocobinamide solution yielded cobinamide derivatives with distinctly different spectra; the resulting derivatives were presumably mononitrocobinamide and dinitrocobinamide, respectively (Figure 1A). Both spectra were different from that of aquohydroxocobinamide (Figure 1A).

Because of a negative trans effect, once a ligand binds to one of cobinamide’s two free binding sites, affinity for the second ligand is reduced considerably.<sup>15</sup> Thus, cobinamide’s affinity for a first cyanide molecule is  $>10^{14} \text{ M}^{-1}$  (and may approach  $10^{19} \text{ M}^{-1}$ ), whereas the affinity for a second cyanide molecule is  $\sim 10^8 \text{ M}^{-1}$ .<sup>15,16</sup> It seemed likely, therefore, that cobinamide’s affinity for a first nitrite ligand would be greater than for a second nitrite ligand, and we found that diluting a concentrated dinitrocobinamide solution in water changed the spectrum to that of mononitrocobinamide (Supporting Information, Figure 2A; the dinitrocobinamide solution was made with two moles of sodium nitrite per mole of cobinamide). This indicated that water or hydroxyl molecules competed effectively with, and thereby displaced, the second nitrite ligand but that they did not displace the first nitrite ligand. This suggested that if we increased the nitrite concentration relative to the cobinamide concentration, the second nitrite ligand should remain bound at lower cobinamide concentrations, since more nitrite molecules will be available to compete with the water and hydroxyl molecules. We therefore repeated the experiment at four molar equivalents of sodium nitrite per mole of cobinamide and found that cobinamide remained as dinitrocobinamide until relatively low concentrations (Supporting Information, Figure 2B).

We then determined the  $K_a$  for the first and second nitrite ligands of cobinamide and found they were  $1 \times 10^5$  and  $2 \times 10^3 \text{ M}^{-1}$ , respectively (Figure 1B and Figure 1C). The  $K_a$  for the first nitrite ligand was determined at a cobinamide concentration of  $10 \mu\text{M}$  (to minimize interference by binding of the second nitrite ligand), and the  $K_a$  for the second nitrite ligand

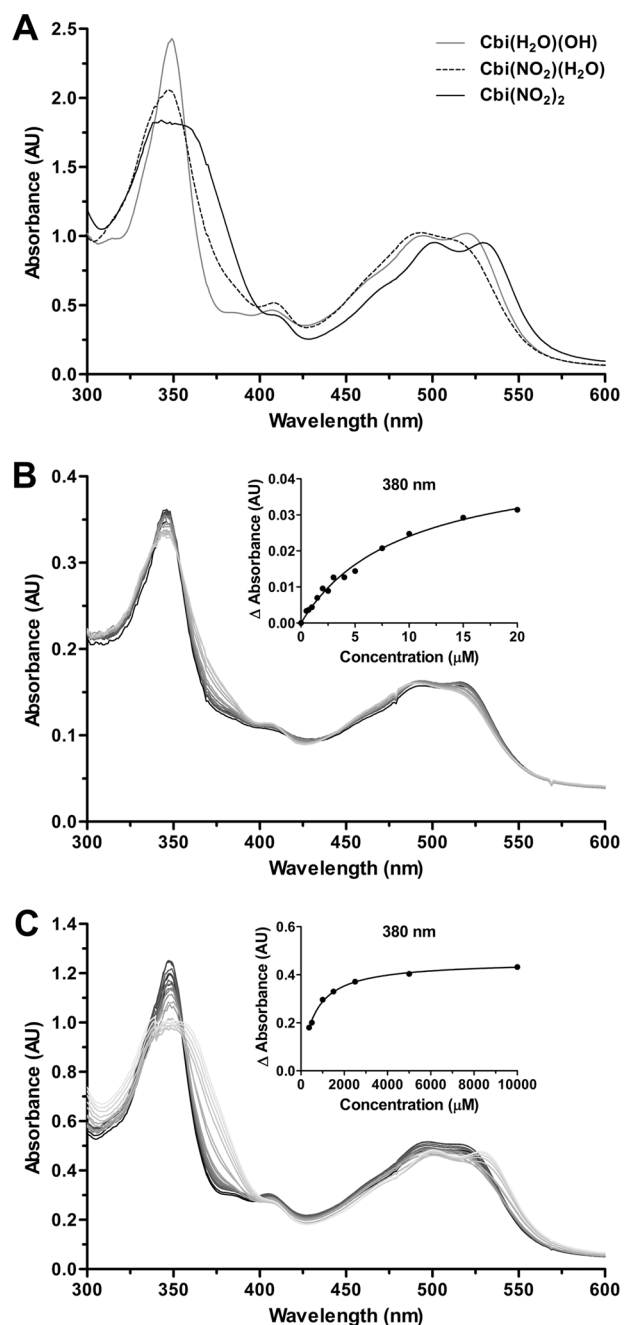


**Figure 1.** Nitrite binding to aquohydroxocobinamide. (A) A 100 mM solution of aquohydroxocobinamide [ $\text{Cbi}(\text{H}_2\text{O})(\text{OH})$ , gray line], nitroaquocobinamide [ $\text{Cbi}(\text{NO}_2)(\text{H}_2\text{O})$ , dashed line], and  $\text{Cbi}(\text{NO}_2)_2$  (black line) in water was scanned from 300 to 600 nm in a 0.01 mm path length cuvette. The nitroaquocobinamide and  $\text{Cbi}(\text{NO}_2)_2$  were prepared by adding one and two molar equivalents, respectively, of sodium nitrite to the aquohydroxocobinamide solution; at 100 mM cobinamide, two nitrite equivalents saturate both ligand binding sites. (B, C) Increasing amounts of sodium nitrite were added to a  $10 \mu\text{M}$  (B) and  $500 \mu\text{M}$  (C) aquohydroxocobinamide solution at the following ratios of nitrite to aquohydroxocobinamide: 0.25X, 0.5X, 0.75X, 1X, 2X, 3X, 4X, 5X, 10X, and 20X. The spectra from 300 to 600 nm were recorded, with the aquohydroxocobinamide spectrum shown in black and the spectra with increasing nitrite concentrations shown in shades of gray from dark to light. Insets: The difference in absorption at 380 nm between the presence and absence of sodium nitrite was plotted, and a best fit equation was used to determine the binding affinity for the first and second binding sites.



was determined at a cobinamide concentration of 500  $\mu\text{M}$  (to minimize competition by water and hydroxyl molecules).

**Nitrocobinamide Converts Readily to Dicyanocobinamide and Effectively Scavenges Cyanide in Cultured Cells.** For nitrocobinamide to be an effective cyanide scavenger, cyanide needs to displace the nitrite ligands efficiently. We assessed cyanide binding to nitrocobinamide in two sets of experiments. First, we showed that adding two molar equivalents of cyanide to a nitrocobinamide solution immediately changed the spectrum to that of dicyanocobinamide<sup>17</sup> [Figure 2A]; the data shown are for cobinamide in the presence of four molar equivalents of sodium nitrite (designated subsequently as  $\text{Cbi}(\text{NO}_2)_4$ ), but similar results were obtained with cobinamide in the presence of two molar equivalents of sodium nitrite (designated subsequently as  $\text{Cbi}(\text{NO}_2)_2$ ). And second, we showed that both  $\text{Cbi}(\text{NO}_2)_2$  and  $\text{Cbi}(\text{NO}_2)_4$  rapidly and completely reversed cyanide-induced inhibition of cellular oxygen consumption (Figure 2B). The rate of reversal was the same as for aquohydroxocobinamide (Figure 2B), indicating no interference by the nitrite ligand. These data also indicate that cobinamide effectively removes cyanide from mitochondrial cytochrome *c* oxidase, the primary intracellular cyanide target. Cobinamide was more effective than hydroxocobalamin at reversing cyanide-induced inhibition of oxygen consumption, and neither sodium nitrite nor sodium thiosulfate counteracted cyanide's inhibition (Figure 2B). The last two agents were tested because nitrite can generate nitric oxide, which can displace cyanide from cytochrome *c* oxidase, and thiosulfate is a substrate for rhodanese, a mitochondrial cyanide-detoxifying enzyme.<sup>18–22</sup> The lack of an effect by nitrite suggests that either nitrite did not generate sufficient nitric oxide under the conditions tested or that nitrite detoxifies cyanide through other mechanisms, i.e., methemoglobin generation.<sup>23</sup> We conclude that cyanide readily displaces nitrite from nitrocobinamide and that nitrocobinamide efficiently reverses cyanide-induced inhibition of cellular oxygen consumption.

**Nitrocobinamide Stability.** Delivering an antidote from a prefilled syringe is much faster and easier than mixing the contents of two vials (one containing solid antidote and the other containing solvent) and then drawing up the dissolved antidote in a syringe. Thus, for treating mass casualties in the field, a prefilled syringe would be preferred, but the antidote must have a reasonably long shelf life as a solution. We therefore tested the stability of nitrocobinamide solutions and found that both  $\text{Cbi}(\text{NO}_2)_2$  and  $\text{Cbi}(\text{NO}_2)_4$  were stable for at least 45 days under the accelerated degradation condition of 50  $^\circ\text{C}$  and 5 months at room temperature. The accelerated degradation data can be extrapolated to a nitrocobinamide solution being stable for at least 1 year at room temperature.<sup>21,24</sup>

**Nitrocobinamide Pharmacokinetics after Intramuscular Injection.** We measured the total plasma cobinamide concentration at various times after intramuscular injection of nitrocobinamide into rabbits. We found that  $\text{Cbi}(\text{NO}_2)_2$  yielded a similar maximal plasma concentration as  $\text{Cbi}(\text{NO}_2)_4$  but that the time to maximal concentration ( $T_{\text{max}}$ ) was markedly different at  $\sim 250$  and 45 min, respectively (Figure 3A). Moreover, the difference between the two nitrocobinamide formulations in the time to half maximal plasma concentration ( $T_{1/2\text{max}}$ ) was even more dramatic:  $T_{1/2\text{max}}$  for  $\text{Cbi}(\text{NO}_2)_4$  and  $\text{Cbi}(\text{NO}_2)_2$  was  $\sim 4$  and  $\sim 90$  min, respectively (Figure 3A). Because of cobinamide's red color, the difference

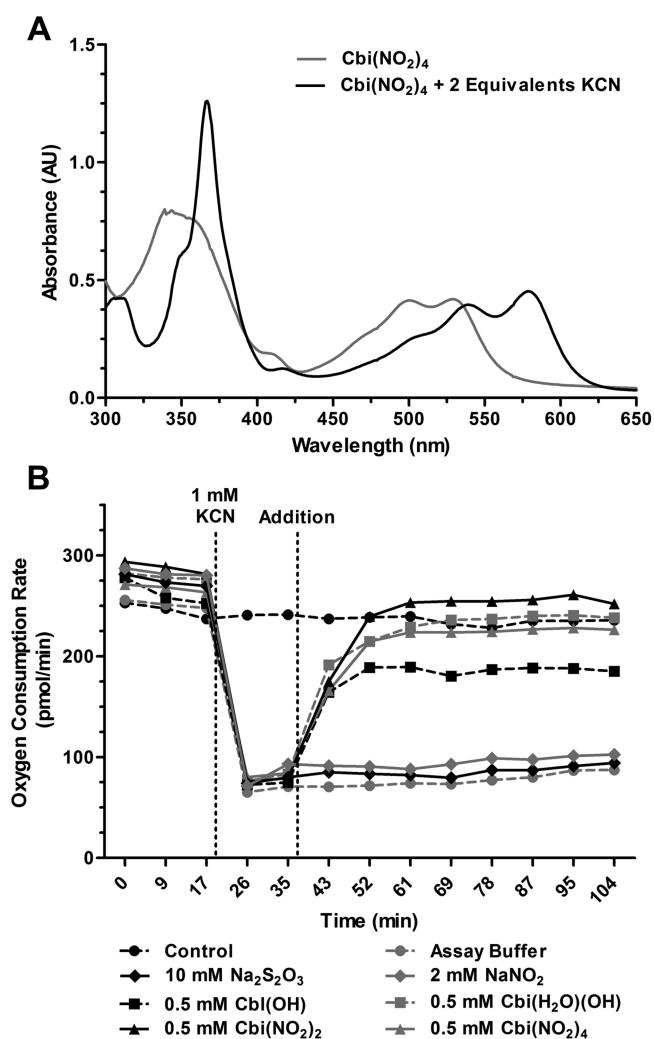


**Figure 2.** Nitrocobinamide conversion to dicyanocobinamide and reversal of cyanide inhibition of mitochondrial respiration. (A) To a 50 mM  $\text{Cbi}(\text{NO}_2)_2$  solution was added KCN to a final concentration of 100 mM. The UV-visible spectra from 300 to 650 nm were recorded immediately before (gray line) and after adding the cyanide (black line). (B) Oxygen consumption rates were measured in COS-7 monkey kidney fibroblasts using a Seahorse Bioscience XF24 extracellular flux analyzer. At the indicated time (vertical line at 19 min), KCN at a final concentration of 1 mM was added to all of the cells except control cells (black circles, dashed line), and 18 min later the following agents were added to the final concentrations noted: XF assay buffer (gray circles, dashed line), 10 mM sodium thiosulfate ( $\text{Na}_2\text{S}_2\text{O}_3$ , black diamonds, solid line), 2 mM sodium nitrite ( $\text{NaNO}_2$ , gray diamonds, solid line), 0.5 mM hydroxocobalamin [ $\text{Cbi}(\text{OH})$ , black squares, dashed line], 0.5 mM aquohydroxocobinamide [ $\text{Cbi}(\text{H}_2\text{O})(\text{OH})$ , gray squares, dashed line], 0.5 mM  $\text{Cbi}(\text{NO}_2)_2$  (black triangles, solid line), and 0.5 mM  $\text{Cbi}(\text{NO}_2)_4$  (gray triangles, solid line). Error bars are omitted for clarity, but the standard deviation about each value was  $<10\%$ .

in absorption was observed on visually inspecting the plasma (Figure 3B). The more rapid absorption of  $\text{Cbi}(\text{NO}_2)_4$  is likely from more complete saturation of cobinamide's binding sites with nitrite and therefore possibly less binding of cobinamide to large negatively charged molecules in the extracellular matrix.

We also measured the total plasma cobinamide concentration in mice 5 min after an intramuscular injection of either  $\text{Cbi}(\text{NO}_2)_2$  or  $\text{Cbi}(\text{NO}_2)_4$  and found concentrations of  $75.5 \pm 2.6$  and  $167.3 \pm 76.61$   $\mu\text{M}$ , respectively (mean  $\pm$  SD,  $n = 4$  in

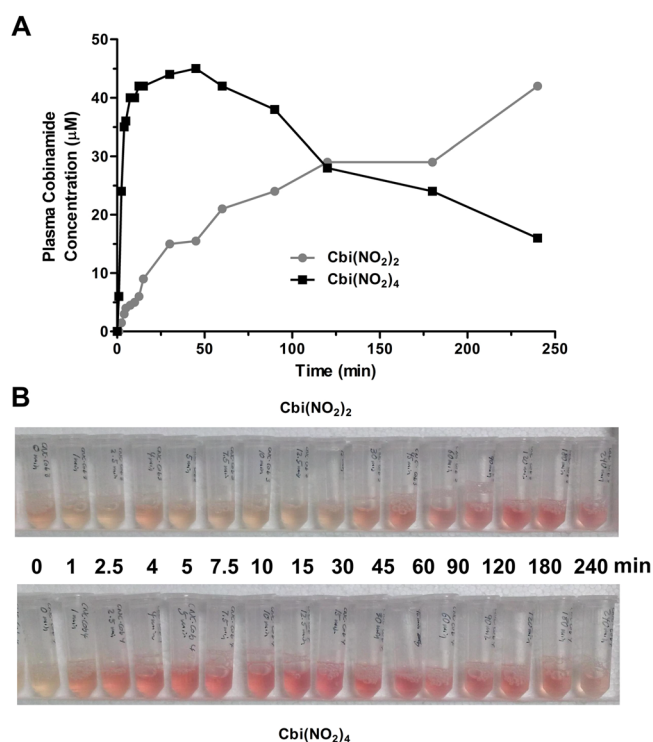


**Figure 3.** Pharmacokinetics of nitrocobinamide after intramuscular injection. Equal volumes (80  $\mu\text{L}$ ) of 200 mM Cbi(NO<sub>2</sub>)<sub>2</sub> or Cbi(NO<sub>2</sub>)<sub>4</sub> were injected into the pectoral muscle of anesthetized rabbits, and blood was collected at the following times: at the time of injection ("0 min") and at the following times after injection, 1, 2.5, 4, 5, 7.5, 10, 15, 30, 45, 60, 90, 120, 180, and 240 min. (A) The plasma cobinamide concentration was measured by HPLC: gray circles, [Cbi(NO<sub>2</sub>)<sub>2</sub>]; black squares, [Cbi(NO<sub>2</sub>)<sub>4</sub>]. The data are the mean from two independent experiments (four rabbits total). (B) Plasma samples are shown for one rabbit injected with Cbi(NO<sub>2</sub>)<sub>2</sub> (upper photograph) and one with Cbi(NO<sub>2</sub>)<sub>4</sub> (lower photograph).

each group;  $p < 0.05$  for differences between the two groups). Thus, Cbi(NO<sub>2</sub>)<sub>4</sub> is better absorbed than Cbi(NO<sub>2</sub>)<sub>2</sub> in two different species.

**Muscle Analysis after Intramuscular Injection of Nitrocobinamide.** For intramuscular injection to be a usable method for administering nitrocobinamide, it would need to cause minimal amount of muscle damage at the injection site. We therefore injected 200  $\mu\text{mol/kg}$  (234 mg/kg) nitrocobinamide in mouse gastrocnemius muscle and examined the injected site over the ensuing 24 h. We found no evidence of edema or necrosis at the injection site, and at 24 h, the mice were euthanized and a histopathological examination of the muscle was performed. We found that Cbi(NO<sub>2</sub>)<sub>2</sub> caused a moderate amount of muscle injury but that Cbi(NO<sub>2</sub>)<sub>4</sub> caused only minimal muscle injury: injury scores of 2.75 and 1.58, respectively (the scoring scale is defined in the Experimental Section) (Figure 4). The muscle injury was resolved fully by 1 week after injection for both nitrocobinamide formulations. These data indicate that both Cbi(NO<sub>2</sub>)<sub>2</sub> and Cbi(NO<sub>2</sub>)<sub>4</sub> could be administered by intramuscular injection but that the latter formulation would be preferred.

**Efficacy of Nitrocobinamide as a Cyanide Antidote.** The more rapid and efficient absorption of both Cbi(NO<sub>2</sub>)<sub>4</sub> than of Cbi(NO<sub>2</sub>)<sub>2</sub> suggested the former would be a better cyanide antidote than the latter. We therefore compared these two nitrocobinamide formulations in an inhaled mouse model

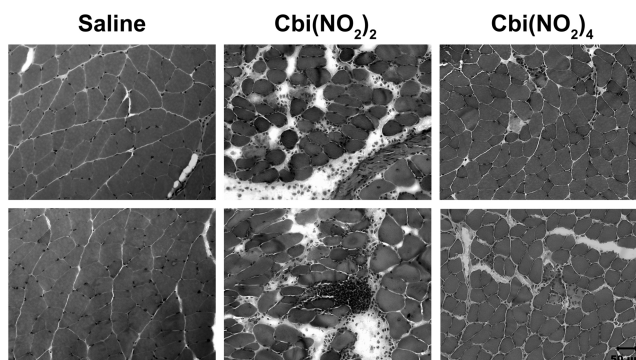


**Figure 4.** Muscle analysis after intramuscular injection of nitrocobinamide. Mice were injected in the gastrocnemius muscle with 50  $\mu\text{L}$  of saline or 50  $\mu\text{L}$  of 200  $\mu\text{mol/kg}$  (216 mg/kg) Cbi(NO<sub>2</sub>)<sub>2</sub> or Cbi(NO<sub>2</sub>)<sub>4</sub>. At 24 h after the injection, the mice were euthanized, the injected muscle was harvested, and cryosections were stained with hematoxylin and eosin. The experiments were repeated three times, with two representative areas for each condition shown. The small cells in the Cbi(NO<sub>2</sub>)<sub>2</sub>-injected muscle are polymorphonuclear leukocytes. Bar in lower right image is 50  $\mu\text{m}$  for all images.

of cyanide poisoning. As expected, intramuscular injection of aquohydroxocobinamide did not rescue animals and appeared similar to saline-injected control animals, presumably because little of the drug was absorbed (Figure 5A). Nitrocobinamide, however, did rescue animals, and we found a significant difference between Cbi(NO<sub>2</sub>)<sub>2</sub> and Cbi(NO<sub>2</sub>)<sub>4</sub>: the former at 50  $\mu\text{mol/kg}$  (54 mg/kg) yielded 50% survival, whereas the latter at 37.5  $\mu\text{mol/kg}$  (40.6 mg/kg) yielded 100% survival (Figure 5A). The difference between aquohydroxocobinamide and nitrocobinamide was not from the nitrite present in the latter, because 100  $\mu\text{mol/kg}$  (6.9 mg/kg) sodium nitrite (the amount of nitrite present in the 50  $\mu\text{mol/kg}$  Cbi(NO<sub>2</sub>)<sub>2</sub>) did not rescue any animals and 150  $\mu\text{mol/kg}$  (10.4 mg/kg) sodium nitrite (the amount of nitrite present in the 37.5  $\mu\text{mol/kg}$  Cbi(NO<sub>2</sub>)<sub>4</sub>) had only a minimal effect (Figure 5A). In a separate set of experiments, we found the protection index of Cbi(NO<sub>2</sub>)<sub>4</sub> to be 3.6 at 135  $\mu\text{mol/kg}$  (158 mg/kg) [the protection index was calculated as the LD<sub>50</sub> of cyanide in the presence of Cbi(NO<sub>2</sub>)<sub>4</sub> divided by the LD<sub>50</sub> of cyanide alone]; the dose corresponds to a likely human dose, since it rescues 50 kg pigs from a lethal cyanide exposure.<sup>7</sup> We conclude that Cbi(NO<sub>2</sub>)<sub>4</sub> is an effective cyanide antidote when administered by intramuscular injection, much more effective than aquohydroxocobinamide or an equivalent amount of sodium nitrite.

**Combination of Nitrocobinamide and Thiosulfate for Treating Cyanide Poisoning. Mouse Studies.** Having shown that Cbi(NO<sub>2</sub>)<sub>4</sub> was an effective cyanide antidote, we asked if combining it with thiosulfate would allow a reduction in the Cbi(NO<sub>2</sub>)<sub>4</sub> dose and thus injection volume. Because of the steep dose–response curve with cyanide, we found that reducing the Cbi(NO<sub>2</sub>)<sub>4</sub> dose by only half [from 37.5 to 18.8  $\mu\text{mol/kg}$  (20.3 mg/kg)] reduced survival from 100% to only 16.7% (compare Figure 5A and Figure 5B). Not surprisingly, sodium thiosulfate at a low subtherapeutic dose [75  $\mu\text{mol/kg}$  (12.6 mg/kg)] did not rescue any animals (Figure 5B; when converted to the human equivalent dose, the amount of thiosulfate was  $\sim 1$  mg/kg, which is 0.56% of the sodium thiosulfate dose in Nithiodote). However, this low amount of thiosulfate combined with 18.8  $\mu\text{mol/kg}$  Cbi(NO<sub>2</sub>)<sub>4</sub> increased survival 5-fold to 83% (Figure 5B). This marked improvement

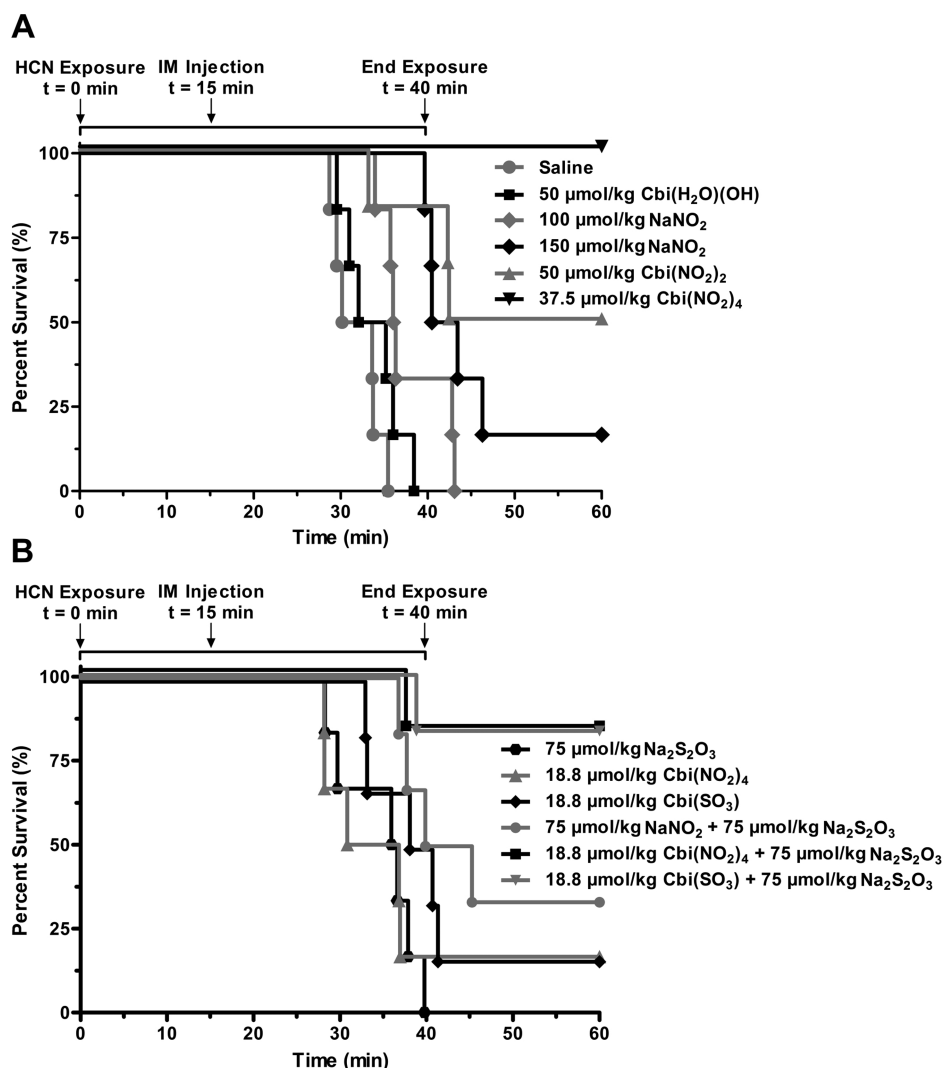


**Figure 5.** Cobinamide as a cyanide antidote in mice without and with sodium thiosulfate. C57BL/6J mice (6 animals per condition) were exposed to 587 ppm of cyanide gas (HCN) for a total of 40 min in a sealed Plexiglas chamber. After 15 min of cyanide exposure, they were removed from the chamber and received an intramuscular (IM) injection of the indicated agent(s). They were placed back in the chamber for an additional 25 min to complete the 40 min of cyanide exposure, and then they were removed from the chamber. (A) Animals were injected with saline (gray circles), 50  $\mu\text{mol/kg}$  aquohydroxocobinamide [Cbi(H<sub>2</sub>O)(OH), black squares], 100  $\mu\text{mol/kg}$  sodium nitrite [(NO<sub>2</sub>), gray diamonds], 150  $\mu\text{mol/kg}$  sodium nitrite (black diamonds), 50  $\mu\text{mol/kg}$  Cbi(NO<sub>2</sub>)<sub>2</sub> (gray triangles), or 37.5  $\mu\text{mol/kg}$  Cbi(NO<sub>2</sub>)<sub>4</sub> (black inverted triangles). (B) Animals were injected with 75  $\mu\text{mol/kg}$  sodium thiosulfate [(S<sub>2</sub>O<sub>3</sub>), black hexagons], 18.8  $\mu\text{mol/kg}$  Cbi(NO<sub>2</sub>)<sub>4</sub> (gray triangles), 18.8  $\mu\text{mol/kg}$  sulfitocobinamide [Cbi(SO<sub>3</sub>), black diamonds], 75  $\mu\text{mol/kg}$  sodium thiosulfate plus 75  $\mu\text{mol/kg}$  sodium nitrite (gray circles), 75  $\mu\text{mol/kg}$  sodium thiosulfate plus 18.8  $\mu\text{mol/kg}$  Cbi(NO<sub>2</sub>)<sub>4</sub> (black squares), or 18.8  $\mu\text{mol/kg}$  sulfitocobinamide plus 75  $\mu\text{mol/kg}$  sodium thiosulfate (inverted gray triangles). The data were divided into two graphs for ease of interpretation only; thus, any condition in each panel could have been shown in the other panel, e.g., the saline-injected controls shown in panel A could also have been shown in panel B.

in survival was not due to the combination of thiosulfate with the nitrite in Cbi(NO<sub>2</sub>)<sub>4</sub> because combining this same dose of sodium thiosulfate with the corresponding amount of sodium nitrite (75  $\mu\text{mol/kg}$ ) yielded only a modest 33.3% survival rate (Figure 5B). Thus, combining sodium thiosulfate with Cbi(NO<sub>2</sub>)<sub>4</sub> clearly improved survival over either agent alone. Moreover, the data indicate that the major improvement in survival was from combining thiosulfate with the cobinamide in Cbi(NO<sub>2</sub>)<sub>4</sub> and not the nitrite. To evaluate this interpretation of the data further, we tested sulfitocobinamide, which we previously showed is well absorbed after intramuscular injection in mice and rabbits and rescues animals from lethal cyanide concentrations.<sup>6,25</sup> We found that 18.8  $\mu\text{mol/kg}$  sulfitocobinamide yielded the same 16.7% survival rate as the identical dose of Cbi(NO<sub>2</sub>)<sub>4</sub> (Figure 5B) and that on adding sodium

thiosulfate, we once again observed a 83% survival rate (Figure 5B). Since no nitrite was present in these experiments, and we have previously shown that sulfite has no antidotal effect against cyanide, we conclude that thiosulfate augments cobinamide.<sup>25</sup>

**Rabbit Studies.** To determine if the combination of nitrocobinamide and sodium thiosulfate was effective in other species, we used a well-established lethal rabbit model of cyanide poisoning.<sup>5,6,26</sup> We found that the combination of 4  $\mu\text{mol/kg}$  (4.88 mg/kg) Cbi(NO<sub>2</sub>)<sub>4</sub> and 60  $\mu\text{mol/kg}$  (14.9 mg/kg) sodium thiosulfate rescued 80% of animals (four of five animals), whereas five of five saline-injected animals died (difference between the two groups was significant at  $p < 0.01$ ).

In addition to assessing survival, we measured the mean arterial pressure (MAP) and cytochrome *c* oxidase redox state in the animals. Because the animals were anesthetized and



ventilated, one would expect neither normal blood pressure nor cytochrome *c* oxidation, and for comparison, we used anesthetized ventilated rabbits that had received a continuous intravenous infusion of saline, instead of sodium cyanide, over the same time period. We found that the MAP and cytochrome *c* oxidation decreased by  $\sim 20$  mmHg and  $0.3 \mu\text{M}$ , respectively, in these control non-cyanide-poisoned animals (Figure 6A and

receive intravenous cyanide for 30 min after antidote injection. The initial decrease in MAP in the  $\text{Cbi}(\text{NO}_2)_4$ -thiosulfate-treated animals was likely due to several minutes being required for the  $\text{Cbi}(\text{NO}_2)_4$  to be absorbed (Figure 3) and thus to counter cyanide's hypotensive effects. The cytochrome *c* oxidase redox state rose in the  $\text{Cbi}(\text{NO}_2)_4$ -thiosulfate-treated animals, approaching that of non-cyanide-poisoned animals (Figure 6B).

In the cyanide-poisoned animals, the methemoglobin concentration was normal in both the saline- and  $\text{Cbi}(\text{NO}_2)_4$ -thiosulfate-treated groups, ranging from 2% to 4% with no more than a 2% variation throughout the studies in any animal.

## DISCUSSION AND CONCLUSIONS

A large number of agents have shown efficacy as cyanide antidotes in various animal models. These agents can be divided into at least six different classes: (i) sulfur donors, e.g., cysteine, sodium thiosulfate, and sodium tetrathionate; (ii) methemoglobin generators, e.g., amyl nitrite, sodium nitrite, and 4-dimethylaminophenol; (iii) cyanide scavengers, e.g., hydroxocobalamin, dicobalt ethylenediaminetetracetic acid, and 5,10,15,20-tetrakis(4-sulfonatophenyl)porphyrato iron encapsulated in  $\beta$ -cyclodextrin dimers; (iv) cyanohydrin formers, e.g.,  $\alpha$ -ketoglutarate, oxaloacetate, and pyruvate; (v) antioxidants, e.g., ascorbic acid, glutathione, and melatonin, and (vi) miscellaneous compounds, e.g., chlorpromazine, pyridoxal phosphate, and riboflavin.<sup>10,11,23,27–34</sup> The only ones that have been used in humans are sodium thiosulfate, amyl nitrite, sodium nitrite, 4-dimethylaminophenol, and hydroxocobalamin. As mentioned earlier, sodium thiosulfate, sodium nitrite, and hydroxocobalamin are given intravenously over 5–10 min. Amyl nitrite is inhaled, but it is not very effective.<sup>35</sup> The only one that is given by intramuscular injection is 4-dimethylaminophenol, but it is limited by toxicity due to generating unpredictable concentrations of methemoglobin.<sup>28</sup> Thus, no safe and effective cyanide antidote is currently available that can be administered by intramuscular injection, as would be needed for treating mass casualties.

We have been developing cobinamide as a cyanide antidote and found it was extremely effective at rescuing animals from lethal cyanide exposures when given by intravenous or intraperitoneal injection.<sup>4,5</sup> We were disappointed to find that aquohydroxocobinamide was absorbed poorly after intramuscular injection and hypothesized that it was binding, and thus becoming tethered, to negatively charged macromolecules in the extracellular matrix such as collagen, heparan sulfate, and chondroitin sulfate; the water molecule is easily displaced, and the hydroxyl group is readily converted to a water molecule. We reasoned that placing a ligand on cobinamide that had a reasonably high affinity for the cobalt would prevent binding to anions in the extracellular matrix. We first tested sulfitecobinamide because we knew that sulfite binds tightly to cobinamide and found that sulfitecobinamide was well absorbed after intramuscular injection and effectively rescued animals from lethal exposures to cyanide.<sup>4,6,25</sup> However, we found that sulfitecobinamide was not stable over time because of a slow redox reaction between the sulfite and cobinamide, and in a preinvestigator's new drug application meeting with the Food and Drug Administration, the agency expressed concern about possible allergic reactions to sulfite. We therefore sought a different ligand and tested a very large number of potential ligands. Because of poor solubility, limited stability, low binding affinity, or unacceptable toxicity, all but

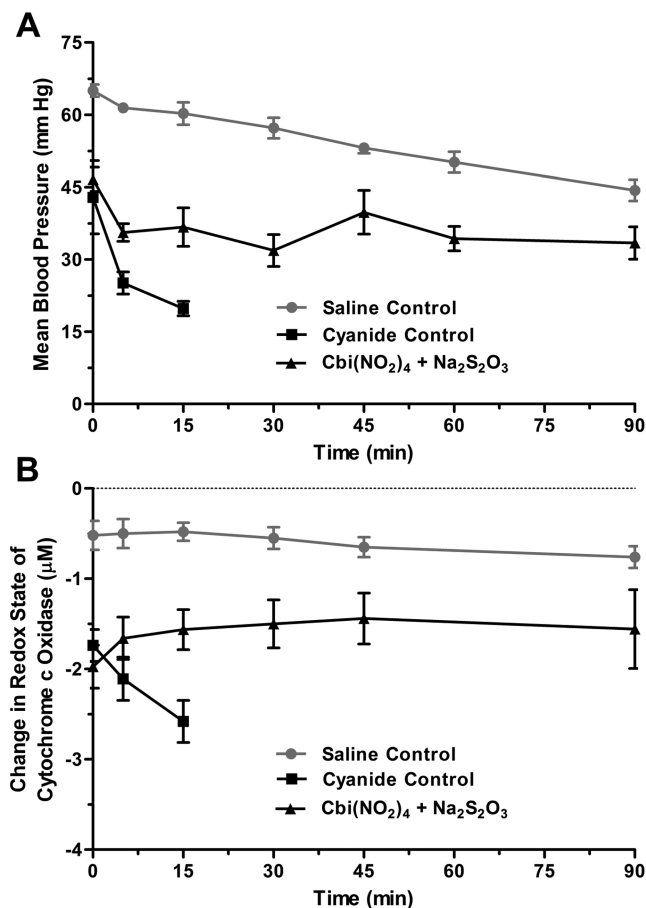


**Figure 6.** Nitrocobinamide and thiosulfate as a cyanide antidote in rabbits. New Zealand white rabbits were anesthetized and received a continuous intravenous infusion of sodium cyanide. When their MAP was  $<70\%$  of precyanide infusion values, generally after  $\sim 30$  min of cyanide infusion, the animals received an intramuscular injection of saline (cyanide control, black squares) or antidote [ $\text{Cbi}(\text{NO}_2)_4$  plus  $\text{Na}_2\text{S}_2\text{O}_3$ , black triangles]. The time of injection is defined as zero time. In separate experiments, rabbits were anesthetized and treated similarly, except they received a continuous intravenous infusion of saline (saline control, gray circles) instead of sodium cyanide and they did not receive an intramuscular injection. (A) MAP is plotted versus time. (B) Cytochrome *c* oxidase redox state is plotted versus time. The data are the mean  $\pm$  SD of three independent experiments.

Figure 6B). In the cyanide-poisoned animals, the MAP and cytochrome *c* oxidation were significantly lower than in the control animals and, in the animals that received an intramuscular injection of saline, decreased further until all the animals had died by 15 min after injection (Figure 6A and Figure 6B). The MAP in the  $\text{Cbi}(\text{NO}_2)_4$ -thiosulfate-treated animals decreased by  $\sim 8$  mmHg within the first 5 min after antidote injection and then stabilized, remaining at  $\sim 40$  mmHg until the animals were euthanized at 90 min (Figure 6A); as described in Experimental Section, the animals continued to

nitrite were eliminated. Nitrite salts are highly water-soluble, deoxygenated nitrite solutions are stable for long periods of time, and as reported here, nitrite has a reasonably high affinity for cobinamide. Moreover, we found that  $\text{Cbi}(\text{NO}_2)_4$  is well absorbed after intramuscular injection and rescues animals from cyanide poisoning. Nitrite has been used for almost a century to treat cardiovascular diseases.<sup>36–38</sup> It has two potentially toxic effects: (i) generation of methemoglobin (which is largely how it functions as a cyanide antidote, since cyanide binds to methemoglobin but methemoglobin does not bind oxygen and (ii) generation of nitric oxide (which is how it functions for treating cardiovascular diseases) but excess nitric oxide can lead to hypotension.<sup>20,21,23,36–39</sup> As calculated below, the amount of nitrite in the projected human dose of  $\text{Cbi}(\text{NO}_2)_4$  for treating cyanide poisoning would be considerably less than the amount of nitrite in Nithiodote, the approved form of nitrite used for cyanide poisoning. Furthermore, we found no evidence of methemoglobin production or hypotension in  $\text{Cbi}(\text{NO}_2)_4$ -treated rabbits. Thus, at the doses nitrite would be used, it appears to be an excellent cobinamide ligand.

We now show in both mice and rabbits that  $\text{Cbi}(\text{NO}_2)_4$  was better absorbed after intramuscular injection than  $\text{Cbi}(\text{NO}_2)_2$ . We also showed that on diluting a  $\text{Cbi}(\text{NO}_2)_4$  solution, two nitrite groups remain bound to cobinamide more effectively than on diluting a  $\text{Cbi}(\text{NO}_2)_2$  solution, and this could reduce cobinamide binding to anions in the extracellular matrix as the nitrocobinamide is diluted in the interstitial fluid. Less cobinamide binding to the extracellular matrix could potentially reduce tissue injury, and this could explain why  $\text{Cbi}(\text{NO}_2)_4$  caused less muscle inflammation and injury in mice than  $\text{Cbi}(\text{NO}_2)_2$ . With either nitrocobinamide formulation, the muscle injury reversed fully within 1 week. We should note that the amount of nitrocobinamide injected in these studies of muscle injury was 5 times the amount required to rescue animals from cyanide toxicity. Thus, nitrocobinamide may cause little muscle damage at a therapeutic dose.

Because of the small size of mice, scaling a drug dose from a mouse to a human is less likely to be accurate than scaling from a larger animal, such as a rabbit. The 4.88 mg/kg  $\text{Cbi}(\text{NO}_2)_4$  and 14.9 mg/kg sodium thiosulfate that rescued 80% of rabbits from a lethal exposure of cyanide translate to 1.57 and 4.8 mg/kg human equivalent doses of  $\text{Cbi}(\text{NO}_2)_4$  and sodium thiosulfate, respectively.<sup>40</sup> Sodium nitrite comprises 18.8% of the molecular mass of  $\text{Cbi}(\text{NO}_2)_4$ , and hence the amount of nitrite delivered to a human would be 0.29 mg/kg. This is ~15% of the amount of nitrite administered in Nithiodote (4.2 mg/kg sodium nitrite), and this small amount of nitrite likely explains the lack of efficacy of the sodium nitrite by itself. It also likely explains why we observed no methemoglobin generation or change in blood pressure by the  $\text{Cbi}(\text{NO}_2)_4$ . The 4.8 mg/kg human equivalent dose of sodium thiosulfate is also much less than the amount of sodium thiosulfate administered in Nithiodote (178 mg/kg). Thus, the amounts of sodium nitrite and sodium thiosulfate in the  $\text{Cbi}(\text{NO}_2)_4$ –thiosulfate combination that we found to be efficacious are low and well within a tolerable range.

By injection of relatively concentrated solutions of  $\text{Cbi}(\text{NO}_2)_4$  and sodium thiosulfate (200 mM and 3 M, respectively), an injection volume of 1.4 mL of each of the two solutions should rescue a human from a lethal cyanide exposure, based on the human equivalent doses of  $\text{Cbi}(\text{NO}_2)_4$  and sodium thiosulfate calculated above. The total volume of

2.8 mL could be administered by injection into the vastus lateralis muscle, a common site for intramuscular injection. We found that nitrocobinamide is stable in solution, and sodium thiosulfate is well-known to be stable. Thus, both drugs could be administered via prefilled autoinjectors, and to ensure that both drugs are administered to a patient, the autoinjectors could be bound together, with the two drugs injected simultaneously. Refinement of the  $\text{Cbi}(\text{NO}_2)_4$  and sodium thiosulfate doses and injection volumes may occur as we study larger animals, but we conclude that the combination of nitrocobinamide with thiosulfate is an effective cyanide antidote that can be administered by intramuscular injection and could therefore be used in the field to treat victims of cyanide poisoning.

A new cyanide antidote would be approved by the FDA via the “Animal Rule Pathway”, which is used when studies cannot be done ethically on humans.<sup>41</sup> Phase I safety studies of the drug are, of course, still required, but well-controlled animal efficacy studies replace standard phase II and III clinical trials. Thus, no human efficacy studies will be performed, and the studies reported here will form the basis for future animal efficacy studies.

## ■ EXPERIMENTAL SECTION

**Nomenclature.** The term “cobinamide” is used generically, without specifying the ligand(s) bound to the cobalt atom. “Aquo-hydroxocobinamide” refers to cobinamide with a water and hydroxyl group coordinated to the cobalt atom, without designating which group is in the lower ( $\alpha$ ) or upper ( $\beta$ ) axial position (Supporting Information, Figure 1). “Dicyanocobinamide” refers to cobinamide with two bound cyanide molecules, and “sulfitecobinamide” refers to cobinamide with one bound sulfite group.

Nitrite binds to cobalamin via the nitrogen atom and not via one of the two oxygen atoms.<sup>42,43</sup> Assuming the same binding mechanism occurs for cobinamide, the proper names for cobinamide with one bound nitrite group is mononitrocobinamide (in aqueous solution, the other axial ligand would be a water molecule or hydroxyl group, depending on the pH), and with two bound nitrite groups, dinitrocobinamide. As described in the Results, the number of nitrite groups bound to cobinamide is dependent on the cobinamide concentration. We therefore use the generic term “nitrocobinamide” to describe cobinamide in the presence of nitrite, without specifying whether one or two nitrites are bound; nitrocobinamide generated by adding two or four molar equivalents of sodium nitrite to cobinamide is designated  $\text{Cbi}(\text{NO}_2)_2$  and  $\text{Cbi}(\text{NO}_2)_4$ , respectively.

**Materials.** The sodium nitrite, sodium sulfite, and sodium thiosulfate were from Sigma-Aldrich and were all >99% pure. Potassium cyanide was from Fisher Chemical and was 99.4% pure. All other chemicals and reagents were of the highest grade available. The cobinamide was synthesized from hydroxocobalamin by base hydrolysis using cerium hydroxide and was >96% pure as determined by HPLC at 370 nm and by comparison to a cobinamide malate reference standard.<sup>44,45</sup> The certificates of analysis for the nitrocobinamide and cobinamide malate are provided in the Supporting Information.

**Nitrite Binding to Cobinamide.** Sodium nitrite was added to 10 and 500  $\mu\text{M}$  solutions of aquo-hydroxocobinamide to final concentrations ranging from 0.25 to 20 times the aquo-hydroxocobinamide concentration. Spectra from 300 to 600 nm were recorded on a Kontron 860 spectrophotometer. The binding affinity ( $K_a$ ) of nitrite for cobinamide was determined by plotting the difference between absorbance at 380 nm in the presence of sodium nitrite from absorbance in the absence of sodium nitrite at various nitrite concentrations using Prism 4 software (Carlsbad, CA). In some experiments, two molar equivalents of sodium cyanide were added to  $\text{Cbi}(\text{NO}_2)_4$ , and the spectrum was recorded immediately.



**Measurement of Cellular Oxygen Consumption.** Cyanide inhibits mitochondrial cytochrome *c* oxidase, and because mitochondrial respiration accounts for >90% of cellular oxygen consumption,<sup>46,47</sup> we studied the effects of cyanide on cellular oxygen consumption using an XF extracellular flux analyzer (Seahorse Bioscience). This instrument allows real-time measurement of oxygen consumption without disturbing cells and sequential addition of drugs to cells.

COS-7 monkey kidney fibroblasts were plated in 24-well XF tissue culture plates, and 24 h later the cells were washed and left in XF assay medium. After obtaining baseline readings, potassium cyanide was added to a final concentration of 1 mM, and 18 min later known cyanide antidotes were added to the cells.

**Nitrocobinamide Stability.** Solutions of Cbi(NO<sub>2</sub>)<sub>2</sub> and Cbi(NO<sub>2</sub>)<sub>4</sub> were incubated at 25 and 50 °C for 1–4 months. At various times during the incubation, samples were removed and analyzed by HPLC. Purity was determined by comparison to known standards.

**Nitrocobinamide Pharmacokinetics after Intramuscular Injection.** The total plasma cobinamide concentration was measured in New Zealand white rabbits and C57/BL/6J mice after injecting Cbi(NO<sub>2</sub>)<sub>2</sub> and Cbi(NO<sub>2</sub>)<sub>4</sub>. In the rabbits, 80 μL of 200 mM nitrocobinamide solutions were injected into the pectoral muscle of anesthetized animals, and blood was collected at various times prior to and after injection. In the mice, an amount of 50 μL of 100 mM nitrocobinamide solutions was injected into the gastrocnemius muscle, and blood was collected 5 min after injection. In both cases, a several-fold excess of potassium cyanide (over the predicted cobinamide concentration) was added to plasma to generate dicyanocobinamide, and the samples were heated at 80 °C for 15 min. Acetonitrile/methanol (90/10) was added to the samples, which were centrifuged, and the clear deproteinized supernatant was analyzed by HPLC, measuring absorption at 366 nm and comparing to dicyanocobinamide standards.

**Muscle Analysis after Intramuscular Injection of Nitrocobinamide.** C57BL/6J adult male mice were injected in the gastrocnemius muscle with 50 μL of saline, 50 μL of 80 mM Cbi(NO<sub>2</sub>)<sub>2</sub>, or 50 μL of 80 mM Cbi(NO<sub>2</sub>)<sub>4</sub>. The mice were euthanized 24 h later, and the injected muscle was harvested. Immediately following collection, muscle specimens were flash frozen in isopentane precooled in liquid nitrogen; cryosections (8 μm) were cut and stained with hematoxylin and eosin. Three injected muscles for each condition were reviewed in a blinded fashion by a veterinary pathologist, who has special expertise in muscle pathology. The pathologist used a scale of 0 to 4 to evaluate the muscle histology: 0, normal muscle; +1, minimally abnormal by evidence of some edema and few polymorphonuclear leukocytes but no muscle necrosis; +2, mildly abnormal by evidence of many polymorphonuclear leukocytes and mild muscle necrosis; +3, moderately abnormal by evidence of extensive polymorphonuclear leukocyte infiltration and moderate muscle necrosis; +4, severely abnormal by evidence of extensive muscle necrosis.

**Nitrocobinamide as a Cyanide Antidote in Mice.** We developed an inhalational model that allows mice to be exposed to cyanide gas, injected with an antidote, and then re-exposed to the gas.<sup>25</sup> We use a custom-made gas chamber and can vary the gas exposure periods: we have chosen 15 min of cyanide gas exposure, inject the animals with test antidote, and then re-expose them to cyanide for 25 min; thus, total cyanide exposure time is 40 min. This model simulates a real-life situation of people being exposed to cyanide such as in an airport or subway station, with 15 min required for emergency medical personnel to arrive and another 25 min required to treat and evacuate the victims from the cyanide-contaminated area. The mice are anesthetized fully throughout the cyanide exposure as required by our Institutional Animal Care and Use Committee (IACUC): we inject isoflurane into the chamber to a final concentration of 2%, which rapidly vaporizes and anesthetizes the mice. The cyanide gas is generated in the chamber by injecting KCN into a beaker of sulfuric acid; we have shown that the HCN concentration reaches equilibrium within 5 min of injection of the KCN and that the HCN concentration remains stable throughout the

40 min exposure period.<sup>4</sup> We used adult male C57BL/6J mice and tested Cbi(NO<sub>2</sub>)<sub>2</sub> and Cbi(NO<sub>2</sub>)<sub>4</sub> with and without sodium thiosulfate; for comparison, we tested sulfitocobinamide.

**Nitrocobinamide as a Cyanide Antidote in Rabbits.** New Zealand white rabbits weighing 3.5–4.5 kg were anesthetized with ketamine and xylazine and mechanically ventilated with room air at 20 respirations per minute and tidal volume of 50 cc. After a 10 min baseline equilibration period, intravenous sodium cyanide was started at 0.33 mg/min. When the mean arterial blood pressure (MAP, measured using an intra-arterial transducer) decreased to <70% of baseline (generally after ~30 min), the animals were injected in the pectoral muscle with either 80 μL of saline (control group) or two separate simultaneous injections of 80 μL of 200 mM Cbi(NO<sub>2</sub>)<sub>4</sub> and 80 μL of 3.0 M sodium thiosulfate (experimental group). Cyanide infusion was continued for 30 min after saline or antidote injection; animals that survived an additional 60 min after the cyanide infusion was stopped were euthanized.

Cyanide renders tissues unable to extract oxygen, resulting in direct reduction of optically active metal centers such as cytochrome *c* oxidase. The extent of cytochrome *c* oxidase reduction can be followed using diffuse optical spectroscopy with the cytochrome *c* oxidase redox state calculated as oxidized cytochrome *c* – reduced cytochrome *c* oxidase.<sup>5,6,48</sup>

**Measurement of Methemoglobin.** Oxidation of hemoglobin to methemoglobin leads to a marked increase in absorption in the red region of the visible spectrum (600–650 nm), with a strong absorption peak at 630 nm. We took advantage of this increased absorption and measured the tissue methemoglobin concentration in vivo using broadband diffuse optical spectroscopy.<sup>49</sup>

**Institutional Animal Care and Use Committee Approval.** All mouse studies were reviewed and approved by the University of California, San Diego IACUC, and all rabbit studies were reviewed and approved by the University of California, Irvine IACUC.

**Data Analysis.** All experiments were performed at least three times unless indicated otherwise. In the case of UV–visible spectra, a representative spectrum is shown, and for other data the mean value is shown. The data were plotted and analyzed using Prism 4 software.

## ■ ASSOCIATED CONTENT

### ● Supporting Information

Figures 1 and 2 showing cobinamide structures and UV–visible spectra. This material is available free of charge via the Internet at <http://pubs.acs.org>.

## ■ AUTHOR INFORMATION

### Corresponding Author

\*Telephone: 858-534-8805. Fax: 858-534-1421. E-mail: [gbooss@ucsd.edu](mailto:gbooss@ucsd.edu).

### Notes

The authors declare no competing financial interest.

## ■ ACKNOWLEDGMENTS

This work was supported by the CounterACT Program, Office of the Director, National Institutes of Health (OD) and the National Institute of Neurological Disorders and Stroke (NINDS), Grant U01 NS058030, and by United States Army Grant AMRMC W81XWH-12-2-0098. J.J. was supported by National Institute of Diabetes and Digestive and Kidney Diseases Training Grant T32DK069263. H.H.P. was supported by grants from the National Heart, Lung Blood Institute (Grant HL107200) and Veterans Administration Merit (Grant BX001963).

## ■ ABBREVIATIONS USED

Cbi(NO<sub>2</sub>)<sub>2</sub>, cobinamide with 2 equiv of sodium nitrite; Cbi(NO<sub>2</sub>)<sub>4</sub>, cobinamide with 4 equiv of sodium nitrite

## REFERENCES

- (1) Dzombak, D. A.; Ghosh, R. S.; Wong-Chong, G. M. *Cyanide in Water and Soil: Chemistry, Risk, and Management*; CRC Press: Boca Raton, FL, 2006.
- (2) Baud, F. J.; Barriot, P.; Toffis, V.; Riou, B.; Vicaut, E.; Lecarpentier, Y.; Bourdon, R.; Astier, A.; Bismuth, C. Elevated blood cyanide concentrations in victims of smoke inhalation. *N. Engl. J. Med.* **1991**, *325*, 1761–1766.
- (3) Alarie, Y. Toxicity of fire smoke. *Crit. Rev. Toxicol.* **2002**, *32*, 259–289.
- (4) Chan, A.; Balasubramanian, M.; Blackledge, W.; Mohammad, O. M.; Alvarez, L.; Boss, G. R.; Bigby, T. D. Cobinamide is superior to other treatments in a mouse model of cyanide poisoning. *Clin. Toxicol.* **2010**, *48*, 709–717.
- (5) Brenner, M.; Mahon, S. B.; Lee, J.; Kim, J.; Mukai, D.; Goodman, S.; Kreuter, K. A.; Ahdout, R.; Mohammad, O.; Sharma, V. S.; Blackledge, W.; Boss, G. R. Comparison of cobinamide to hydroxocobalamin in reversing cyanide physiologic effects in rabbits using diffuse optical spectroscopy monitoring. *J. Biomed. Opt.* **2010**, *15*, 017001.
- (6) Brenner, M.; Kim, J. G.; Mahon, S. B.; Lee, J.; Kreuter, K. A.; Blackledge, W.; Mukai, D.; Patterson, S.; Mohammad, O.; Sharma, V. S.; Boss, G. R. Intramuscular cobinamide sulfite in a rabbit model of sublethal cyanide toxicity. *Ann. Emerg. Med.* **2009**, *55*, 352–362.
- (7) Bebart, V.; Tanen, D.; Boudrea, S.; Castaneda, M.; Zarzabal, L.; Vargas, T.; Boss, G. Intravenous cobinamide versus hydroxocobalamin for acute treatment of severe cyanide poisoning in a swine (Sus Scroba) model. *Ann. Emerg. Med.* **2014**, *64*, 612–619.
- (8) Chen, K. K.; Rose, C. L. Nitrite and thiosulfate therapy in cyanide poisoning. *JAMA, J. Am. Med. Assoc.* **1952**, *149*, 113–119.
- (9) Frankenberg, L.; Sorbo, B. Effect of cyanide antidotes on the metabolic conversion of cyanide to thiocyanate. *Arch. Toxicol.* **1975**, *33*, 81–89.
- (10) Schwartz, C.; Morgan, R. L.; Way, L. M.; Way, J. L. Antagonism of cyanide intoxication with sodium pyruvate. *Toxicol. Appl. Pharmacol.* **1979**, *50*, 437–441.
- (11) Way, J. L.; Burrows, G. Cyanide intoxication: protection with chlorpromazine. *Toxicol. Appl. Pharmacol.* **1976**, *36*, 93–97.
- (12) Hall, A. H.; Rumack, B. H. Hydroxycobalamin/sodium thiosulfate as a cyanide antidote. *J. Emerg. Med.* **1987**, *5*, 115–121.
- (13) Isom, G.; Way, J. L. Cyanide intoxication: protection with cobaltous chloride. *Toxicol. Appl. Pharmacol.* **1973**, *24*, 449–456.
- (14) Firth, R. A.; Hill, H. A. O.; Pratt, J. M.; Thorp, R. G.; Williams, R. J. P. The chemistry of vitamin B<sub>12</sub>. Part XI. Some further formation constants. *J. Chem. Soc. A* **1969**, 381–386.
- (15) Hayward, G. C.; Hill, H. A. O.; Pratt, J. M.; Vanston, N. J.; Williams, A. R. W. The chemistry of vitamin B(12). Part IV.1 The thermodynamic trans-effect. *J. Chem. Soc.* **1965**, 6485–6493.
- (16) Ma, J.; Dasgupta, P. K.; Zelder, F. H.; Boss, G. R. Cobinamide chemistries for photometric cyanide determination. A merging zone liquid core waveguide cyanide analyzer using cyanoaquacobinamide. *Anal. Chim. Acta* **2012**, *736*, 78–84.
- (17) Ma, J.; Dasgupta, P. K.; Blackledge, W.; Boss, G. R. Temperature dependence of Henry's law constant for hydrogen cyanide. Generation of trace standard gaseous hydrogen cyanide. *Environ. Sci. Technol.* **2010**, *44*, 3028–3034.
- (18) Pearce, L. L.; Bominaar, E. L.; Hill, B. C.; Peterson, J. Reversal of cyanide inhibition of cytochrome c oxidase by the auxiliary substrate nitric oxide: an endogenous antidote to cyanide poisoning? *J. Biol. Chem.* **2003**, *278*, 52139–52145.
- (19) Leavesley, H. B.; Li, L.; Prabhakaran, K.; Borowitz, J. L.; Isom, G. E. Interaction of cyanide and nitric oxide with cytochrome c oxidase: implications for acute cyanide toxicity. *Toxicol. Sci.* **2008**, *101*, 101–111.
- (20) Feelisch, M.; Fernandez, B. O.; Bryan, N. S.; Garcia-Saura, M. F.; Bauer, S.; Whitlock, D. R.; Ford, P. C.; Janero, D. R.; Rodriguez, J.; Ashrafi, H. Tissue processing of nitrite in hypoxia: an intricate interplay of nitric oxide-generating and -scavenging systems. *J. Biol. Chem.* **2008**, *283*, 33927–33934.
- (21) Li, H.; Kundu, T. K.; Zweier, J. L. Characterization of the magnitude and mechanism of aldehyde oxidase-mediated nitric oxide production from nitrite. *J. Biol. Chem.* **2009**, *284*, 33850–33858.
- (22) Sorbo, B. H. Crystalline rhodanese. II. The enzyme catalysed reaction. *Acta Chem. Scand.* **1953**, *7*, 1137–1143.
- (23) Way, J. L. Cyanide intoxication and its mechanism of antagonism. *Annu. Rev. Pharmacol. Toxicol.* **1984**, *24*, 451–481.
- (24) Socarras, S.; Magari, R. T. Modeling the effects of storage temperature excursions on shelf life. *J. Pharm. Biomed. Anal.* **2009**, *49*, 221–226.
- (25) Chan, A.; Crankshaw, D. L.; Monteil, A.; Patterson, S. E.; Nagasawa, H. T.; Briggs, J. E.; Kozocas, J. A.; Mahon, S. B.; Brenner, M.; Pilz, R. B.; Bigby, T. D.; Boss, G. R. The combination of cobinamide and sulfanegen is highly effective in mouse models of cyanide poisoning. *Clin. Toxicol.* **2011**, *49*, 366–373.
- (26) Kim, J. C.; Lee, J.; Mahon, S. B.; Mukai, D.; Patterson, S. E.; Boss, G. R.; Tromberg, B. J.; Brenner, M. Noninvasive monitoring of treatment response in a rabbit cyanide toxicity model reveals differences in brain and muscle metabolism. *J. Biomed. Opt.* **2012**, *17*, 105005.
- (27) Okolie, N. P.; Iroanya, C. U. Some histologic and biochemical evidence for mitigation of cyanide-induced tissue lesions by antioxidant vitamin administration in rabbits. *Food Chem. Toxicol.* **2003**, *41*, 463–469.
- (28) Rodgers, G. C., Jr.; Condurache, C. T. Antidotes and treatments for chemical warfare/terrorism agents: an evidence-based review. *Clin. Pharmacol. Ther.* **2010**, *88*, 318–327.
- (29) Watanabe, K.; Kitagishi, H.; Kano, K. Supramolecular ferric porphyrins as cyanide receptors in aqueous solution. *ACS Med. Chem. Lett.* **2011**, *2*, 943–947.
- (30) Hatch, R. C.; Laflamme, D. P.; Jain, A. V. Effects of various known and potential cyanide antagonists and a glutathione depletor on acute toxicity of cyanide in mice. *Vet. Hum. Toxicol.* **1990**, *32*, 9–16.
- (31) Reiter, R. J.; Paredes, S. D.; Korkmaz, A.; Jou, M. J.; Tan, D. X. Melatonin combats molecular terrorism at the mitochondrial level. *Interdiscip. Toxicol.* **2008**, *1*, 137–149.
- (32) Maduh, E. U.; Johnson, J. D.; Ardelt, B. K.; Borowitz, J. L.; Isom, G. E. Cyanide-induced neurotoxicity: mechanisms of attenuation by chlorpromazine. *Toxicol. Appl. Pharmacol.* **1988**, *96*, 60–67.
- (33) Bhattacharya, R.; Tulsawani, R. In vitro and in vivo evaluation of various carbonyl compounds against cyanide toxicity with particular reference to alpha-ketoglutaric acid. *Drug Chem. Toxicol.* **2008**, *31*, 149–161.
- (34) Nath, A. K.; Roberts, L. D.; Liu, Y.; Mahon, S. B.; Kim, S.; Ryu, J. H.; Werdich, A.; Januzzi, J. L.; Boss, G. R.; Rockwood, G. A.; MacRae, C. A.; Brenner, M.; Gerszten, R. E.; Peterson, R. T. Chemical and metabolomic screens identify novel biomarkers and antidotes for cyanide exposure. *FASEB J.* **2013**, *27*, 1928–1938.
- (35) Lavon, O.; Bentur, Y. Does amyl nitrite have a role in the management of pre-hospital mass casualty cyanide poisoning? *Clin. Toxicol.* **2010**, *48*, 477–484.
- (36) Dejam, A.; Hunter, C. J.; Tremonti, C.; Pluta, R. M.; Hon, Y. Y.; Grimes, G.; Partovi, K.; Pelletier, M. M.; Oldfield, E. H.; Cannon, R. O., III; Schechter, A. N.; Gladwin, M. T. Nitrite infusion in humans and nonhuman primates: endocrine effects, pharmacokinetics, and tolerance formation. *Circulation* **2007**, *116*, 1821–1831.
- (37) Alef, M. J.; Tzeng, E.; Zuckerbraun, B. S. Nitric oxide and nitrite-based therapeutic opportunities in intimal hyperplasia. *Nitric Oxide* **2012**, *26*, 285–294.
- (38) Nossaman, V. E.; Nossaman, B. D.; Kadowitz, P. J. Nitrates and nitrites in the treatment of ischemic cardiac disease. *Cardiol. Rev.* **2010**, *18*, 190–197.
- (39) Gracia, R.; Shepherd, G. Cyanide poisoning and its treatment. *Pharmacotherapy* **2004**, *24*, 1358–1365.
- (40) U.S. Department of Health and Human Services, Food and Drug Administration, Center for Drug Evaluation and Research (CDER). *Guidance for Industry: Estimating the Maximum Safe Starting Dose in Initial Clinical Trials for Therapeutics in Adult Healthy*

Volunteers; Office of Training and Communications, Food and Drug Administration: Rockville, MD, 2005; pp 1–27.

(41) U.S. Department of Health and Human Services, Food and Drug Administration, Center for Drug Evaluation and Research (CDER); Center for Biologics Evaluation and Research (CBER). *Guidance for Industry: Product Development under the Animal Rule*; Office of Communication, Food and Drug Administration: Silver Spring, MD, 2014; pp 1–48.

(42) Perry, C. B.; Fernandes, M. A.; Brown, K. L.; Zou, X.; Valente, E. J.; Marques, H. M. Probing the nature of the Co<sup>III</sup> ion in cobalamins—spectroscopic and structural investigations of the reactions of aquacobalamin (vitamin B<sub>12</sub>) with ambident nucleophiles. *Eur. J. Inorg. Chem.* **2003**, 2095–2107.

(43) Garau, G.; Geremia, C.; Marzilli, R. G.; Randaccio, L.; Tauzher, J. Crystal chemistry and binding of NO<sub>2</sub>, SCN and SeCN to Co in cobalamins. *Acta Crystallogr.* **2003**, 859, 51–59.

(44) Renz, P. Some intermediates in the biosynthesis of vitamin B<sub>12</sub>. *Methods Enzymol.* **1971**, 18c, 82–86.

(45) Broderick, K. E.; Singh, V.; Zhuang, S.; Kambo, A.; Chen, J. C.; Sharma, V. S.; Pilz, R. B.; Boss, G. R. Nitric oxide scavenging by the cobalamin precursor cobinamide. *J. Biol. Chem.* **2005**, 280, 8678–8685.

(46) van Buuren, K. J.; Nicholis, P.; van Gelder, B. F. Biochemical and biophysical studies on cytochrome aa 3. VI. Reaction of cyanide with oxidized and reduced enzyme. *Biochim. Biophys. Acta* **1972**, 256, 258–276.

(47) Babcock, G. T.; Wikstrom, M. Oxygen activation and the conservation of energy in cell respiration. *Nature* **1992**, 356, 301–309.

(48) Lee, J.; Kim, J. G.; Mahon, S. B.; Mukai, D.; Yoon, D.; Boss, G. R.; Patterson, S. E.; Rockwood, G.; Isom, G.; Brenner, M. Noninvasive optical cytochrome c oxidase redox state measurements using diffuse optical spectroscopy. *J. Biomed. Opt.* **2014**, 19, 055001.

(49) Lee, J.; El-Abaddi, N.; Duke, A.; Cerussi, A. E.; Brenner, M.; Tromberg, B. J. Noninvasive in vivo monitoring of methemoglobin formation and reduction with broadband diffuse optical spectroscopy. *J. Appl. Physiol.* **2006**, 100, 615–622.

# Hand-Held High-Throughput Ultrasonic Monodisperse Aerosol Inhalers for Detoxification of Massive Cyanide Poisoning

Chen S. Tsai\*, Rong W. Mao, Yun Zhu, Eric Chien,  
James Maduzia

University of California, Irvine  
Dept. of Electrical Eng. and Comp. Science  
Irvine, CA 92697, USA  
\*e-mail: cstsai@uci.edu

Shirley C. Tsai  
Dept. of Chem. Eng. and Materials Science  
University of California, Irvine

Matthew Brenner, Sari Mahon, David Mukai,  
Jangwoon Lee, David Yoon, Tanya Berney

University of California, Irvine  
Division of Pulmonary and Critical Care Medicine  
Beckman Laser Institute and Medical Clinics  
Irvine, CA 92612 USA

Gerry Boss  
Department of Medicine, Univ. of California, San Diego  
La Jolla, CA 92093  
Steve Patterson  
Dept. of Pharmacology and Center for Drug Design, Univ.  
of Minnesota, Minneapolis, MN 55455

**Abstract**— Detoxification of massive cyanide (CN) poisoning by inhalation of antidotes is recognized to be superior to intravenous (IV) or intra muscular (IM) treatment with regard to ease of administration, self-administration, and rapidity of onset. However, there are currently no effective, portable, high-throughput inhalers that can be produced in large quantities and distributed for such purpose. A hand-held inhaler has been realized using silicon-based ultrasonic nozzle to produce high-throughput of monodisperse cobinamide antidote solution for detoxification of CN poisoning in a rabbit model.

**Keywords**- cyanide poisoning and detoxification, cobinamide antidote, Fourier-horn ultrasonic nozzles, monodisperse aerosol inhaler

## I. INTRODUCTION

Currently, all effective cyanide (CN) antidotes must be administered intravenously (IV). This is not possible for mass CN poisoning resulting from disasters such as terrorist attack and major fires. There is currently no available intramuscular (IM) treatment or agents that can be applied rapidly for the mass CN poisoning either. Meanwhile, inhalation modes may be superior with regard to ease of administration, self-administration, and rapidity of onset. However, current commercial inhalers or nebulizers all suffer from polydisperse (broad-size) aerosol distribution and/or low throughput, making it difficult to deliver sufficient amount of drugs to the lung rapidly and precisely. Thus, there is no effective portable, high-throughput, low-power inhalers that can be produced in large quantities and distributed for such purposes.

Aerosol particles (or droplets) greater than  $5\mu\text{m}$  in mass median aerodynamic diameter (MMAD) or mass median diameter (MMD) impact primarily in the oropharynx and thus do not enter the respiratory system. Particles between  $5$  and  $1\mu\text{m}$  (the “respirable” fraction) enter the respiratory system [1,

2] and deposit in progressively smaller airways [2]. Particles between  $3$  and  $1\mu\text{m}$  deposit optimally in the alveolar region [3-5], while particles smaller than  $1\mu\text{m}$  remain airborne and are exhaled. Droplet size distribution, as measured by geometrical standard deviation (GSD), is also an important determinant of inhaled drug delivery. Human deposition images from the same patient inhaling from two different wet nebulizers both with MMAD below  $5\mu\text{m}$  but with different size distributions (GSD  $>4.0$  versus  $3.0$ - $4.0$ ) illustrate how small changes in the polydispersity or GSD of the aerosol distributions result in markedly different deposition patterns [6, 7].

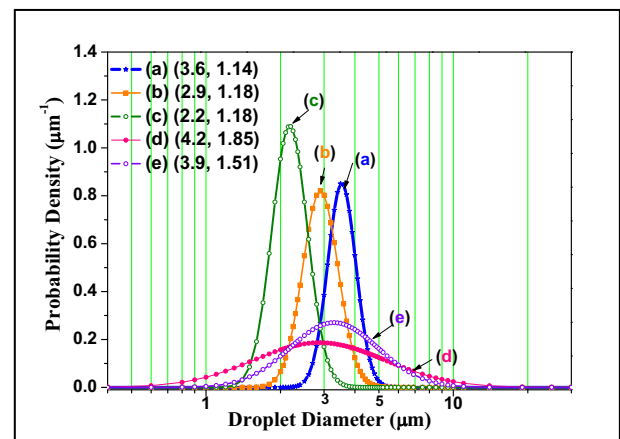


**Fig. 1** (a) 1.5 MHz nozzle with water ( $3.6\mu\text{m}/1.14$ ), (b) 2.0 MHz nozzle with water ( $2.9\mu\text{m}/1.18$ ), (c) 2.0 MHz nozzle with alcohol ( $2.2\mu\text{m}/1.18$ ), and commercial nebulizers (d) Omron NE-U22V ( $4.2\mu\text{m}/1.85$ ) and (e) Pari eFlow ( $3.9\mu\text{m}/1.51$ ). Note: Numbers in parenthesis designate NMD and GSD which stand for number mean diameter and geometrical standard deviation, respectively.

As shown in Fig. 1 plots (d) and (e), even the most advanced vibrating mesh technology-based ultrasonic



nebulizers produced very broad drop-size distributions. In contrast, the MHz multiple-Fourier horn ultrasonic nozzle reported recently [8-10] has demonstrated its capability of producing high-throughput micrometer-sized monodisperse droplets (see plots (a) to (c) of Fig. 1) at very low electrical drive power and thus fulfilling the unmet needs. This paper reports utilization of a hand-held inhaler with 1.5 MHz 4-Fourier horn nozzle to produce high-throughput of aerosolized monodisperse cobinamide antidote solution for detoxification of CN poisoning in a rabbit model.

## II. SILICON-BASED ULTRASONIC NOZZLE

Figure 2(a) shows the silicon-based multiple-Fourier horn ultrasonic nozzle that enables controlled excitation of single-mode MHz Faraday waves and production of micrometer-sized monodisperse droplets from the nozzle end face. Fig. 2(b) shows photographs of the 1.5 MHz four-Fourier horn nozzle used in this study. The nozzle was designed to vibrate in a single longitudinal vibration mode at the single resonance frequency ( $f$ ) of the multiple-Fourier horns [8]. Electrical activation of the PZT transducers at this resonance frequency creates a standing acoustic wave through the nozzle body in the direction perpendicular to the nozzle end face [Z-axis in Figs. 2(a) and 2(c)] with a maximum vibration displacement ( $h$ ) on the end face. The greatly enhanced  $h$  due to the multiple-Fourier horns in resonance (with a displacement gain of  $2^n$  for a  $n$ -Fourier-horn nozzle) [8, 9] facilitates the critical excitation displacement ( $h_{cr}$ ) required to form Faraday waves on the free surface of the planar liquid layer resting on the nozzle end face and, subsequently, initiates temporal instability of the waves, resulting in the ejection of monodisperse droplets at low electrical drive power. Specifically, high-throughput of aerosolized micrometer-sized monodisperse cobinamide antidote solution was produced for the CN detoxification experiments.

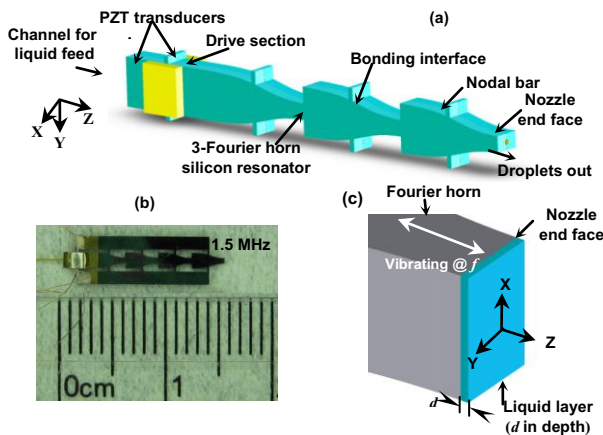


**Fig. 2** (a) MHz silicon ultrasonic nozzle with central channel dimensions of  $150\mu\text{m} \times 150\mu\text{m}$  for 1.5 MHz four-Fourier horn nozzle, and the corresponding end face dimensions of  $482\mu\text{m} \times 1060\mu\text{m}$ . (b) Photograph of the 1.5 MHz nozzle; (c) Geometry of nozzle end face and liquid layer  $d$  in depth.

## III. CYANIDE DETOXIFICATION EXPERIMENTS WITH RABBITS

We proceeded with the animal experiments using the 1.5 MHz nozzle just described with relatively low throughput (0.15 ml/min) of cobinamide antidote (100 mM or  $\sim 100$  mg in saline solution) [11-13]. Four rabbits were studied using CN infusion continuously for 60 min as shown in Fig. 3. Nebulized cobinamide was administered beginning 40 min into the CN infusion and continuing for 10 min. As is evident from Fig. 4, the rate deterioration and tissue oxygen extraction defect was immediately stabilized as the nebulization started. The process was further reversed after the CN infusion was discontinued at 60 min. Cobinamide was readily seen in the plasma samples drawn serially following initiation of the cobinamide nebulization (Fig. 5). These results clearly show the significant effect of nebulized cobinamide for reversing CN poisoning even at low dose ( $\sim 100$  mg) and thus, demonstrate the high potential of the hand-held high-throughput ultrasonic monodisperse aerosol inhalers for detoxification of massive CN poisoning.

## IV. CONCLUSIONS

Significant effect of aerosolized cobinamide for reversing CN poisoning even at low dose ( $\sim 100$  mg) has demonstrated the high potential of a hand-held MHz ultrasonic monodisperse aerosol inhaler for detoxification of massive CN poisoning. Furthermore, the micrometer-sized (2.2 to  $4.6\mu\text{m}$ ) monodisperse aerosols produced at high throughput and very low electrical drive power ( $<1.0$  W) will have broad applications to delivery of both inhalation solution and suspension drugs to the lung.

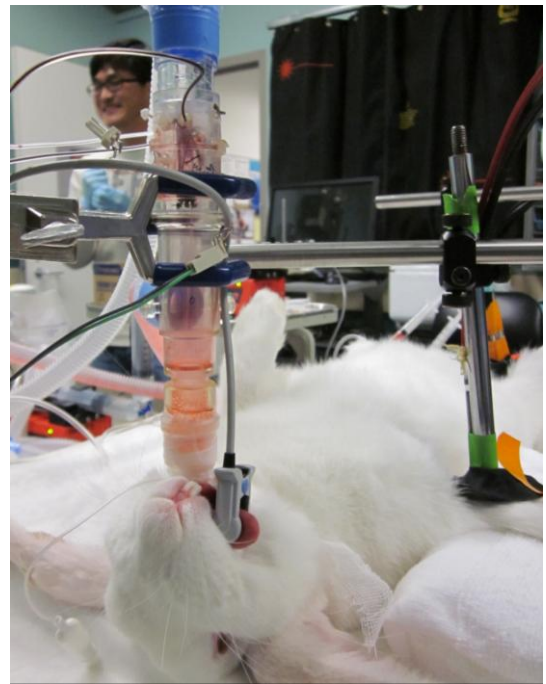


**Fig. 3** Rabbit Model Experiment



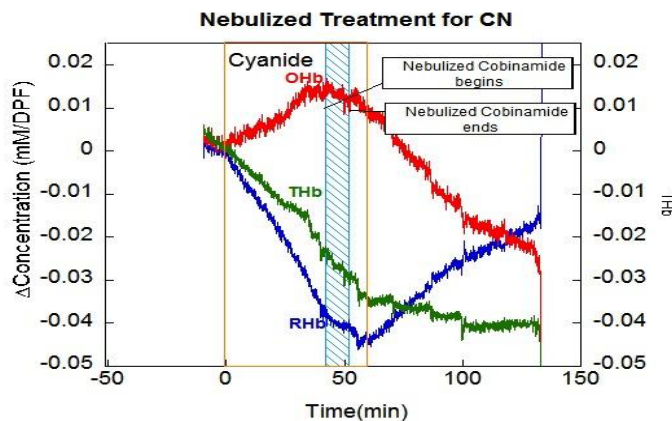


**Fig. 4** Diffuse optical spectroscopy (DOS) measurements of oxyhemoglobin (OHb) and deoxyhemoglobin (RHb) during induction of cyanide poisoning and reversal using monodisperse aerosol cobinamide administration. OHb increases during cyanide poisoning due to inability of tissue to extract oxygen. As antidote drug is absorbed, OHb returns to normal rapidly.

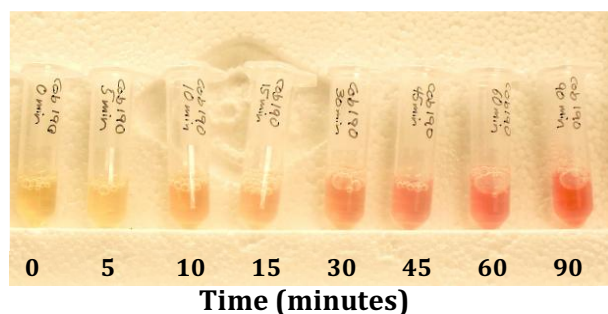


**Fig. 5** Appearance of active drug, cobinamide, in the plasma of rabbits following trans-pulmonary drug administration. In other words, cobinamide is seen as CN toxicity has been reversed with aerosol administration

#### ACKNOWLEDGMENT

This work was supported jointly by Grants 5R21-EB006366, U54-NS063718, and Counter ACT Program U01-NS058030 of National Institute of Health (NIH), USA.

#### REFERENCES

- [1] W. H. Finlay and A. R. Martin, "Recent advances in predictive understanding of respiratory tract deposition," *J Aerosol Med Pulm D*, vol. 21, pp. 189-205, Jun 2008.
- [2] J. Heyder, "Deposition of inhaled particles in the human respiratory tract and consequences for regional targeting in respiratory drug delivery," *Proc. Am. Thorac. Soc.*, vol. 1, pp. 315-20, 2004.
- [3] J. S. Patton and P. R. Byron, "Inhaling medicines: delivering drugs to the body through the lungs," *Nat. Rev. Drug Discovery*, vol. 6, pp. 67-74, Jan 2007.
- [4] J. Heyder, J. Gebhart, G. Rudolf, C. F. Schiller, and W. Stahlhofen, "Deposition of Particles in the Human Respiratory-Tract in the Size Range 0.005-15  $\mu$ m," *J. Aerosol Sci*, vol. 17, pp. 811-825, Oct 1986.
- [5] P. R. Byron, "Prediction of drug residence times in regions of the human respiratory tract following aerosol inhalation," *J. Pharm. Sci.*, vol. 75, pp. 433-8, May 1986.
- [6] S. Sangwan, R. Condos, and G. C. Smaldone, "Lung deposition and respirable mass during wet nebulization," *J. Aerosol. Med.*, vol. 16, pp. 379-386, Win 2003.
- [7] M. Solomita and G. C. Smaldone, "Reconciliation of Cascade Impaction during Wet Nebulization," *J. of Aerosol Medicine and Pulmonary Drug Delivery*, vol. 22, pp. 11-18, Mar 2009.

- [8] S. C. Tsai, Y. L. Song, T. K. Tseng, Y. F. Chou, W. J. Chen, and C. S. Tsai, "High-frequency silicon-based ultrasonic nozzles using multiple Fourier horns," *IEEE Trans. Ultrason. Ferroelectr. Freq. Control*, vol. 51, pp. 277-285, Mar 2004.
- [9] S. C. Tsai, C. H. Cheng, N. Wang, Y. L. Song, C. T. Lee, and C. S. Tsai, "Silicon-based Megahertz ultrasonic nozzles for production of monodisperse micrometer-sized droplets," *IEEE Trans. Ultrason. Ferroelectr. Freq. Control*, vol. 56, pp. 1968-1979, 2009.
- [10] C. S. Tsai, R. W. Mao, S. K. Lin, N. Wang, and S. C. Tsai, "Miniaturized multiple Fourier-horn ultrasonic droplet generators for biomedical applications," *Lab. Chip*, vol. 10, DOI: 10.1039/c005262k, pp. 2733-2740, 2010.
- [11] K. E. Broderick, P. Potluri, S. Zhuang, I. E. Scheffler, V. S. Sharma, R. B. Pilz, and G. R. Boss, "Cyanide detoxification by the cobalamin precursor cobinamide," *Exp Biol Med (Maywood)*, vol. 231, pp. 641-649, May 2006.
- [12] K. A. Kreuter, J. Lee, S. B. Mahon, J. G. Kim, D. Mukai, O. Mohammad, W. Blackledge, G. R. Boss, B. J. Tromberg, and M. Brenner, "Rapid reversal of cyanide toxicity using a novel agent, cobinamide, assessed non-invasively using diffuse optical spectroscopy," *Chest*, vol. 134, pp. 124001, 2008.
- [13] M. Brenner, J. G. Kim, S. B. Mahon, J. Lee, K. A. Kreuter, W. Blackledge, D. Mukai, S. Patterson, O. Mohammad, V. S. Sharma, and G. R. Boss, "Intramuscular cobinamide sulfite in a rabbit model of sublethal cyanide toxicity," *Ann. Emerg. Med.*, vol. 55, pp. 352-363, Apr 2010.

# Pocket-Sized Ultrasonic Nebulizer For Inhalation Drug Delivery

C.S. Tsai<sup>1,2†</sup>, R.W. Mao<sup>1</sup>, S.K. Lin<sup>1</sup>, Y. Zhu<sup>1</sup>, S.C. Tsai<sup>3</sup>

<sup>1</sup> Dept. of Elec. Eng. and Comp. Science  
University of California, Irvine, CA 92697, USA

<sup>†</sup> E-mail: cstsai@uci.edu

<sup>2</sup> Inst. of Optoelectronics and Photonics, National Taiwan University, Taipei, TAIWAN

M. Brenner<sup>4,5</sup>, S. Mahon<sup>5</sup>, D. Mukai<sup>5</sup>, and G. Boss<sup>6</sup>

<sup>3</sup> Dept. of Chem. Eng. and Materials Science

<sup>4</sup> Division of Pulmonary and Critical Care Medicine

<sup>5</sup> Beckman Laser Institute and Medical Clinics

University of California, Irvine, CA 92697, USA

<sup>6</sup> Dept. of Medicine, Univ. of California, San Diego  
La Jolla, CA 92093, USA

**Abstract**—Silicon-based MHz ultrasonic multiple Fourier horns in resonance are capable of producing high-throughput micrometer-sized droplets at low drive power. The centimeter-sized nozzles together with low power requirement enabled most recent realization of the first pocket-sized ultrasonic nebulizer (8.6 x 5.6 x 1.5 cm<sup>3</sup>) that contains nozzle, IC electronic driver, cell-phone battery, micro pump, drug reservoir, and liquid feed. A variety of common drugs for asthma, chronic obstructive pulmonary disease (COPD), diabetics, cyanide poisoning, pulmonary fibrosis, etc. such as albuterol, Humulin U-100, cobinamide, interferon- $\gamma$ , and budesonide suspension have been nebulized with desirable aerosol size and throughput.

**Keywords**— MEMS; Fourier-horn Nozzle; Pocket-Sized Ultrasonic Nebulizer; Inhalation Drug Delivery; Aerosol

## I. INTRODUCTION

Droplet generation has continued to be an area of broad interest with many applications [1, 2] among which is inhalation (pulmonary) drug delivery. Inhalation is a vitally important route for non-invasive drug delivery for both systemic and local applications [3]. Control of aerosol (particles or droplets in air) size to the optimum range (2 to 5  $\mu$ m) and throughput plays a critical role in the efficient and effective delivery of inhaled medications to the lung. Current commercial devices are metered dose inhalers (MDI), dry powder inhalers (DPI), and wet nebulizers. All these devices suffer from broad particle size (polydisperse) distributions (with large geometrical standard deviation GSD >1.5) and relatively low throughput (0.16 to 0.42 ml/min), making it difficult to deliver often expensive drug of desirable particle sizes and sufficient amount to targeted sites precisely and rapidly. The silicon-based MHz multiple-Fourier horn ultrasonic nozzle we reported recently [1, 2] has demonstrated capability of producing high-throughput micrometer-sized monodisperse droplets at low drive power and, thus, fulfilling the unmet needs, e.g., detoxification of cyanide poisoning [4, 5]. Here we report realization of the first pocket-sized ultrasonic nebulizer for inhalation drug delivery using such nozzles.

## II. NOZZLE ARCHITECTURE AND WORKING PRINCIPLE

Each basic nozzle consists of a drive section and a resonator section (Fig. 1a). A lead zirconate titanate (PZT)

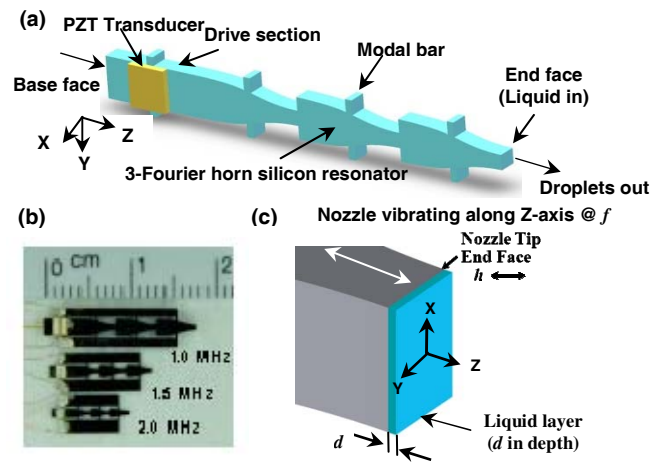


**Fig. 1**(a) 3-D architecture of the MHz multiple-Fourier horn ultrasonic nozzle; (b) Photograph of the 1.0 MHz and 1.5 MHz nozzles; (c) Geometry of nozzle endface and liquid layer  $d$  in depth.

piezoelectric transducer is bonded on the drive section to excite mechanical vibrations along the nozzle axis. The resonator section is made of multiple (3 in the example) Fourier horns in cascade [6]. The nozzle is designed to vibrate in a single longitudinal mode (along the nozzle axis) at the resonance frequency of the three Fourier horns. The liquid to be atomized is externally transported to the nozzle end face using a fused silica tube. The resonance effect greatly enhances the vibration displacement of the nozzle endface (by a factor of 8) and, hence, readily facilitates generation and subsequent temporal instability of Faraday waves on the liquid layer resting on the nozzle end face. Droplets are ejected from the liquid surface when the vibration displacement of the nozzle end face exceeds the onset threshold. Importantly, the single vibration mode at the single resonance frequency ensures single-mode Faraday wave excitation and amplification and, thus, production of monodisperse droplets at very low electrical drive power [2].

This is in stark contrast to all other ultrasonic devices that simultaneously involve various atomization mechanisms such as cavitation, impinging, and jetting in addition to capillary wave mechanism [7-9]. These various atomization mechanisms require much higher electrical drive power (by 2 to 3 orders of magnitude) and produce broad droplet size distribution. The significance of such low drive power (due to resonance) for the proposed device should be emphasized because it will eliminate the temperature rises that may damage the medications to be aerosolized.

### III. NOZZLE PERFORMANCE AND COMPARISON TO COMMERCIAL DEVICES

Nebulization (atomization) of water or medicine is carried out by applying a voltage at MHz resonance frequency across the PZT transducer and the liquid to be nebulized transported upon the nozzle end face via a fused silica tube. Droplets are ejected from the liquid free surface when the vibration displacement of the nozzle end face exceeds the onset threshold. Fig. 2 shows the measured size distributions of the droplets produced by atomization with the 1.0, 1.5 and 2.0 MHz nozzles (plots (a), (b), (c), and (d)). The corresponding geometric standard deviations (GSD) of the droplets are shown to be as small as 1.18, 1.16, 1.18, and 1.18, respectively. Note that GSD of 1.0 corresponds to single size and that an aerosol with GSD up to 1.22 is commonly accepted as monodisperse in aerosol medicine [10]. For comparison, the size distributions of polydisperse droplets with GSDs of 1.85 (Omron published data sheet) and 1.51 [11] generated by two most advanced commercial nebulizers, Omron NE-U22V and Pari e-Flow, are also shown in Fig. 2, plots (e) and (f), respectively. In Fig. 2, MMD and MMAD stand for mass median diameter and mass median aerodynamic diameter, respectively. MMD was obtained in ambient air using the Malvern/Spraytec System while MMAD was obtained in the presence of high-velocity air (15-30L/min) using a commercial cascade impactor for plots (e) and (f). Generally speaking, MMAD is significantly smaller than MMD for aqueous aerosols.

The throughput of such commercial devices ranges from 160 to 420  $\mu\text{L}/\text{min}$ , but with very broad droplet size distributions as described. The Pari e-Flow, which utilizes vibrating mesh technology, is capable of high throughput but suffers from broad droplet size distribution ( $\text{GSD} > 1.5$ ) and clogging of the orifices that are considerably smaller in diameter than the droplets produced [12]. Clearly, the size distribution of the droplets produced by the ultrasonic nozzles is much narrower than that produced by the current commercial devices. Furthermore, since no mesh is used, the new device is less prone to clogging that severely impacts on the reliability and robustness of commercial devices.

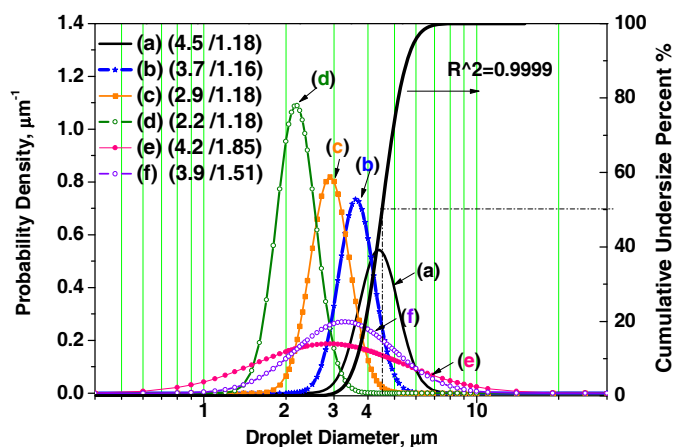


Fig. 2 Comparison of measured droplet sizes and size distributions in logarithmic scale (with MMD/GSD in parentheses for (a) to (d), and MMAD/GSD for (e) and (f)) among: (a) 1.0 MHz nozzle with a central channel for water (4.5  $\mu\text{m}/1.18$ ), (b) 1.5 MHz nozzle with water (3.7  $\mu\text{m}/1.16$ ), (c) 2.0 MHz nozzle with water (2.9  $\mu\text{m}/1.18$ ), (d) 2.0 MHz nozzle with alcohol (2.2  $\mu\text{m}/1.18$ ), (e) Omron NE-U22V (4.2  $\mu\text{m}/1.85$ ), and (f) Pari e-Flow (3.9  $\mu\text{m}/1.51$ ).

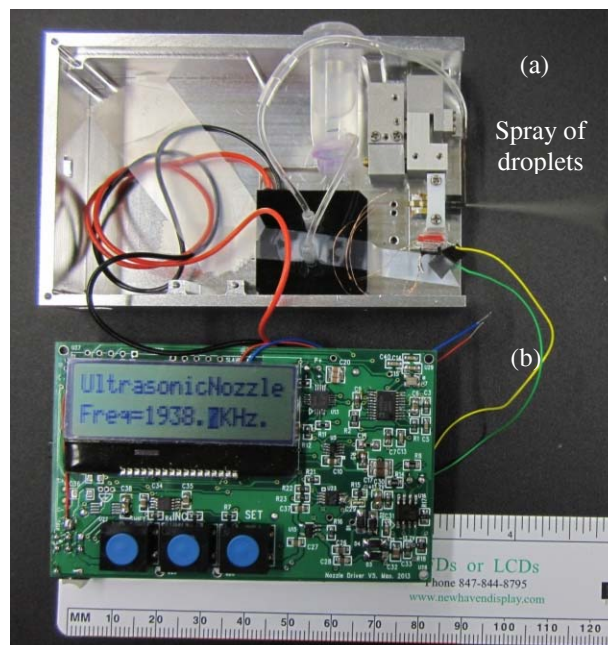


Fig. 3 MEMS-based pocket-size ultrasonic nebulizer (8.8 cm x 5.9 cm x 1.9 cm): (a) Mechanical components layout; (b) Battery-powered electronic driver

### IV. POCKET-SIZE ULTRASONIC NEBULIZER AND NEBULIZATION OF COMMON DRUGS

#### A. Pocket-Sized Nebulizer

Monodisperse medicinal aerosols of diameter range 2.2 to 4.6  $\mu\text{m}$  have been produced at throughput as high as 200  $\mu\text{L}/\text{min}$  and electrical drive power as low as 0.3 watt. The centimeter-sized nozzles together with low power requirement enabled most recent realization of the first pocket-sized ultrasonic nebulizer (8.6 x 5.6 x 1.5  $\text{cm}^3$ ) as shown in Fig. 3. The

nebulizer contains nozzle, IC electronic driver, cell-phone battery, micro pump, drug reservoir, and liquid feed.

### B. Nebulization of common Drugs

A variety of common drugs for asthma, chronic obstructive pulmonary disease (COPD), diabetes, pulmonary fibrosis, cyanide poisoning, etc. such as albuterol (isoproterenol), Humulin U-100, cobinamide, interferon- $\gamma$  [13] and budesonide suspension [14] have been nebulized using either the bench-scale unit [2] or the pocket-size nebulizer with desirable aerosol size and output rate as summarized in Table I. It is to be noted that the demonstrated moderate output rate of 100 – 150 $\mu$ l/min by the pocket-sized nebulizer would provide a higher effective dosage over the current commercial nebulizers in light of the higher aerosol monodispersity produced by the former.

### V. CONCLUDING REMARKS

A low-power, mesh-less pocket-sized ultrasonic nebulizer has been realized for the first time. The core of the nebulizer is the MEMS-based multiple-Fourier horn nozzle. The nebulizer is based on temporal instability of Faraday waves generated on the surface of medicine liquid resting on the nozzle end face. No mesh with micrometer-sized holes is used as in the commercial ultrasonic nebulizers based on the advanced vibrating mesh technology. Therefore, this new-type of ultrasonic nebulizer is less prone to clogging.

In addition, the external liquid feed offers advantage of easy control of on-off liquid flow to facilitate breath-actuation in inhalation drug delivery. The output can be increased by increasing the area of the nozzle end face and/or array of nozzles packed together sharing a single liquid feed system.

### REFERENCES

[1] S. C. Tsai, C. H. Cheng, N. Wang, Y. L. Song, C. T. Lee, and C. S. Tsai, "Silicon-based Megahertz ultrasonic nozzles for production of monodisperse micrometer-sized droplets," *IEEE Trans. Ultrason. Ferroelect. Freq. Control*, vol. 56, pp. 1968-1979, 2009.

[2] C. S. Tsai, R. W. Mao, S. K. Lin, N. Wang, and S. C. Tsai, "Miniaturized multiple Fourier-horn ultrasonic droplet generators for biomedical applications," *Lab. Chip*, vol. 10, DOI: 10.1039/c005262k, pp. 2733-2740, 2010.

[3] J. S. Patton and P. R. Byron, "Inhaling medicines: delivering drugs to the body through the lungs," *Nat. Rev. Drug Discovery*, vol. 6, pp. 67-74, Jan 2007.

[4] K. E. Broderick, P. Potluri, S. Zhuang, I. E. Scheffler, V. S. Sharma, R. B. Pilz, and G. R. Boss, "Cyanide detoxification by the cobalamin precursor cobinamide," *Exp Biol Med (Maywood)*, vol. 231, pp. 641-649, May 2006.

[5] C. S. Tsai, R. W. Mao, Y. Zhu, E. Chien, S. C. Tsai, M. Brenner, S. Mahon, D. Mukai, J. Lee, D. Yoon, T. Berney, G. R. Boss, and S. Patterson, "Hand-Held High-Throughput Ultrasonic Monodisperse Aerosol Inhalers for Detoxification of Massive Cyanide Poisoning," in *IEEE International Ultrasonics Symposium*, Dresden, Germany, Paper P4B-9, October 7-10, 2012.

[6] S. C. Tsai, Y. L. Song, T. K. Tseng, Y. F. Chou, W. J. Chen, and C. S. Tsai, "High-frequency silicon-based ultrasonic nozzles using multiple Fourier horns," *IEEE Trans. Ultrason. Ferroelect. Freq. Control*, vol. 51, pp. 277-285, Mar 2004.

[7] N. Maehara, S. Ueha, and E. Mori, "Influence of the vibrating system of a multipinhole-plate ultrasonic nebulizer on its performance," *Rev. Sci. Instrum.*, vol. 57, pp. 2870-2876, 1986.

[8] S. C. Tsai, P. Luu, P. Childs, A. Teshome, and C. S. Tsai, "The role of capillary waves in two-fluid atomization," *Phys. Fluids*, vol. 9, pp. 2909-2918, Oct 1997.

[9] A. J. Yule and Y. Al-Suleimani, "On droplet formation from capillary waves on a vibrating surface," *Proc. of Royal Society of London A*, vol. 456, pp. 1069-1085, May 8 2000.

[10] O. S. Usmani, M. F. Biddiscombe, and P. J. Barnes, "Regional lung deposition and bronchodilator response as a function of b2-agonist particle size," *Am. J. Respir. Crit. Care Med.*, vol. 172, pp. 1497-1504, Dec 15 2005.

[11] A. L. Coates, M. Green, K. Leung, J. Chan, N. Ribeiro, E. Louca, F. Ratjen, M. Charron, M. Tservistas, and M. Keller, "Rapid pulmonary delivery of inhaled tobramycin for Pseudomonas infection in cystic fibrosis: a pilot project," *Pediatr. Pulmonol.*, vol. 43, pp. 753-759, Aug 2008.

[12] B. L. Rottier, C. J. P. van Erp, T. S. Sluyter, H. G. M. Heijerman, H. W. Frijlink, and A. H. de Boer, "Changes in Performance of the Pari eFlow (R) Rapid and Pari LC Plus (TM) during 6 Months Use by CF Patients," *J Aerosol Med Pulm D*, vol. 22, pp. 263-269, Sep 2009.

[13] K. T. Diaz, S. Skaria, K. Harris, M. Solomita, S. Lau, K. Bauer, G. C. Smaldone, and R. Condos, "Delivery and safety of inhaled interferon-gamma in idiopathic pulmonary fibrosis," *J Aerosol Med Pulm Drug Deliv*, vol. 25, pp. 79-87, Apr 2012.

[14] K. Nikander, M. Turpeinen, and P. Wollmer, "The conventional ultrasonic nebulizer proved inefficient in nebulizing a suspension," *J. Aerosol Med.*, vol. 12, pp. 47-53, Summer 1999.

TABLE I. SUMMARY OF DRUGS NEBULIZED

Medicine	Medicine Conc.	Ultrasonic Drive Freq. MHz	Nebulizer Unit	Droplet Diameter $\mu$ m	Output Rate $\mu$ l/min	Disease
Albuterol (isoproterenol)	25mg/ml	1.0	Bench-scale	4.5	150	Asthma
Humulin, U100	100 units/ml	1.0	Bench-scale	4.5	100	Diabetes
Cobinamide	100 mM	1.5	Pocket-size	3.9	130	Cyanide poisoning
Budesonide suspension*	0.5mg/2.0 ml	2.0	Pocket-size	3.1	200	Asthma

\*Prevention of lung cancer in clinical trial



# MEMS-Based Silicon Ultrasonic Twin-Nozzle Nebulizer for Inhalation Drug Delivery\*

R.W. Mao<sup>1</sup>, S.K. Lin<sup>1</sup>, S.C. Tsai<sup>2</sup>, M. Brenner<sup>3,4</sup>

<sup>1</sup> Dept. of Elec. Eng. and Comp. Science

<sup>2</sup> Dept. of Chem. Eng. and Materials Science

<sup>3</sup> Division of Pulmonary and Critical Care Medicine

<sup>4</sup> Beckman Laser Institute and Medical Clinics

University of California, Irvine, CA 92697, USA

<sup>†</sup>E-mail: cstsai@uci.edu

S. Mahon<sup>4</sup>, G. Boss<sup>5</sup>, G. Smaldone<sup>6</sup>, C.S. Tsai<sup>1,7†</sup>

<sup>5</sup> Dept. of Medicine, Univ. of California, San Diego  
La Jolla, CA 92093, USA

<sup>6</sup> Univ. Medical Center and Dept. of Medicine  
Pulmonary/Critical Care Div.

State Univ. of New York at Stony Brook, NY 11790

<sup>7</sup> Inst. of Photonics and Optoelectronics

National Taiwan University, Taipei, TAIWAN

**Abstract**— A versatile silicon-based ultrasonic nebulizer that utilizes a twin-nozzle of multiple Fourier horns at 1–2 MHz drive frequencies has been realized to perform simultaneous aerosolization of cobinamide and magnesium thiosulfate drug solutions. The drive frequency of the individual nozzle for a desirable aerosol diameter was individually designed. Using the 2.0 MHz 4-Fourier horn twin-nozzle aerosols of the two drug solutions with mass median diameter (MMD) of  $3.0 \pm 0.1 \mu\text{m}$  and geometrical standard deviation (GSD) of  $1.18 \pm 0.02$  and total flow rate up to  $400 \mu\text{L}/\text{min}$  were produced.

**Keywords**— MEMS, Multiple Fourier-horn Nozzle, Twin-Nozzle Ultrasonic Nebulizer, Inhalation Drug Delivery, Medicinal Aerosol Mixing

## I. INTRODUCTION

The innovation and potential applications of megahertz (MHz) MEMS-based multiple-Fourier horn ultrasonic nozzles that utilize temporal instability of Faraday waves for formation and ejection of monodisperse micro droplets were highlighted in a new journal most recently [1]. In fact, the resulting ultrasonic nebulizer module using a single nozzle was used successfully to aerosolize a number of common pulmonary drugs [1, 2]. Controllability of particle (aerosol) size range (2 to  $6 \mu\text{m}$ ) and much narrower size distribution achievable by the new device will improve targeting of treatment within the respiratory tract and improve delivery efficiency. For example, a recent in-vitro experiment with Technetium ( $T_c$ )-tagged saline solution using the new nebulizer module has demonstrated potential of higher delivery efficiency than typical commercial nebulizers [3]. Therefore, it may constitute a desirable device for inhalation delivery of expensive medicines such as gamma interferon [4]. Short treatment time is a critical requirement in situations such as massive cyanide poisoning [5]. Clearly, the treatment time can be shortened by increased aerosol output rate of an array of such nozzles. Furthermore, nozzle arrays with individual nozzles operating at identical or different drive frequency will provide the unique capability for formation and subsequent mixing of medicinal aerosols of the same or different medicines at identical or different aerosol sizes. Note that such strategy is essential in order to avoid instability of mixed drug solutions prior to

aerosolization. Here we report the realization of a pocket-size 2 MHz twin-nozzle nebulizer for simultaneous nebulization of cobinamide and magnesium thiosulfate drug solutions.

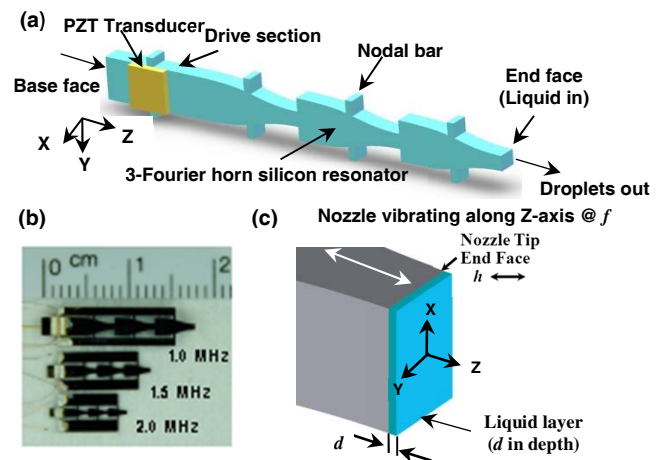


**Fig. 1** (a) 3-D architecture of the MHz multiple-Fourier horn ultrasonic nozzle; (b) Photograph of the 1.0, 1.5, and 2.0 MHz nozzles; (c) Geometry of nozzle end face vibrating at nozzle drive frequency  $f$  with displacement  $h$  and liquid layer  $d$  in depth.

## II. TWIN-NOZZLE ULTRASONIC NEBULIZER

### A. Architecture of Element Nozzle and Working Principle

Each basic (element) nozzle consists of a drive section and a resonator section (Fig. 1a). A lead zirconate titanate (PZT) transducer is bonded on the drive section to excite mechanical vibrations along the nozzle axis. The resonator section is made of multiple (3 in the example) Fourier horns in cascade [1]. The nozzle is designed to vibrate in a single longitudinal mode at the resonance frequency of the multiple Fourier horns. The resonance effect greatly enhances the vibration displacement ( $h$ ) of the nozzle end face (by a factor of approximately 8 for three Fourier horns) and, hence, readily facilitates excitation and subsequent temporal instability of Faraday waves on the liquid layer resting on the nozzle end face. Droplets are formed and ejected from the nozzle end face when its longitudinal vibration displacement exceeds the onset threshold [6]. The

\*Supported by Army/NIH U54-NS063718 and AMRMC W81XWH-12-2-0114, USA.



liquid to be atomized is externally transported to the nozzle end face using a fused silica tube. Importantly, the single vibration mode at the single MHz resonance frequency ensures single-mode capillary wave atomization mechanism, namely, temporal instability of Faraday waves, and production of micron-size monodisperse droplets at very low electrical drive power [1]. The diameter ( $D_p$ ) of the resulting droplets is equal to four tenth of the wavelength ( $\lambda$ ) of the Faraday waves excited as follows [6]:

$$D_p = 2(2/\pi^2)^{1/3}(\sigma/\rho)^{1/3}f^{-2/3} = 0.40\lambda, \quad (1)$$

where  $\sigma$ ,  $\rho$ , and  $f$  designate surface tension, liquid density, and the nozzle drive frequency (resonance frequency), respectively.

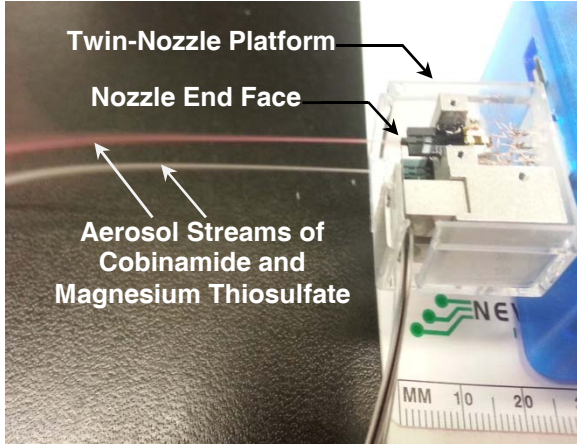


Fig. 2 Twin-nozzle platform

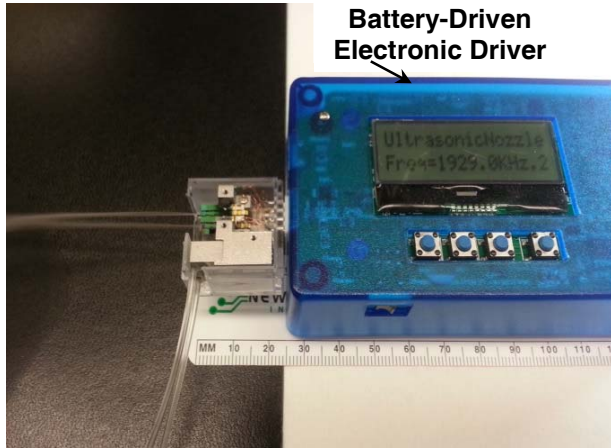


Fig. 3 Pocket-size MEMS-based ultrasonic twin-nozzle nebulizer

### B. Platform of Twin-Nozzle and Pocket-Size Nebulizer

Fig. 2 shows the platform for installation of the twin-nozzle array with identical or separate design specifications for the aerosol size (or drive frequency). The twin nozzles were driven by a pair of independent electronic drivers with controllable frequency and power together with separate fused silica tubes for transport of drug solutions to the nozzle end faces. Fig. 3 shows the resulting battery-run pocket-size ultrasonic nebulizer.

### III. SIMULTANEOUS NEBULIZATION OF IDENTICAL OR DIFFERENT MEDICINES

Separate aerosolization of 100mM cobinamide solution [7] and 1.0 M magnesium thiosulfate solution as well as simultaneous aerosolization of the two drug solutions at varying flow rates were carried out using the nebulizer shown in Figs. 2 and 3 with 2 MHz 4-Fourier horn twin-nozzle and established equipment and characterization procedures [8]. Fig. 2 shows the two streams of aerosols produced simultaneously at respective flow rates of 200 $\mu$ L/min and 250 $\mu$ L/min.

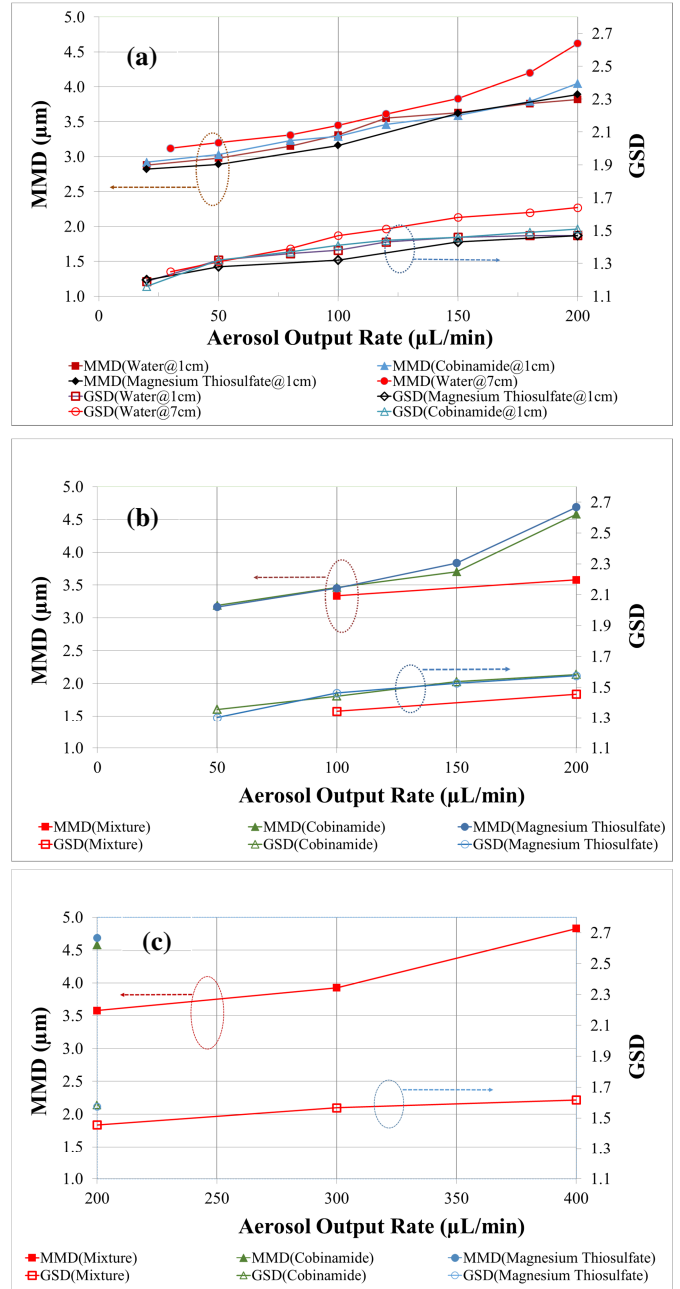


Fig. 4 Measured aerosol sizes in mass median diameter (MMD)/geometrical standard deviation (GSD) versus output rate for 100mM cobinamide solution and 1 M magnesium thiosulfate solution using the 2 MHz 4-Fourier horn ultrasonic nebulizers with (a) single-nozzle, and (b) and (c) twin-nozzle. Note that all data in (b) and (c) were obtained at a distance of 7 cm from the nozzle end face.

The sizes and size distributions of the aerosols produced were measured using Malvern/Spraytec system (Model #STP 5311) which is a well-established non-invasive particle sizing instrument based on laser light diffraction. The streams of aerosol traveled from the nozzle end faces (as depicted in Figs. 2 and 3) and passed the laser beam of the instrument. Fig. 4(a) shows that the sizes of aerosols produced using the 2 MHz single-nozzle nebulizer and measured at 1 cm from the nozzle end face are within the experimental errors in sizes for all three liquids including water (reference liquid), cobinamide solution, and magnesium thiosulfate solution. Specifically, the measured mass median diameters (MMDs) of the aerosols of water and the two aqueous drug solutions are in good agreement with the predicted value of  $3.1\mu\text{m}$  for water based on Eq. (1). The MMDs are seen in Fig. 4(a) to increase from  $2.8\pm0.1$  to  $3.8\pm0.2\mu\text{m}$  as the aerosol output rate (liquid flow rate) increases from 20 to  $200\mu\text{L}/\text{min}$ . The corresponding geometrical standard deviation (GSD) increases from  $1.18\pm0.02$  to  $1.49\pm0.02$ . Fig. 4(a) also shows that the sizes of the water (reference liquid) aerosols measured at a distance of 7 cm are larger than those measured at a distance of 1 cm. The increase in aerosol sizes with increased output rate may be caused by aerosol coalescence in the dense sprays.

A comparison of Fig. 4(b) with Fig. 4(a) shows that like the water aerosols, the aqueous medicinal aerosols measured downstream at 7 cm from the nozzle end faces of the 2 MHz twin-nozzle nebulizer are larger than those measured at 1 cm from where they were produced (liquid layer on the nozzle end face). The two streams of aerosols ensuing from the two nozzle end faces overlapped (mixed) at 7cm downstream. Note that the aerosol MMD and GSD were measured at both 1 and 7 cm from the nozzle end faces.

Furthermore, Figs. 4(b) and 4(c) show that when the two streams of aerosols overlapped at 7 cm from the nozzle end face, the total aerosol output rate was doubled to about  $400\mu\text{L}/\text{min}$ , and the MMD and GSD of the mixed aerosols were slightly larger than those of the individual aerosol streams at half the total output rate.

#### IV. CONCLUDING REMARKS E

A pocket-size ultrasonic nebulizer with 2 MHz twin-nozzle of silicon multiple-Fourier horn has been realized to demonstrate the capability of doubling the aerosol output of same drug solution and simultaneous aerosolization of different drug solutions. Specifically, for 100mM cobinamide and 1 M magnesium thiosulfate drug solutions, simultaneous and continuous aerosolization at respective flow rates of  $200\mu\text{L}/\text{min}$  and  $250\mu\text{L}/\text{min}$  for 7 min. delivered 430mg thiosulfate and 152mg cobinamide that would be nearly sufficient antidote dosages for effective detoxification of cyanide poisoning.

#### REFERENCES

- [1] C.S. Tsai, R.W. Mao, S.K. Lin, & S.C. Tsai, "Faraday instability-based micro droplet ejection for inhalation drug delivery," *TECHNOLOGY*, vol. 2, pp. 75-81, 2014.
- [2] C.S. Tsai, S.K. Lin, R.W. Mao, S.C. Tsai, M.Brenner, S. Mahorn, D. Mukai, and G. Boss, "Pocket-Sized Ultrasonic Nebulizer for Inhalation Drug Delivery," *Proc. of the IEEE Int. Ultrasonics Symp. (IUS-2013)*, pp. 1190-1192, 2013.
- [3] G. C. Smaldone, personal communication.
- [4] K. T. Diaz, S. Skaria, K. Harris, M. Solomita, S. Lau, K. Bauer, G. C. Smaldone and R. Condos, "Delivery and safety of inhaled interferon-gamma in idiopathic pulmonary fibrosis," *J Aerosol Med Pulm Drug Deliv*, vol. 25, pp. 79-87, 2012.
- [5] S.C. Tsai, R.W. Mao, Y. Zhu, E. Chien, J. Maduzia, C.S. Tsai, M.Brenner, S. Mahorn, D. Mukai, G. Boss, and S. Patterson, "Hand-Held High-Throughput Ultrasonic Monodisperse Aerosol Inhalers for Detoxification of Massive Cyanide Poisoning," *Proc. of the IEEE Int. Ultrasonics Sym. (IUS-2012)*, pp. 1632-1634, 2012.
- [6] S.C. Tsai and C.S. Tsai, "Linear Theory on Temporal Instability of Megahertz Faraday Waves for Monodisperse Micro Droplet Ejection," *IEEE Trans. on Ultrasonics/Ferroelectrics and Frequency Control (TUFFC)*, vol. 60, pp. 1746-1755, 2013.
- [7] K. E. Broderick, P. Potluri, S. Zhuang, I. E. Scheffler, V. S. Sharma, R. B. Pilz, and G. R. Boss, "Cyanide detoxification by the cobalamin precursor cobinamide," *Exp Biol Med (Maywood)*, vol. 231, pp. 641-649, May 2006.
- [8] C.S. Tsai, R. W. Mao, S. K. Lin, N. Wang, and S. C. Tsai, "Miniaturized multiple Fourier-horn ultrasonic droplet generators for biomedical applications," *Lab on a Chip*, vol. 10, pp. 2733-2740, DOI: 10.1039/c005262k, 2010.



2015 International Congress on Ultrasonics, 2015 ICU Metz

# Ultrasound-Driven Megahertz Faraday Waves for Generation of Monodisperse Micro Droplets and Applications

Chen S. Tsai<sup>1\*</sup>, Rong W. Mao<sup>1</sup>, Shih K. Lin<sup>1</sup>, Shirley C. Tsai<sup>2</sup>, Gerry Boss<sup>3</sup>, Matt Brenner<sup>4</sup>, Gerry Smaldone<sup>5</sup>, Sari Mahon<sup>4</sup>, Kaveh Shahverdi<sup>1</sup>, and Yun Zhu<sup>1</sup>

<sup>1</sup>Department of Electrical Engineering and Computer Science

<sup>2</sup>Department of Chemical Engineering and Materials Science  
University of California, Irvine, CA 92697, USA

<sup>3</sup>School of Medicine, University of California, San Diego, La Jolla, CA 92093, USA

<sup>4</sup>Division of Pulmonary and Critical Care Medicine, Beckman Laser Inst. and Medical Clinics

School of Medicine, University of California, Irvine, CA 92697, USA

<sup>5</sup>Univ. Medical Center and Dept. of Medicine Pulmonary/Critical Care Div.

State University of New York at Stony Brook, NY 11790, USA

## Abstract

Our theoretical findings on instability of Faraday waves at megahertz (MHz) drive frequency and realization of silicon-based MHz multiple-Fourier horn ultrasonic nozzles (MFHUNs) together have enabled generation of mono-disperse droplets of controllable diameter (2.5–6.0  $\mu\text{m}$ ) at very low electrical drive power (<0.5 Watt). The resulting battery-run clogging-free droplet generator has imminent application to pulmonary (inhalation) drug delivery and other potential applications. Here an update of advances on analysis and design of the MHz MFHUNs and the underlying physical mechanism for generation of mono-disperse micro droplets, and the nebulizer platform for application to detoxification of cyanide poisoning are presented.

© 2015 The Authors. Published by Elsevier B.V.

Peer-review under responsibility of the Scientific Committee of 2015 ICU Metz.

**Keywords:** Faraday instability, multiple-Fourier horns, monodisperse micro droplet, pulmonary drug delivery, cyanide poisoning

## 1. Introduction

A number of ultrasonic techniques for generation of micro droplets, for examples, the micro-machined droplet generators based on a liquid horn structure (Meacham et al., 2004) and piezo-electrically actuated flex-tensional micro-machined transducers (Perçin et al., 2002; Kwon et al, 2006) were reported. Current commercial ultrasonic nebulizers produce droplets of uncontrollable and very broad size distributions (polydisperse). Here we present a new technique for generation of controllable monodisperse droplets of desirable diameter range (2.5 to 6.0  $\mu\text{m}$ ) using Faraday waves excited by ultrasound with MHz multiple-Fourier horns (MFHs) in cascade and in resonance.

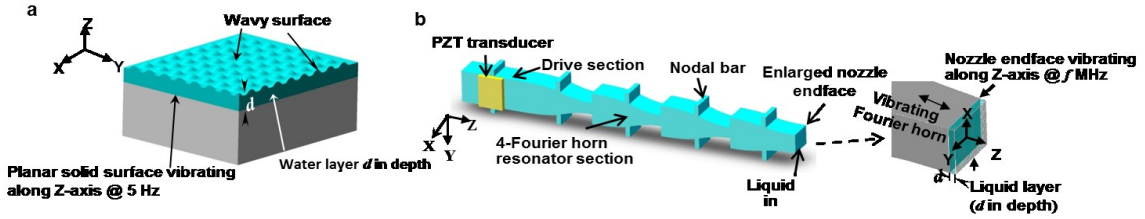


Fig. 1. (a) Classical planar geometry for Faraday wave formation at low drive frequency; (b) 3-D architecture of MHz 4-Fourier horn ultrasonic nozzle with the geometry of its endface and the liquid layer

Faraday waves were first observed as wavy surface of a water layer resting on an elastic planar solid support subjected to perpendicular vibration, as depicted in Fig. 1a, at a very low drive frequency of 5 Hz (Faraday, 1831), and analyzed (Rayleigh, 1883). Faraday instability, the underlying physical mechanism for Faraday wave formation and amplification, was studied extensively based on Faraday's planar geometry, but mostly at very low drive frequencies ranging from tens to thousands hertz (Hz). See the references cited in (Cerdeja and Tirapegui, 1997; Tsai and Tsai, 2013). At such low drive frequencies, various standing-wave patterns were observed when the vibration amplitude (displacement) on the solid surface reached the onset threshold for Faraday wave formation. However, in the few reports on experiments at such low drive frequencies droplet ejection was found to take place only when the vibration amplitude on the solid surface was much higher than the onset threshold for Faraday wave formation (Yule, 2000). In stark contrast, our recent discovery as presented here shows that at the much higher drive frequencies of MHz the onset threshold for Faraday wave formation is much lower and the vibration amplitude required for subsequent droplet ejection is only slightly higher than the onset threshold for Faraday wave formation.

## 2. Theory and technique

### 2.1. Excitation of Enhanced Ultrasonic Vibration at MHz using Multiple-Fourier Horns in Resonance

Silicon-based multiple Fourier horns (MFHs) in cascade and vibrating at a single resonance frequency at MHz (Fig. 1b) is used to facilitate Faraday's classical low-frequency experiment at MHz drive frequency. The resulting multiple-Fourier horn ultrasonic nozzle (MFHUN) with its Z-axis along the  $\langle 110 \rangle$  direction of the silicon wafer is fabricated using the MEMS technology (Tsai et al., 2009). The nozzle consists of a drive section and a resonator section. A lead zirconate titanate (PZT) piezoelectric transducer is bonded on the drive section to excite mechanical vibrations along the nozzle axis (Z-axis). The resonator section is made of MFHs in cascade. Each horn is of half wavelength design. The nozzle is designed to vibrate at a single resonance frequency of the MFHs. The resultant vibration amplitude (displacement) on the nozzle end face (tip of the distal horn) is greatly enhanced with a gain of  $M^n$  for a n-Fourier horn nozzle in which  $M$  is the magnification of displacement for each horn (Tsai et al., 2009).

A 3-D finite element method simulation is carried out first for vibration mode shape analysis and then for electrical impedance analysis. The former determines the nozzle resonance frequency of pure longitudinal vibration mode; the latter determines the longitudinal vibration amplitude on the nozzle end face and the electrical impedance at the resonance frequency (Tsai et al., 2009). The simulated vibration amplitude (at electrode voltage of 1.0 V) is then used to determine the threshold voltage required to produce the onset threshold of vibration amplitude ( $h_{cr}$ ) for Faraday wave formation and droplet ejection. Finally, the threshold voltage thus obtained together with the resistive part of the impedance determined is then used to calculate the electrical drive power required for droplet ejection.

### 2.2. Linear Theory on Temporal Instability of MHz Faraday Waves for Droplet Ejection

The enhanced longitudinal vibration amplitude on the end face of the MFHUN exerts a periodic pressure on the resting liquid layer depicted in Fig. 1(b). Faraday waves, under an external periodic acceleration  $h(2\pi f)^2 \cos(2\pi f t)$ , are formed on the free surface of the liquid layer when the peak vibration amplitude of the nozzle end face ( $h$ ) reaches the onset threshold ( $h_{cr}$ ). The theoretical treatment based on linearized Navier-Stokes equations for incompressible Newtonian liquids with density  $\rho$ , surface tension  $\sigma$ , and kinematic viscosity  $\nu$  (Tsai and Tsai, 2013) results in temporal evolution of the Faraday wave amplitude  $\xi_k$  of the  $k^{\text{th}}$  mode:

$$\xi_k(t) = \xi_0 e^{\pi k f (h - h_{cr}) t} \sin(2\pi(f/2)t - \pi/4), \quad (1)$$

where the wave number  $k = 2\pi/\lambda$ , the wave frequency  $\omega_k^2 \equiv \sigma k^3 / \rho$ ,  $\xi_0$  is the initial wave amplitude, and  $h_{cr}$  is:

$$h_{cr} = 2\nu k / (\pi f) = 2\nu \rho^{1/3} (\pi \sigma)^{-1/3} f^{-1/3}. \quad (2)$$

Eq. (2) shows the specific dependence of the onset threshold on the drive frequency ( $f$ ) and the liquid properties ( $\rho$ ,  $\sigma$ , and  $\nu$ ). It is important to emphasize that  $h_{cr}$  decreases with the drive frequency in accordance with  $f^{-1/3}$ , and the wave amplitude  $\xi_k(t)$  grows exponentially in time when  $h > h_{cr}$ . While  $h_{cr}$  decreases with the drive frequency in accordance with  $f^{-1/3}$ , the exponent  $\pi k f (h - h_{cr}) t$  in the exponential factor of  $\xi_k(t)$  increases with the drive frequency in accordance with  $f^{4/3}$ . Thus, the temporal growth of the single-mode MHz Faraday wave amplitude excited is very rapid once the nozzle end face excitation displacement  $h$  exceeds the onset threshold  $h_{cr}$ .

### 2.3. Dynamics of Droplet Ejection and Droplet Diameter

Take the 2.0 MHz drive frequency with the corresponding wavelength ( $\lambda$ ) of 7.6 $\mu$ m in water and the high periodic acceleration  $h(2\pi f)^2 \cos(2\pi f t)$  of 4.19 $\times 10^6 g$  as an example, where  $g$  is the gravitational acceleration. When  $h$  exceeds the predicted  $h_{cr}$  of 0.26 $\mu$ m by as small as 0.01 $\mu$ m the growth rate factor  $e^{\pi k f (h - h_{cr}) t}$  of Eq. (1) in a time increment of 0.4ms is  $\sim 2 \times 10^{11}$  times that with  $(h - h_{cr})$  as large as 100 $\mu$ m at 200 Hz drive frequency and a low periodic acceleration of 16g (Yule and Al-Suleimani, 2000) at the same time increment (0.4ms). The amplitude growth rate factor at 2.0 MHz with  $(h - h_{cr})$  of 0.01 $\mu$ m in a time increment of 0.4ms is still greater (by 8%) than that at 200 Hz with  $(h - h_{cr})$  of 100 $\mu$ m in a much longer time increment of 185ms. Thus, the wave amplitude at 2 MHz drive frequency grows very rapidly and when it becomes too great to maintain stability the Faraday waves break up to result in ejection of droplets from the free surface of the liquid layer. Fig. 2 shows a stream of droplets issuing from the endface of a 4-Fourier horn 2 MHz nozzle at atomization frequency of 1.921 MHz, output rate of 200 $\mu$ L/min, and electrical drive power of 0.2 W. Note that the liquid (water) was transported to the nozzle endface through a silica tube and a 50 $\mu$ m liquid layer was maintained during atomization.

The theoretical droplet diameter ( $D_p$ ) in terms of Faraday wavelength ( $\lambda$ ) is as follows (Tsai and Tsai, 2013):

$$D_p = 2(2/\pi^2)^{1/3} (\sigma/\rho)^{1/3} f^{-2/3} = 0.40\lambda \quad (3)$$

Clearly, for a given liquid to be atomized, the desired size of the droplets can be controlled by the drive frequency ( $f$ ) of the MFHUN in accordance with  $f^{-2/3}$ ; the higher the nozzle drive frequency the smaller the droplet size. The size and size distribution of the droplets (aerosols) produced by the 2.0 MHz nozzle (Fig. 2) was measured using Malvern/Spraytec size analyzer (Model #STP 5311). The measured droplet diameter is 3.4 $\pm$ 0.3 $\mu$ m in good agreement with the predicted value of 3.2  $\mu$ m which can be significantly smaller for low surface tension medicines.

In summary, all the experimental data including controllable micron-size droplet diameter, narrow size distribution, and very low electrical drive power are in excellent agreement with the predictions of the linear theory.

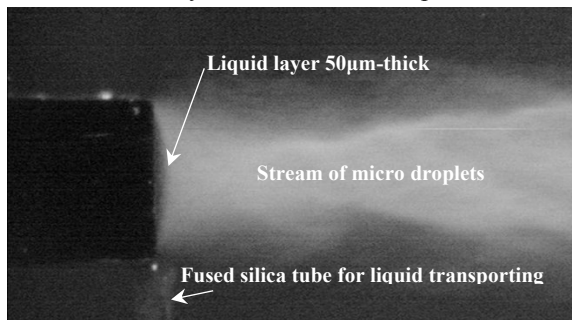


Fig. 2. Droplet ejection from a water layer on the end face of a 4-Fourier horn 2.0 MHz nozzle at 200 $\mu$ L/min output rate and <0.2 W electrical power.

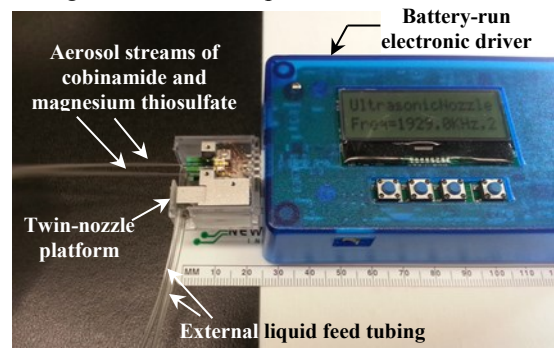


Fig. 3. Battery-run pocket-size 2 MHz twin-nozzle ultrasonic nebulizer.



### 3. Applications to inhalation drug delivery

The droplet generator presented has demonstrated imminent application to inhalation drug delivery and other applications such as nanoparticle synthesis, processing for electronic and photonic nano-structures can be envisaged. Inhalation is an important route for non-invasive drug delivery. Drugs designed to treat pulmonary diseases or for systemic absorption through the lung require optimum particle size (2 to 6 $\mu$ m) to target delivery (Patton and Byron, 2000). Therefore, control of aerosol size plays a critical role in the efficient and effective delivery of medications. Even the advanced commercial devices using vibrating mesh technology still suffer from broad aerosol size (polydisperse) distributions and lack of size-control capability, and are also plagued by clogging of the orifices of the mesh used. The battery-run pocket-size nebulizer realized earlier using a single MFHUN was used successfully to aerosolize a variety of common pulmonary drugs (Tsai et al., 2014). Controllability of particle (aerosol) size range (2.5 to 6 $\mu$ m) and much narrower size distribution demonstrated by the new nebulizer will improve targeting of treatment within the respiratory tract and improve delivery efficiency. For example, a recent in-vitro experiment with Technetium ( $T_c$ )-tagged saline solution has demonstrated higher delivery efficiency than the existing commercial nebulizers (Diaz et al., 2012).

Short treatment time is a critical requirement in acute situations such as massive cyanide poisoning (Tsai et al., 2012). Clearly, the treatment time can be shortened by increased aerosol output rate of an array of MFHUNs. Furthermore, nozzle arrays with individual nozzles operating at identical or different drive frequency will provide the unique capability for simultaneous formation of aerosols of the same or different medicines at identical or different aerosol sizes. Such strategy is essential in order to avoid instability of mixed drug solutions prior to aerosolization. A battery-run pocket-size nebulizer with twin-nozzles as shown in Fig. 3 was constructed most recently to demonstrate simultaneous nebulization of cobinamide and magnesium thiosulfate antidotes for detoxification of cyanide poisoning. Specifically, for 115mM cobinamide and 1 M magnesium thiosulfate antidote solutions, simultaneous and continuous aerosolization each at a flow rate of 250 $\mu$ L/min for 5 min delivered 430mg thiosulfate and 155mg cobinamide that would be sufficient antidote dosages for effective detoxification of cyanide poisoning.

**Acknowledgements.** Supports by the National Institute of Health (NIH), USA (NIBIB Grant #5R21EB006366, Counter ACT Program U54-NS063718 and AMRMC W81XWH-12-2-0114) are gratefully acknowledged.

### References

- Cerda, E.A., E. L. Tirapegui, 1997. Faraday's instability for viscous liquids. *Phys. Rev. Lett.*, **78**, 859-862.
- Diaz, K.T., S. Skaria, K. Harris, M. Solomita, S. Lau, K. Bauer, G.M. Smaldone, R. Condos, 2012. Delivery and safety of inhaled interferon- $\gamma$  in idiopathic pulmonary fibrosis. *J. Aerosol Medicine and Pulmonary Drug Delivery*, **25**, 79-87.
- Faraday, M., 1831. On a peculiar class of acoustical figures and on certain forms assumed by groups of particles upon vibrating elastic surfaces. *Phil. Trans. Roy. Society, London*, **A52**, 299-340.
- Kwon, J.W., H. Yu, Q. Zou, E.S. Kim, 2006. *J. Micromech. Microeng.*, **16**, 2697-2704.
- Meacham, J.M., C. Ejimofor, S. Kumar, F.L. Degertekin, A.G. Fedorov, 2004. *Rev. Scientific Instruments*, **75**, 1347-1352.
- Patton, J.S., P. R. Byron, 2007. Inhaling medicines: delivering drugs to the body through the lungs. *Nat. Rev. Drug Discovery*, **6**, 67-74.
- Perçin, G., B.T. Khuri-Yakub, 2002. *IEEE Trans. on Ultrasonics/Ferroelectrics and Frequency Control*, **49**, 573-584 and 585-595.
- Rayleigh, B., 1883. On the crispation of fluid resting upon a vibrating support. *Phil. Mag.*, **16**, 50-58.
- Tsai, S.C., C. H. Cheng, N. Wang, Y. L. Song, C. T. Lee, C. S. Tsai, 2009. Silicon-based Megahertz ultrasonic nozzles for production of monodisperse micrometer-sized droplets. *IEEE Trans. Ultrason. Ferroelect. Freq. Control (UFFC)*, **56**, 1968-1979.
- Tsai, C.S., R.W. Mao, S.K. Lin, N. Wang, S.C. Tsai, 2010. *Lab on a Chip*, **10** 2733-2740.
- Tsai, S.C., S.K. Lin, R.W. Mao, C.S. Tsai, 2012. *Phys. Rev. Lett.*, **108**, 154501-154501 to -154505.
- Tsai, S.C., R.W. Mao, Y. Zhu, E. Chien, J. Maduzia, C.S. Tsai, M. Brenner, S. Mahorn, D. Muka, G. Boss, and S. Patterson, 2012. *Proc. of the IEEE Int. Ultrasonics Sym. (IUS-2012)*, 1632-1634.
- Tsai, S.C., C.S. Tsai, 2013. Linear theory of temporal instability of megahertz Faraday waves for monodisperse microdroplet ejection. *IEEE Trans. UFFC*, **60**, 1746-1754.
- Tsai, C.S., R.W. Mao, S.K. Lin, Y. Zhu, S.C. Tsai, 2014. Faraday instability-based micro droplet ejection for inhalation drug delivery. *TECHNOLOGY*, **2**, 75-81. <http://www.worldscientific.com/worldscinet/technology>.
- Yule, A.J., Y. Al-Suleimani, 2000. *Proc. of Royal Society of London A*, **456**, 1069-1085.